Copyright

by

Joel Kevin Blakeney

2015

The Dissertation Committee for Joel Kevin Blakeney Certifies that this is the approved version of the following dissertation:

Characterization of Electron Propagation via Coherent Transition Radiation in Two Different Conductivity Regimes

Committee:

Todd Ditmire, Supervisor

Roger Bengtson

Greg Sitz

Michael Becker

Gennady Shvets

Characterization of Electron Propagation via Coherent Transition Radiation in Two Different Conductivity Regimes

by

Joel Kevin Blakeney, B.S.; M. S. E.

Dissertation

Presented to the Faculty of the Graduate School of

The University of Texas at Austin

in Partial Fulfillment

of the Requirements

for the Degree of

Doctor of Philosophy

The University of Texas at Austin

May 2015

Dedication

To my family

Acknowledgements

.

This thesis would not have been possible without a number of people. I would like to first thank all the staff at the Center for High Energy Density Science for their support, expertise, and understanding.

My fellow lab mates – In Tai Kim, Matt McCormick, Brendan Murphy, Sandra Bruce, and Ahmed Helal – have provided immeasurable help. Whether providing support or comic relief, their helpfulness and understanding made the lab work manageable. The staff scientists, Hernan Quevedo, Gilliss Dyer, and Aaron Bernstein, have been great advisors. I appreciate their willingness to always make time and engage any issue I had. I'd like to thank Roger Bengtson for re-introducing me to Physics. I would probably be an attorney if he hadn't directed me to Dr. Ditmire's door. Erhard Gaul is probably the best laser mentor ever. Being around him in the lab, served as a catalyst for me to pursue a PhD. To my supervisor, Todd Ditmire, I am eternally gratefully for the chance to pursue a PhD in High Energy Density Physics.

To my committee members, thanks for your time and feedback to my dissertation. Lastly, I want to send thanks to my family. Without them I wouldn't have made it. My parents, Ernest & LaWanda, served as my inspiration and role models. My wife, Tami, who has been both my greatest champion and my rock. Coming to my wife and son made the daily grind of the lab enjoyable.

Characterization of Electron Propagation via Coherent Transition Radiation in Two Different Conductivity Regimes

Joel Kevin Blakeney, Ph.D.

The University of Texas at Austin, 2015

Supervisor: Todd Ditmire

High intensity lasers interacting with an overdense target can accelerate high energy ("hot") electrons at currents that would far exceed the Alfven limit. Hot electron propagation can be inhibited when bulk electron motion is unable to provide a return current such that the total current is nearly zero. The ability of the material to generate a sufficient return current, and permit propagation of the non-collisional hot electrons, is strongly affected by the material conductivity. Here we present an experimental study of the interplay between the conductivity of strongly heated solid density matter and the propagation of laser accelerated hot electrons.

We diagnose the hot electrons by imaging the coherent transition radiation(CTR) generated from the target's back surface into vacuum. The 1ω and 2ω harmonics of the CTR were imaged using a 10x microscope objective to CCD cameras. The spatial profile and energy emitted at the rear surface were evaluated, showing marked differences between high and low conductive materials.

The conductivity is changed through both target temperature and material selection. CTR images of electrons propagating in high conductive targets, aluminum, displayed a high degree of collimation and a spot size 2.5x smaller than the focal spot. In contrast, CTR images from low conductive target exhibited significant expansion of the

electron beam. Electron propagation through the dielectric experienced 2x divergence on average compared to the aluminum. The 1ω and 2ω CTR images of heated aluminum were both 1.2 times greater area on average than the corresponding unheated spot sizes. Evaluating the energy contained in a 7.5 x 7.5 micron square, the unheated targets have 1.6x more energy for 1ω and 2x greater for 2ω on average. The reduction in material conductivity produces an electrostatic field opposing the hot electron beam leading to a reduction in energy and increased divergence of the electron beam.

Table of Contents

List of Figures

Chapter 1: Introduction

Lasers are present in virtually every aspect of our lives and have a wide range of applications ranging from the ordinary, scanning bar codes, to the extraordinary, medical surgery, fusion energy, etc. High intensity lasers have proliferated over the last 30 years due to the process of chirped pulse amplification (CPA) [1]. In CPA, a pulse is dispersed in time, amplified, and then compressed back to the original pulse duration yielding a high peak power. This reduces the potential for component laser damage and nonlinear effects associated with high energy laser pulses. CPA has allowed six orders of magnitude increase in peak power with the potential for more as shown in figure 1 [2].

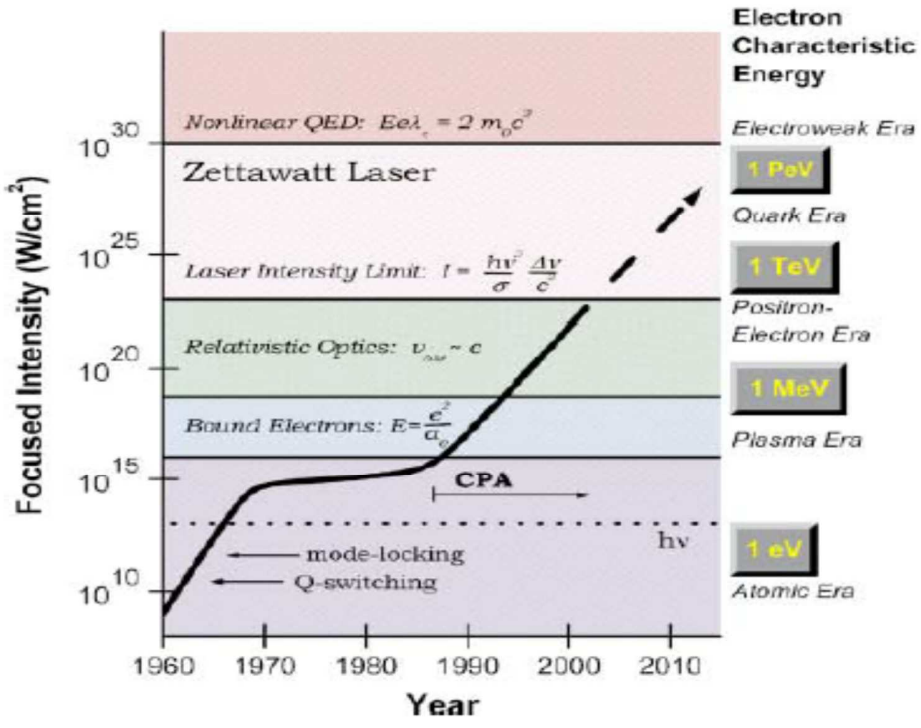

Figure 1: Focused laser intensity timeline. Dotted line indicates proposed intensity increase. Reproduced from [2].

As the above figure displays, the high peak powers combined with a tightly focused beam generates high intensities which produce large number of energetic ("hot") electrons transported as a current.

There are a wide range of applications for hot electron currents including X-ray generation [3], pulsed radiography [4], warm dense matter studies [5,6], intense ion beams [7] and laser fusion [8]. The most promising and widely studied topic is laser fusion, so this paper will consider electron current propagation in the context of laser fusion.

Fusion energy is being pursued in two main thrusts – magnetic confinement fusion (MCF) and inertial confinement fusion (ICF). MCF uses a magnetic field to contain a low density, ~10^{20} m^{-3} deuterium-tritium plasma in a 10 meter toroidal vacuum vessel. The thermonuclear reaction occurs slowly ~1 second. In ICF, a 100µm deuterium-tritium target is compressed to densities of 10^{32} m^{-3} by approximately 1MJ of laser energy [9]. The ICF timescale is 1ns or less and the ions are confined by their own inertia.

The most widely known ICF experiment occurs at the NIF laser facility at Lawrence Livermore National Lab shown in figure 2.

Figure 2: Pictures of NIF laser facility. Overall footprint is equal to 3 football fields (Image courtesy of Lawrence Livermore National Laboratory).

In ICF on NIF, a target capsule is adiabatically imploded by an external radiation source. The kinetic energy of the imploded shell is eventually converted to thermal energy creating ignition conditions at a central hot spot. Several inherent issues have been encountered: the hot spot requires minimal disturbance from laser-target generated particles, a low adiabat must be maintained for optimal compression, and the implosion is inherently unstable hydrodynamically as two fluids of different mass, target and capsule, are being accelerated simultaneously.

Another approach to fusion energy that decouples the target compression from the ignition offers a solution with the NIF approach to ICF. In the Fast Ignition scheme, a target experiences reduced compression with a large current of relativistic electrons externally generated striking the fuel creating ignition potentially resulting in greater gain [10]. In this scenario, the electrons must propagate a distance of a couple hundred microns through a dense plasma without significant energy loss or divergence. An overview of both ICF applications is shown in figure 3.

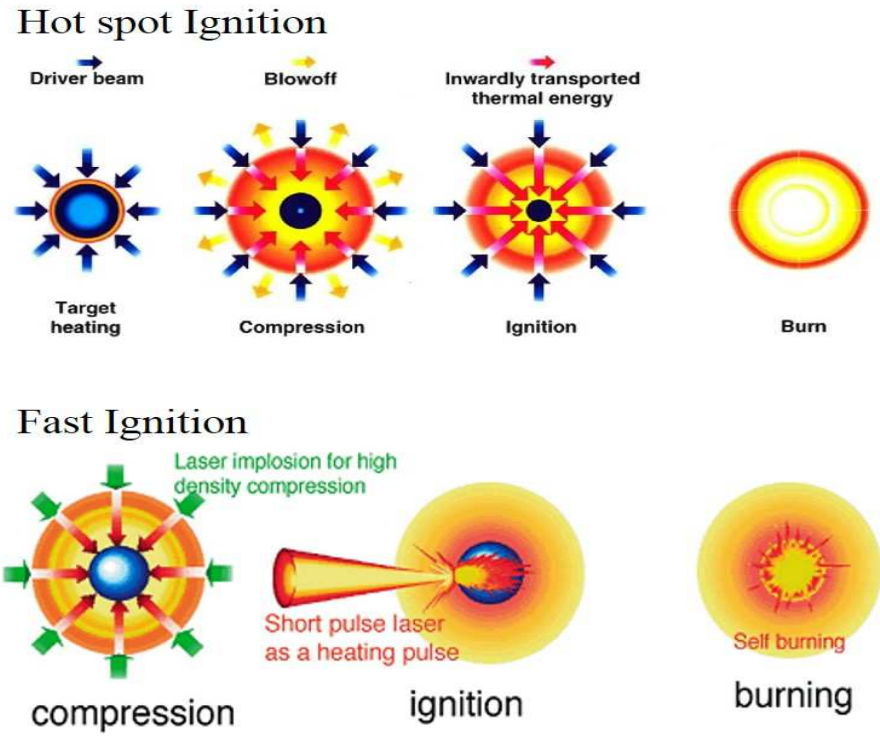

Figure 3: Schematic overview of laser ICF ignition schemes. Hot spot ignition at top and the bottom shows fast ignition. (Image courtesy of Lawrence Livermore National Laboratory)

It has been observed [11-13] that the electron propagation is affected by a number of different issues – beam divergence [14-16], plasma instabilities [17, 18] and electric inhibition [19-21]. The main purpose of this research is to explore the role of electric inhibition in electron propagation. Intense electron currents cannot propagate undisturbed without a compensating return current. The return current is dependent on the material conductivity. The focus of this thesis is measurement of the quantitative difference in electron propagation in two different conductivity regimes. We influence the material conductivity through two methods, changing the target temperature and material selection.

The primary diagnostic measuring electron propagation is optical radiation emitted from electrons escaping, or transitioning, from the rear surface of the target into vacuum. When the emitted transition radiation is coherent (CTR), distinct spectral components at harmonics of the laser frequency are observed. The CTR gives information both about the electron spatial distribution and the temperature through the emitted harmonic. The main drawback is the emitted radiation intensity depends nonlinearly on the coherence of the electron bunch and gives information only about the electrons that can escape the target sheath field.

This thesis is organized as follows. The next chapter describes the basic interaction of high-intensity lasers with solid density targets and single electron motion in an external field. Chapter 3 introduces the laser interaction with an overdense target. Different effects manifest as a function of laser intensity. The thermal transport of the laser pulse throughout the target is discussed. Chapter 4 explains the propagation of electrons through a solid density medium. Material conductivity as a function of temperature, return currents, and plasma instabilities are all discussed. Chapter 5 explains the theory of transition radiation. The theory is extended from single particle radiation to large numbers of electrons generated in a laser-target interaction. Chapter 6 describes the experimental layout including the GHOST laser. The target chamber geometry is described along with the experimental techniques related to the positioning of a solid target in the laser focal plane. Chapter 7 details the 1ω, 2ω CTR observed for multiple experiments. The hydrodynamic code used to model the heating beam is explained. A conductor, aluminum, was compared with an insulator, Al/Plastic sandwich. The Al foil conductivity was reduced by introducing a heating beam with different time delays prior to the arrival of the main beam. The emitted CTR energy and area of the heated Al foils were compared to unheated Al foils. For comparison, the

sandwich Al/Plastic target was also heated and the observed CTR compared to unheated Al/Plastic. Chapter 8 concludes the thesis, summarizes the results and discusses future directions.

Chapter 2: Introduction to High-Intensity Laser Solid Interactions

High Energy Density Physics refers to states of matter with an energy density of at least 10^{11} J/m^3 corresponding to a pressure of 1Mbar. This regime can be accessed with many different devices: lasers, pulsed power devices, linear accelerators and gas guns. The baseline parameters for High Energy Density Physics are 500T magnetic field, 10^{11} V/m electric fields and light pressure I/c of ~0.3 Gbar [22]. The introduction of chirped pulse amplification has allowed lasers to easily achieve these values in a traditional laboratory. The current starting point for high energy density physics occurs at a laser intensity of 3.5 * 10^{16} W/cm^2. This occurs when the peak electric field of the laser wave $E_o = \sqrt{\frac{8\pi I}{c}}$ is equivalent to atomic unit of the electric field, $E_a = \frac{e}{a_{Bohr}^2} = 5.1*10^9 V/cm$ where $a_{Bohr} = \frac{4\pi\varepsilon_o\hbar^2}{m_e e^2}$ is the Bohr radius. In the GHOST lab, peak intensities above 1* 10^{19} W/cm^2 are typical.

In this chapter, basic plasma concepts will be review including general laser target interaction. Single particle motion in the presence of an intense field will be derived.

2.1 Plasma Concept Overview

Plasmas respond to charge perturbations with an oscillation frequency given by

$$\omega_p = \sqrt{\frac{n_e e^2}{\varepsilon_o m_e}} \quad (1)$$

where e is the electron charge, n_e is the electron density, and m_e is the electron mass. This frequency is called the plasma frequency and is proportional to the electron density. Each species in the plasma has its own frequency, but typically the most important and the one we are concerned with is the electron frequency. A metal target at solid density,

$1*10^{23} cm^{-3}$ has a plasma frequency $\omega_p = 2*10^{16} s^{-1}$. The spatial scale of a plasma is typically defined by the Debye length [23],

$$\lambda_D = \sqrt{\frac{kT_e + kT_i}{4\pi e^2 n_o Z}} \tag{2}$$

where kT_e is the electron temperature, kT_i is the ion temperature, Z is the average charge state, and n_o initial electron density. The Debye length is the length over which a plasma observes charge neutrality. The Debye length is derived based on the assumption that the plasma is weakly coupled, eφ<<kT, where the potential energy is much less than the kinetic energy of the plasma. This assumption is not always valid in the high energy density regime.

2.2 LASER-TARGET INTERACTION INTRODUCTION

Laser technology has allowed shorter and shorter pulse durations, 40fs to 1ps are typical, with increasing laser contrast. Theoretically, a high-contrast, short pulse laser can interact with a completely undisturbed target at density n_o. In reality, the laser may consists of prepulses of 10^{-5} to 10^{-8} compared to the main pulse intensity and preceding the main pulse up to 1ns. A laser pulse with peak intensity 10^{19} W/cm^2 and a pre-pulse 10^{-6} prior the main pulse by 100ps can generate a micron length preplasma at the target front surface. As the laser interacts with the target, the laser energy is transferred to the electrons which oscillate in the laser electric field. Ionization can occur via multiple processes while some electrons can be directly accelerated by the laser field which is covered in chapter 3. The transfer of laser momentum to the target causes the ablated plasma layer to be ejected away from the target with velocity [24]

$$C_s = \sqrt{\frac{k\left(ZT_e + T_i\right)}{M_i}} \tag{3}$$

where T_e, T_i are the electron and ion temperatures, k is the Boltzmann constant, and M_i is the ion mass. The density scale length is

$$L_n = n\frac{dx}{dn} \approx C_s \tau_L \tag{4}$$

where n is the plasma density, $\frac{dn}{dx}$ is the slope at the density n, and τ_L is the laser pulse duration. For a surface temperature of 1keV and pulse duration of 120fs, the plasma has expanded a distance of 10nm in an Al target.

As the laser EM wave transitions from vacuum to target preplasma, we obtain the dispersion relation for an electromagnetic wave traveling through a plasma

$$\omega^2 = \omega_{pe}^2 + k^2 c^2 \tag{5}$$

If a wave has a frequency $\omega < \omega_{pe}$, then k<0 and wave propagation ceases. This cutoff, expressed in terms of electron density, is called the critical density [25]

$$n_{cr} = \gamma \frac{1.1\times10^{21}}{\lambda_u[\mu m]} cm^{-3} \tag{6}$$

The laser actually can propagate further via an exponentially decaying wave. This is called the collisionless skin depth $l = \frac{c}{\omega_{pe}}$. Since the critical density is proportional to the laser intensity $n_{cr} \sim \gamma$, the laser can penetrate further into a target at higher intensities. This is due to the fact that the mass of electrons increase as they become relativistic. This has been experimentally observed [26] and with the correct combination of target/laser parameters the whole target may become transparent to the laser pulse [27].

2.3 SINGLE ELECTRON MOTION

Lasers transfer the majority of their energy into electrons through the interaction of the oscillating laser electromagnetic fields at the critical density surface. The motion

of an electron in an E-M plane wave has previously been solved [28] and is the starting point for describing electron motion in a laser field. For a non-relativistic electron in a vacuum under the influence of a linear polarized plane wave, conservation of momentum yields the equation of motion

$$v = v_{osc} \sin\left(w_L t\right) + v_o \tag{7}$$

where v_o is the particle velocity just after ionization, ω_L is the laser frequency, and $v_{osc} = \frac{eE_o}{m_e \omega_L}$ called the electron quiver velocity. The cycle averaged kinetic energy of this oscillating electron is

$$U_p = \left\langle \frac{1}{2} m v_{osc}^2 \right\rangle = \frac{e^2 E_o^2}{4 m_e \omega_L^2} \tag{8}$$

called the ponderomotive potential. In a plane wave interaction with an electron, no net energy is transferred to the electron. The electron will oscillate during the pulse interaction time and then return to initial velocity [29].

For relativistic motion, the electron oscillation velocity approaches c. The oscillation velocity is related to the laser intensity through the normalized laser amplitude,

$$a_o = \frac{eE_o}{m_e \omega_L c} = \frac{v_{osc}}{c} = 8.55 \times 10^{-10} \sqrt{I\left(W / cm^2\right)} \tag{9}$$

A value of 1 corresponds to a laser intensity $I = 1.4 \times 10^{18} \left(W / cm^2\right)$. The electron motion is described by [30] the Lorentz Force equation

$$\frac{dp}{dt} = e\left(E + \frac{1}{c} v \times B\right) \tag{10}$$

along with an energy equation

$$\frac{d}{dt}\left(\gamma m c^2\right) = -e\left(v \bullet E\right) \tag{11}$$

where $p = \gamma m v$ and $\gamma = \left(1 + \frac{p^2}{m^2 c^2}\right)$. If we consider a plane wave polarized along the x-axis, the transverse momentum can be written $p_x = a_o mc \sin\left(\omega t\right)$. If the electron is at rest

before the EM wave arrives, the longitudinal and transverse momentum of the electron can be related through $p_z = \frac{p_x^2}{2mc}$. An expression for the longitudinal momentum is then obtained $p_z = \frac{a_o^2 mc}{4}\left(1-\cos\left(2\omega t\right)\right)$. From the momenta, the electron orbits can be derived and are plotted for several values of a_o (figure 4). The electron now has a longitudinal component that grows with time or distance called the drift velocity and can be calculated as $\frac{1}{c}\frac{dz}{dt} = \frac{a_o^2}{4+a_o^2}$. .

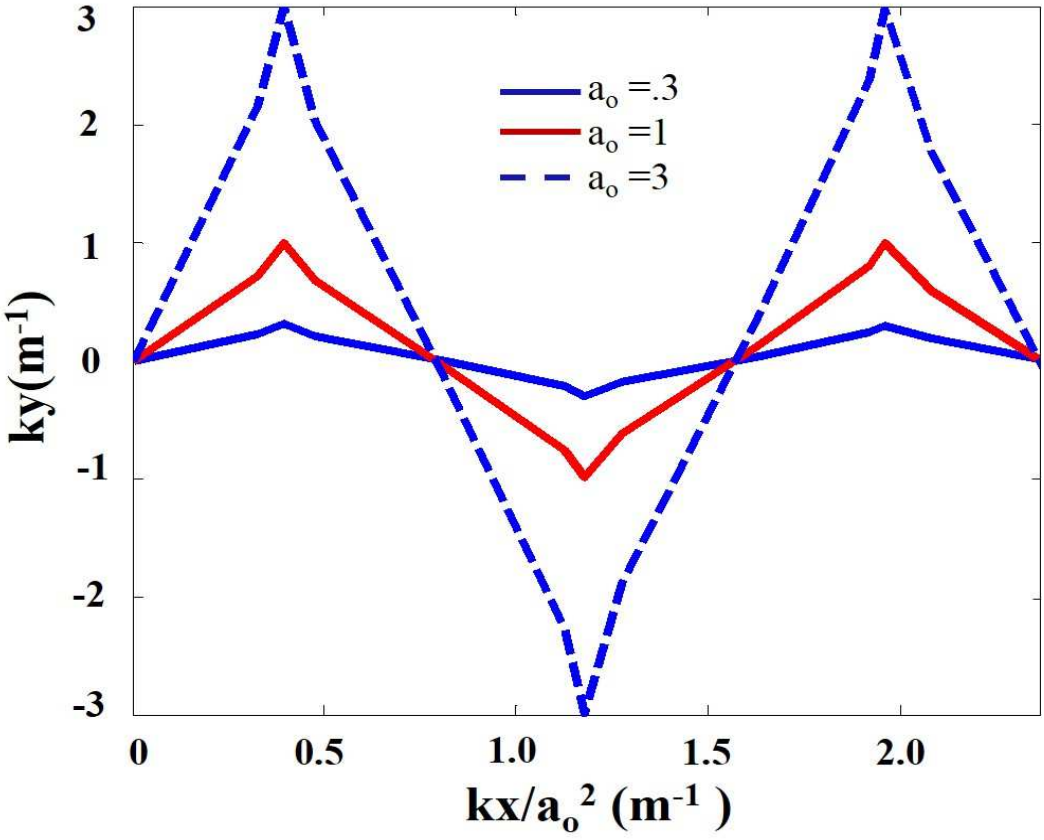

Figure 4: Electron motion in the presence of a large amplitude intensity EM plane wave. The values for a_o correspond to intensities of 10^{17}, 10^{18}, and 10^{19} W/cm^2.

At the target plane, lasers are tightly focused with large radial intensity gradients and a plane wave interaction with electron is not complete. The ponderomotive force, the gradient of the oscillation potential, describes electron motion at the focus. If we first consider the non-relativistic case, the equation of motion for an electron is

$$\frac{dv_y}{dt} = -\frac{e}{m} E_y(r) \tag{12}$$

with the EM wave propagating in the x-direction with a radial variation in the y-axis only. The electric field can be Taylor expanded

$$E_y(r) \simeq E_o(y)\cos(\omega t - kz) + y\frac{\partial E_o(y)}{\partial y}\cos(\omega t - kz) \tag{13}$$

and the velocity approximated to 2nd order $v_y = v_y^{(1)} + v_y^{(2)}$. Plugging back into the Lorentz equation, the 2nd order velocity term yields

$$\frac{\partial v_y^{(2)}}{\partial t} = -\frac{e^2}{m_e^2\omega^2} E_o \frac{\partial E_o(y)}{\partial y}\cos^2(\omega t - kz). \tag{14}$$

Multiplying by m_e and taking the cycle-average yields,

$$f_p = m_e\left\langle \frac{\partial v_y^{(2)}}{\partial t} \right\rangle = -\frac{e^2}{4m_e\omega^2}\frac{\partial E_o^2}{\partial y} = -\nabla U_p \tag{15}$$

which is the gradient of the ponderomotive potential. As the electron motion becomes relativistic, the force must be derived in a more rigorous, non-perturbative manner. One method is to define the oscillation center as a pseudo particle with an effective mass in the rest frame [31]. The relativistic ponderomotive force is most commonly expressed in the literature as

$$f_p = -m_e c^2 \nabla \gamma_{osc} \tag{16}$$

The ponderomotive force will serve to accelerate the electrons out of the focus at an angle as the equations of motion contain both transverse and longitudinal components.

The angle can be found using the momenta relation $p_{\parallel} = \frac{p_{\perp}^2}{2mc}$ which yields $\tan\theta = \frac{p_{\perp}}{p_{\parallel}} = \sqrt{\frac{2}{\gamma - 1}}$.

Chapter 3: Laser Interaction with Overdense Plasma

The laser-target interaction is governed by the characteristics of the laser pulse: energy, pulse duration, and temporal profile. A laser with low-contrast or long pulse duration will have to propagate through large amounts of plasma before reaching the critical surface. In this case, significant laser energy could be consumed prior to reaching the critical density surface. A high-contrast, short pulse laser will interact almost exclusively with an overdense target the front surface being the critical surface. The laser parameters determine the response of the target, i.e. melting, ablation, ionization, which in turn influences the further laser propagation.

Interaction processes can also be categorized according to laser intensity. The rapid increase in laser intensity has necessitated a large amount of effort to develop models that can accurately describe the physics occurring. Collisional effects seem to dominate the laser interaction until intensities reach $10^{15} W/cm^2$ [32]. At this intensity, the quiver velocity of the electron becomes comparable to the thermal velocity of the plasma thus reducing the collision frequency. Electron temperature has been found to generally scale with laser intensity $T_{Hot} \propto \left(I\lambda^2\right)^b$. Early experiments [50] involving resonance absorption or vacuum heating showing a scaling $T_{Hot} \approx 100keV\left(I\lambda^2\right)^{1/3}$ where λ is measured in microns and laser intensity in units of $10^{17} W/cm^2$. For comparison, an intensity of $1.5*10^{19} W/cm^2$ yields an approximate electron temperature of 500keV. At intensities approach $10^{19} W/cm^2$ a more appropriate scaling related to the ponderomotive potential is obtained [44]

$$T_{Hot} \approx .511\left[\left(1+\left(I_{17}\lambda_{\mu m}{}^2\right)/11.3\right)^{1/2}-1\right] \tag{17}$$

A generalized overview of laser processes compared to laser intensity is shown in figure 5.

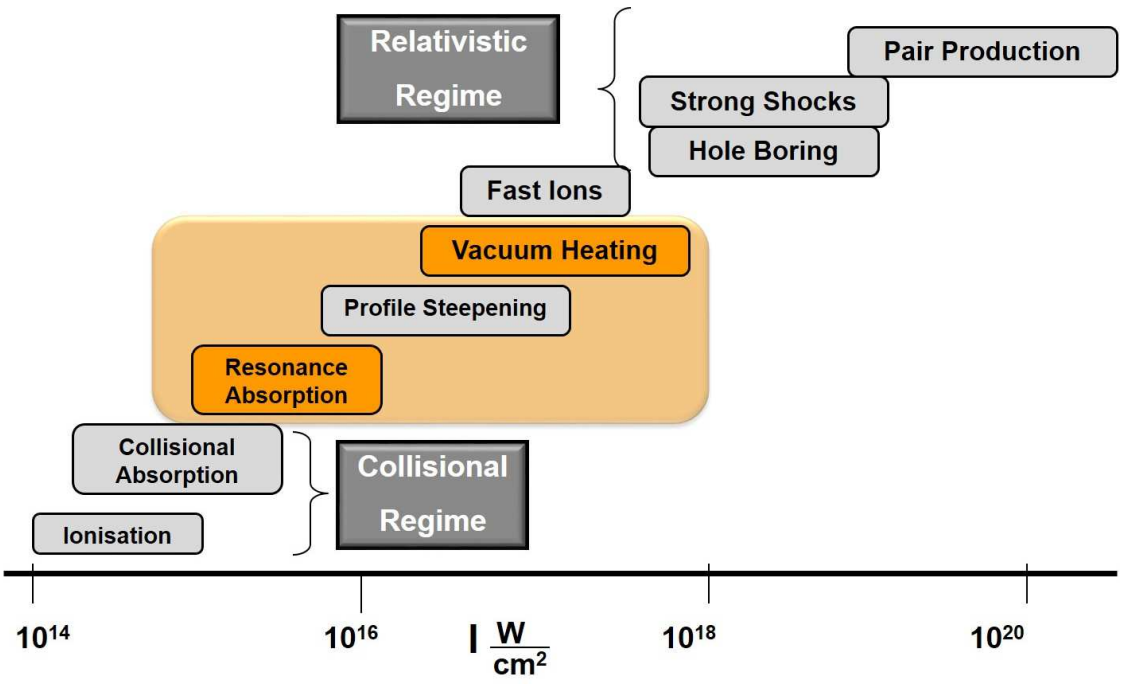

Figure 5: General overview of laser-target interactions as a function of laser intensity. Reproduced from [33].

3.1 COLLISIONAL ABSORPTION

One of the most fundamental laser-target energy conversions mechanisms is through collisions. As mentioned previously, the laser energy is preferentially transported to electrons through the electric field. The electrons then transport energy to the target via collisions with the ion lattice.

The Lorentz force equation for an electron now includes a collisional term [24]

$$m\frac{dv}{dt} = -e\left(E + \frac{v}{c}B\right) - m\nu_{ei}v \tag{18}$$

where ν_{ei} is the electron-ion collision frequency given by

$$\nu_{ei} = \frac{4(2\pi)^{1/2}}{3}\frac{n_e Z e^4}{m^2 v_e^3}\ln\Lambda \ . \tag{19}$$

In this equation, n_e is the electron density, Z is the number of free electron per atom, and $\ln\Lambda$ is the Coulomb logarithm with $\Lambda = \frac{b_{\max}}{b_{\min}}$ corresponding to the limits of the scattering cross section. $b_{\max}$ is the Debye length and $b_{\min}$ is the classical distance of closest approach. If we consider a plane wave propagating in the z direction on a slab of plasma, we obtain the wave equation

$$\frac{d^2E}{dz^2} + \frac{\omega^2}{c^2}\varepsilon(z)E = 0 \ . \tag{20}$$

Assuming a linear density profile, $n_e = n_{cr}\frac{z}{L}$ we obtain an expression for the dielectric function

$$\varepsilon = 1 - \frac{z}{L(1 + i\nu_{ei}/\omega)} . \tag{21}$$

The collision frequency dependence on density is neglected and the value for ν_{ei} is taken at the critical density. Plugging into the wave equation, yields the equation

$$\frac{d^2E}{dz^2} + \frac{\omega^2}{c^2}\left[1 - \frac{z}{L\left(1 + \frac{i\nu_{ei}}{\omega}\right)}\right]E = 0 . \tag{22}$$

Changing variables, this equation can be written $\frac{d^2E}{d\eta^2} - \eta E = 0$ which has the solution $E(\eta) = \alpha A_i(\eta)$. The function $A_i(\eta)$ is an Airy function and α is a constant chosen by matching the electric field at the vacuum-plasma interface, z=0. The electric field at the interface can be represented as an incident wave and a reflected wave multiplied by $e^{i\phi}$ where

$$\phi = \frac{4}{3}\left[-\eta(z=0)\right]^{3/2} - \frac{\pi}{2} \ . \tag{23}$$

The imaginary part of ϕ is the damping term and the fractional absorption due to collisional damping is

$$f_A = 1 - \exp\left(-\frac{8\nu_{ei}L}{3c}\right). \tag{24}$$

This analytical model assumed a smooth, linear density profile and $\nu_{ei}/\omega \ll 1$ which is rarely encountered with an ultrashort pulse incident on an overdense target. Low intensity absorption calculations with overdense targets are obtained through experimental observation calculating the reflected laser pulse using a Fresnel reflection model [34, 35]. Laser absorptions of up to ~50-60% at $10^{15} W/cm^2$ were measured.

3.2 THERMAL TRANSPORT

The laser deposits the majority of its energy in a volume $V \simeq l_s \pi r^2$ where l_s is the skin depth, and r is the laser focal spot radius. The energy of the laser pulse can then be transported in the form of a thermal wave described by the traditional heat flux equation [36] $Q = -\kappa \nabla T$ where Q is the heat flux, κ is the electron thermal conductivity and T is the electron temperature. The heat transport can be described as collisional or radiative depending on the material temperature. This thesis is primarily interested in thermal transport in the context of a low intensity laser pulse $\sim 10^{15} W/cm^2$. In this regime, only collisional effects are considered. The thermal conductivity can be expressed as $\kappa = \frac{1}{3}\lambda_{MFP} v_e c_v$ where v_e is the electron velocity, c_v is the specific heat, and λ_{MFP} is the electron mean free path. The mean free path is the electron velocity times the collisional relaxation time $\lambda_{MFP} = v_e \tau$. Substituting the coulomb collision relaxation time yields an expression for the heat conduction

$$\kappa = \frac{9\sqrt{3}}{16\pi} \frac{k_B (k_B T_e)^{5/2}}{\sqrt{m_e} Z e^4 \ln \Lambda} \tag{25}$$

Here $\ln\Lambda$ is the Coulomb logarithm which defines the maximum and minimum collision impact parameters. The thermal conductivity can be related to the electrical conductivity by the Wiedemann and Franz law $\frac{\kappa}{\sigma} \sim T$ which means for an ideal plasma $\sigma \sim T^{3/2}$. The heat flow into the target takes the form of a thermal wave with a self-similar solution which means the shape of the thermal wave remains constant as the wave propagates into the target. The depth of the heat wave can be given by [37]

$$x_f \simeq 65\left(\frac{n_e}{10^{23} cm^{-3}}\right)^{-7/9} Z^{-2/9}\left(\frac{I_{abs}}{10^{15}\frac{W}{cm^2}}\right)^{5/9}\left(\frac{t}{100\,fs}\right)^{7/9} nm\,. \tag{26}$$

If we assumed 20% absorbed light at an intensity of $5*10^{15} W/cm^2$, after 60ps the location of the heat front is ~5μm. The surface temperature can be estimated using the absorption coefficient for the normal skin effect [38]

$$T_e(0) = 119\left(\frac{n_e}{10^{23} cm^{-3}}\right)^{1/12} Z^{1/12}\left(\frac{I_{abs}}{10^{15}\frac{W}{cm^2}}\right)^{1/3}\left(\frac{t}{100\,fs}\right)^{1/6} eV\,. \tag{27}$$

Using the same laser parameters for the heating wave depth, a surface temperature of 130eV is obtained at a time of 150fs. These simple, analytical estimates can be compared to the results from a commercial Hydrodynamics code described in section 7.1

3.3 COLLISIONLESS ELECTRON TRANSPORT

3.3.1 Resonance Absorption

Consider a light wave incident at an angle θ on an inhomogeneous plasma slab with increasing density profile from 0 to critical density over a length, L. Figure 6 shows this scenario with y-z being the plane of incidence.

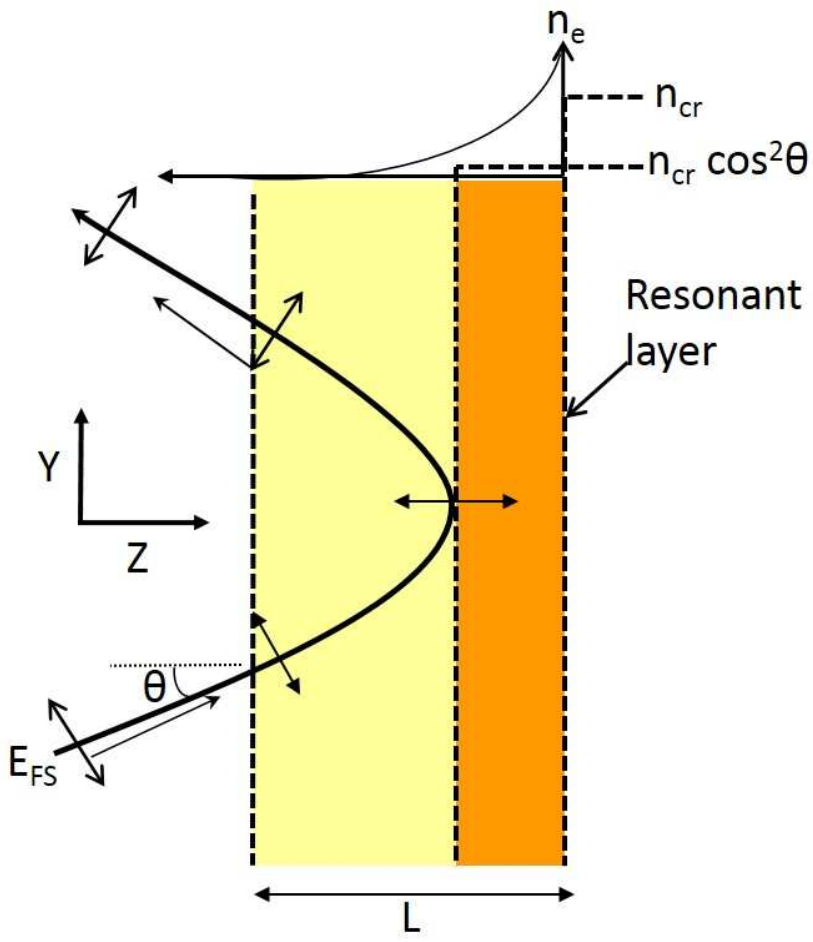

Figure 6: P-polarized light wave incident on a plasma slab at an angle θ.

Let's first consider a light wave polarized out of the plane of incidence, s-polarized. The wave is obliquely incident on the plasma surface and the wave equation can be written [24]

$$\frac{\partial^2 E_x}{\partial y^2}+\frac{\partial^2 E_x}{\partial z^2}+\frac{\omega^2}{c^2}\varepsilon(z)E_x=0 \tag{28}$$

where $E=E_x\vec{x}$ and y-z is the plane of incidence. The dielectric constant is a function of z only and k_y must be conserved. Plugging in to the wave equation yields

$$\frac{d^2E(z)}{dz^2}+\frac{\omega^2}{c^2}\left(\varepsilon(z)-\sin^2\theta\right)E(z)=0 \tag{29}$$

Since $\varepsilon=1-\frac{\omega_p^2(z)}{\omega^2}$, the laser will reflect at a density lower than the critical density as seen by $\omega_p=\omega\cos\theta$. The s-polarized wave has no component normal to the interface and is simply reflected.

If a light wave is polarized in the plane of incidence, $E=E_y\vec{y}+E_z\vec{z}$ or p-polarized, a component of the electric field exists that can drive electrons along the direction of the density gradient. Consider the same light wave obliquely incident on the plasma only now the wave is p-polarized. Using Poisson's equation, $\nabla\bullet(\varepsilon E)=0$ along with the vector identity

$$\nabla\bullet(\varepsilon E)=\varepsilon\nabla\bullet E+\nabla\varepsilon\bullet E \tag{30}$$

we obtain $\nabla\bullet E=-\frac{1}{\varepsilon}\frac{\partial\varepsilon}{\partial z}E_z$. When $\omega=\omega_p$, a resonance is driven due to $\varepsilon=0$. The light wave will again reflect at a density lower than then critical similar to the s-polarized case. However, it now possesses a field component along the density gradient which generates a standing wave at the turning point. The standing wave drives plasma oscillations along the density gradient. Although reflection occurs and the electron oscillations do not match the local plasma frequency, the fields can evanescently tunnel to the critical density and if the distance is not too great, the field begins to resonantly excite a plasma

wave. Electrons in the plasma wave then acquire energy from the laser driven oscillating field and are accelerated into the target through a process called wavebreaking [24].

In order to determine the energy transfer, the magnitude of the driving field must be calculated. This is most easily done by solving for the magnetic field and relating it to the electric field via Ampere's law. The relation can be written $E_z = \frac{\sin\theta * B(z)}{\varepsilon(z)} = \frac{E_d}{\varepsilon(z)}$ where the electric field normal component driving the resonance is E_d . The B-field is solved using the assumption of a linear plasma density. The solution is the Airy function with an exponential decaying term $B = A_i(\eta)\exp^{-\beta}$. We now obtain a solution of the driving field

$$E_d = \frac{E_{FS}}{\sqrt{2\pi\omega L/c}}\phi(\tau) \tag{31}$$

where $\phi(\tau) \simeq 2.3\tau\exp\left(\frac{-2\tau^3}{3}\right)$, $\tau = \left(\frac{\omega L}{c}\right)^{1/3}\sin\theta$ and E_{FS} is the electric field of the light wave in free space. $\phi(\tau)$ is plotted as a function of τ in figure 7. At normal incidence, the light wave has no component along the density gradient and nothing to drive the plasma oscillation. At large angles, the effect is diminished as the driver field must propagate through a large amount of plasma and the field is reduced when the critical surface is reached. In between the two angles, an optimal angle of incidence is given by $\left(\frac{\omega L}{c}\right)^{1/3}\sin\theta \simeq 0.8$.

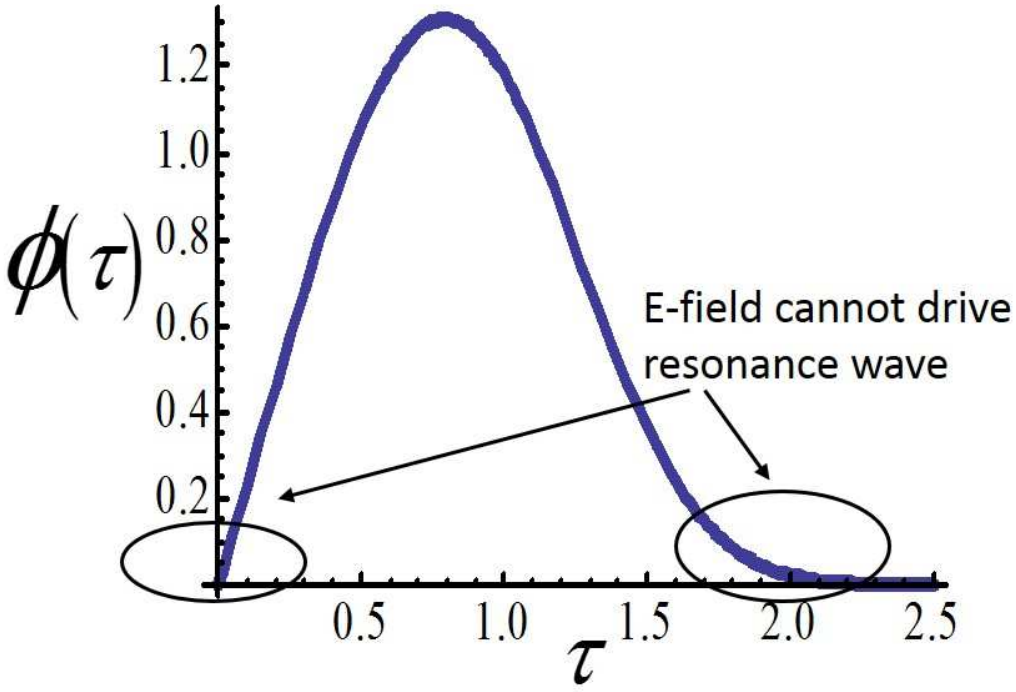

Figure 7: Resonance absorption as a function of τ.

3.3.2 Vacuum Heating

For resonance absorption, the plasma scale length was considered to be quite large $L \gg \lambda_o$. For short scale lengths, electrons can be accelerated via a different mechanism, vacuum heating. It was first proposed by Brunel [39] and has been verified experimentally [40]. Similar to Resonance Absorption, a p-polarized light wave is obliquely incident on a target. This time the interface is a sharp, overdense plasma. The electric field component normal to the interface can pull an electron out of the overdense target. Once out of the target, the electron is heated to $\sim v_{osc}$ and the field sends the electron back towards the target in one cycle. The light wave is stopped at the critical density while the electron is accelerated into the target. The target is modeled as a perfect conductor with an incident electric field $E(x,t) = E_L \sin(\omega t)$ and 100% light reflected [39]. The electric field is given by Poisson's equation on the surface

$$\Delta E = -4\pi e \int_{-\Delta x}^{x=0} n dx = 4\pi e n \Delta x . \quad (32)$$

The number of electrons pulled out into the vacuum is now known $n = \frac{N}{A\Delta x}$. Setting the two equations equal, relates the electron number to the electric field $\frac{N}{A} = \frac{2E_o \sin\theta}{4\pi e}$ the power absorbed per unit area is given by $\frac{1}{A}\left(\frac{dE_{abs}}{dt}\right) \approx \omega_o \frac{E_o \sin\theta}{4\pi e} \frac{1}{2} m_o v_o^2$. This can be written as

$$f = \left(\frac{\eta}{2\pi}\right)\left(\frac{v_{osc}^3}{v_L^2 c \cos\theta}\right) . \quad (33)$$

where η measures how much heating is lost to the plasma and found to be ~1.57. Numerical simulations conducted with intensities up to $10^{18} W/cm^2$ [41] have been performed that yield a wide range of absorption, 10-80%, depending on the input parameters. It was also observed that the hot electron temperature scales with the square root of intensity.

3.3.3 J x B Heating

Another electron acceleration mechanism that occurs on small plasma scale lengths is JxB Heating. As the light wave interacts with the target, electrons in the skin depth will oscillate perpendicular to the laser direction due to the ponderomotive force (eqn. 15). At relativistic intensities $> 10^{18} W \mu m^2 / cm^2$, the magnetic field becomes comparable to the electric field resulting in an additional force $\vec{J} \times \vec{B} = n_e m_e \vec{v}_{osc} \times \vec{B}$ directed along the k vector of the laser. Typical geometry of a laser interacting with a step-like overdense target is shown in figure 8.

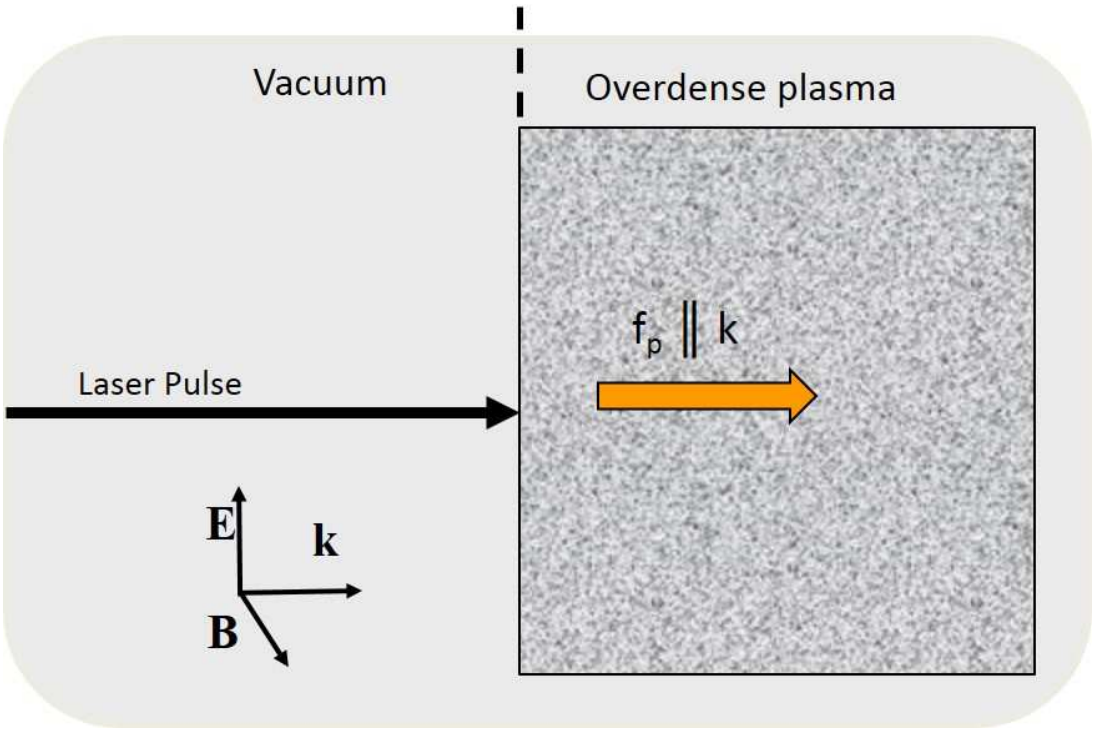

Figure 8: J x B heating with linear polarized light wave normally incident on an overdense plasma slab.

The relevant physics can be understood by first considering the nonrelativistic case. The force felt by the electrons from the laser is the ponderomotive force expressed as $F = -U_p$ where U is the ponderomotive potential described in eqn. 8. Assuming an electric field of the form $E = E_o(x)\hat{y}\sin\omega t$ and plugging into the ponderomotive force equation, the longitudinal component of the ponderomotive force can be written $F_x = -\frac{m}{4}\frac{\partial}{\partial x}v_{osc}^2(x)(1-\cos 2\omega t)\hat{x}$ with x the direction along the laser direction. This is the force felt by an electron a depth x inside the plasma. The oscillating 2nd term serves to accelerate electrons via an electrostatic field twice a laser cycle. Electrons oscillating in a preferential phase are accelerated into the overdense target while the laser is reflected

at the critical surface. J x B heating increases if more electrons can be accelerated. Two obvious examples of this are lasers at higher intensities propagating further into an overdense target or plasmas with lower densities up to the skin depth. It should be noted that the oscillating term arises for a linearly polarized beam, but is not present when the beam is circularly polarized. Relativistically, the Lorentz Force equation can be written in terms of an electron fluid element [43]. The equation of motion for the element is

$$\frac{\partial \vec{p}}{\partial t} + \vec{v} \bullet \vec{\nabla} \vec{p} = -e\left[\vec{E} + \frac{\vec{v} \times \vec{B}}{c} \right] \tag{34}$$

where $\vec{p} = \gamma m_o \vec{v}$ and $\gamma = \frac{1}{\sqrt{1 - \frac{v^2}{c^2}}} = \frac{1}{\sqrt{1 - \frac{\vec{p}^2}{\gamma^2}}}$. Eqn. 34 can be rewritten by replacing E and B with the vector, A, and electrostatic, φ potentials [44] and decomposing p into transverse and longitudinal components. The original equation now consists of two terms, a transverse

$$\frac{\partial p_T}{\partial t} = -\frac{e}{c}\frac{\partial A}{\partial t} \tag{35}$$

and longitudinal

$$\frac{\partial p_l}{\partial t} = e\nabla\phi - \frac{p \cdot \nabla p}{m_e \sqrt{1 + p^2/(m_e c)^2}} - \frac{e}{m_e c}\frac{p}{\sqrt{1 + p^2/(m_e c)^2}} \times \nabla \times A \tag{36}$$

component. Using a vector identity and rewriting in terms of the Lorentz factor, equation 36 can be expressed as

$$\frac{\partial \vec{p}_L}{\partial t} = e\vec{\nabla}\phi - m_o c^2 \vec{\nabla}(\gamma - 1) \ . \tag{37}$$

The first term is the electrostatic force while the second is the relativistic ponderomotive force that accelerates electron forward in the laser vector direction. The corresponding ponderomotive potential is expressed as $U_p = (\gamma - 1) m_e c^2$. Substituting $\gamma = \sqrt{1 + \vec{p}^2/2}$

for linearly polarized light, where $\vec{p}^2 = \frac{v_{osc}^2}{c^2}$ with $v_{osc} = \frac{eE_L}{m_e \omega_L}$ (eqn. 9) yields a hot electron temperature scaling for J x B heating [45]

$$T_{hot} \approx \left(\sqrt{1 + \frac{I\lambda_\mu^2}{2.8 * 10^{18}}} - 1 \right) 511 keV \tag{38}$$

Summarized in figure 9 are the operating characteristics of the three main electron acceleration mechanisms described – Resonance Absorption, Vacuum Heating, and JxB Heating.

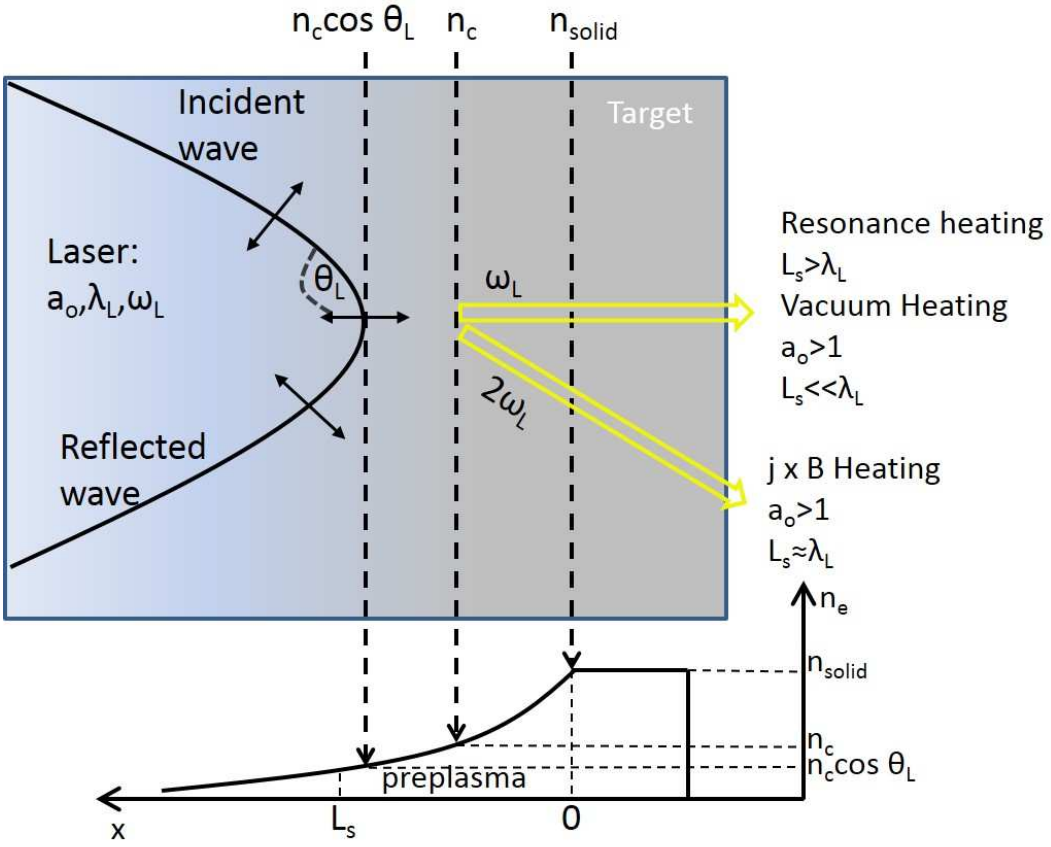

Figure 9: Laser – target characteristics of the three collisionless processes described – Resonance Absorption, Vacuum Heating, & J x B Heating. Reproduced from [42].

3.3.4 Skin Effects

The anomalous skin effect and sheath inverse-bremsstrahlung are two additional overdense target energy transfer mechanisms. Typically, electrons interact in a distance corresponding to the laser skin depth. At higher thermal velocities, the electrons can propagate a distance larger than the skin depth $\lambda_{mfp} > l$ into the material and deposit their energy. The field and the energy deposition are then nonlocal. For short pulses, the absorption coefficient is approximately [46] $\eta \approx \frac{2.8kl_s}{\cos\theta}$.

In sheath inverse-bremsstrahlung, the transit time of an electron through the skin depth is longer than the laser period [47]. The electron acquire energy from laser field oscillations in the skin layer. These two processes are analogous to Brunel heating in that they are present when the scale length is small and the laser is away from normal incidence. There are greatest when the plasma pressure is greater than the light pressure [30]

$$\frac{P_L}{P_E} = \frac{2 I_o / c}{n_e k_B T_e} \simeq \frac{660 I_{18}}{160 n_{23} T_{keV}} < 1 \tag{39}$$

For a 10keV plasma and a density $1*10^{23} cm^{-3}$, we get a value of 6 assuming an intensity of $1.5*10^{19} W/cm^2$. For our experiment, resonance absorption/vacuum heating should be the dominant heating mechanisms.

Chapter 4: Electron Propagation in Overdense Targets

As discussed previously, lasers propagate a skin depth into an overdense target at which the laser energy is deposited. Here we focus on the propagation of hot electrons generated by the collisionless acceleration processes described in Section 3.3. The total electric and magnetic fields generated in the target are described by Maxell's equations coupled to the material equations at all times.

$$\begin{aligned} \nabla \bullet E &= 4\pi e\left(n_o - n_e\right) \\ \nabla \times E &= -\frac{1}{c}\frac{\partial B}{\partial t} \\ \nabla \times B &= -\frac{4\pi}{c} j + \frac{1}{c}\frac{\partial E}{\partial t} \\ \nabla \bullet B &= 0 \end{aligned} \tag{40}$$

4.1 Electron Beam Characteristics

Electrons are accelerated a spatial scale roughly on the order of the laser spot size and length comparable to the laser pulse duration. For our experiment, we can assume a cylindrical shape approximately 15µm in diameter and 40µm in length. The energy distribution is approximately a Boltzmann energy distribution [48] although there are several experiments that describe evidence of a two temperature distribution [49, 50,51]. This distribution consists of a dense, lower energy bulk temperature combined with a much lower density tail of hot electrons.

Electrons with kinetic energy greater than the sheath field potential can escape the target. An electron bunch leaving the positively charged target creates a dipole with increasing length. For electron detachment, we consider the distance between the

electron bunch and the target to equal the geometric size of the bunch length [52]. For KE>PE, $\lambda_b - 1 > \frac{N_b r_c}{l}$ where γ_b is the bunch Lorentz factor, N_b is the number of electrons in a bunch, r_c is the classic electron radius, and l is the bunch length. For $l \sim 40\mu m$ and $N_b > 1^{10}$, the electrons escaping the target must have an energy ~1.5MeV.

4.2 ALFVEN LIMIT

If we consider a reasonable number of electrons $N \sim 1*10^{12}$, accelerated by the laser, we obtain a current of 1MA. Using the cylinder geometry of the previous paragraph, a magnetic field of 10,000T exists on the surface of the cylinder. The energy in the magnetic field is proportional to $\left(\frac{B^2}{2\mu_o}\right)\pi r^2 L \ln\left(\frac{L}{r}\right)$ where L is the electron propagation distance into the target and r is the electron beam radius. Plugging in the experimental values, yields a value of 5J which is larger than the input laser energy. This suggests there is an opposing field compensating or limiting the value. Currents of this limit have been shown to be unstable [53] and must obey a limit called the Alfven limit $I_A \simeq 17000\gamma\beta(A)$ where $\beta = \frac{v}{c}$ and γ is the relativistic Lorentz factor. The limit was derived for monoenergetic, uniform cosmic rays with a neutralizing background, but the physics is extremely relevant to our case. The electron current generates a magnetic field. As the current increases, so too does the magnetic field. As the Alfven limit is approached, the outermost electron trajectories are deflected perpendicular to the propagation axis by the magnetic field. This can be observed by solving the radial equation of motion for an electron in a constant magnetic field. For a beam of radius r_o, electron velocity v_o, electron radial velocity v_r, electron axial velocity v_z and $\beta_o = \frac{v_o}{c}$,

this can written in terms of dimensionless variables $R = \frac{r}{r_o}, V_r = \frac{v_r}{\beta_o c}, V_z = \frac{v_z}{\beta_o c}, \tau = \frac{t}{r_o / v_o}$

[54]. The resulting equations are

$$\begin{aligned} \frac{dR}{d\tau} &= V_R, \\ \frac{dV_R}{d\tau} &= -\frac{I}{\left[4\pi\varepsilon_o c^3 \beta_o \gamma_o / e\right]} \frac{2V_z}{R}, \\ V_z &= \left(1 - V_R^2\right)^{1/2} \end{aligned} \tag{41}$$

The term in brackets is the Alfven current I_A, V_R is the electron radial velocity, R is the normalized radius, τ is the normalized time, and V_z is the axial velocity. The particle trajectories for different values of I / I_A are shown in figure 10.

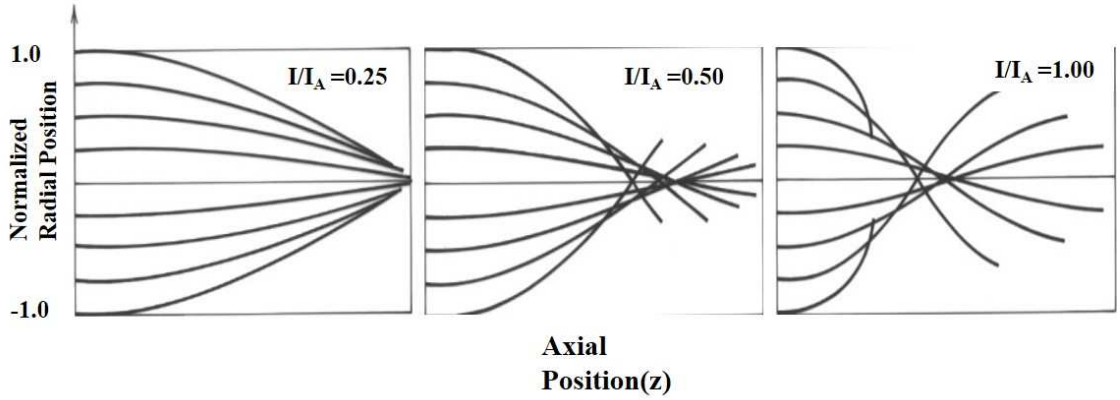

Figure 10: Single electron orbit in a constant magnetic field generated from a uniform current. Reproduced from [53].

The particle trajectories are approximately harmonic at low ratios of I / I_A. Increasing the current increases the radial velocity in turn reducing the particle oscillation period. As the ratio approaches 1, the outermost particles are deflected until they have zero axial velocity. The process is then self-limiting. This can be potentially overcome by an opposing magnetic field from a return current opposing the hot electrons [55].

4.3 RETURN CURRENTS

As the hot electrons penetrate inside a target, they produce an electrostatic field. To preserve charge neutrality, bulk electrons flow in the opposite direction providing a return current. Charge neutrality occurs in a time given by $\Delta t \approx \frac{2\pi}{\omega_p} = 1.77 * 10^{-5} n_e^{-1/2}$ [56]. For densities above $10^{22} cm^{-3}$, $\Delta t \approx 10^{-15} s$. Return currents have been observed experimentally [57] but in reality measuring return currents in a solid density target is quite difficult. So, it is universally presumed that the hot electron current is balanced by a return current $j_f \simeq -j_r$ [58] for a conducting medium. The electric field generated by the hot electrons is related to the current via Ohm's law, $j_r = \sigma E$ where σ is the material conductivity. The electrons heat the target through collisional heating that can alter the conductivity of the medium.

A simple heating model has been developed [49] assuming complete current neutralization $j_f \simeq -j_r$. The deposited energy per volume is related to the return current by

$$C_v \frac{d}{dt} T_e = E \bullet j_f = \frac{j_r^2}{\sigma} \tag{42}$$

where T_e is the cold electron temperature, C_v is the heat capacity, and σ is the electrical conductivity. The heat capacity and conductivity are functions of temperature and are computed at each time step. The heat capacity is modeled as an ideal gas $C_v = \frac{3}{2} k_B n_e$. The background electron density is written as $n_e = Z^* n_i$ and is a function of temperature through the ionization state modeled through More's formula of the Thomas-Fermi model [59]. The conductivity is adapted from a hydrodynamic simulation model [61]. Figure 11 shows the time evolution of resistive heating for three different hot electron

current magnitudes from $1*10^{12} A/cm^2$ to $1*10^{13} A/cm^2$ which approximate the experimental observed value.

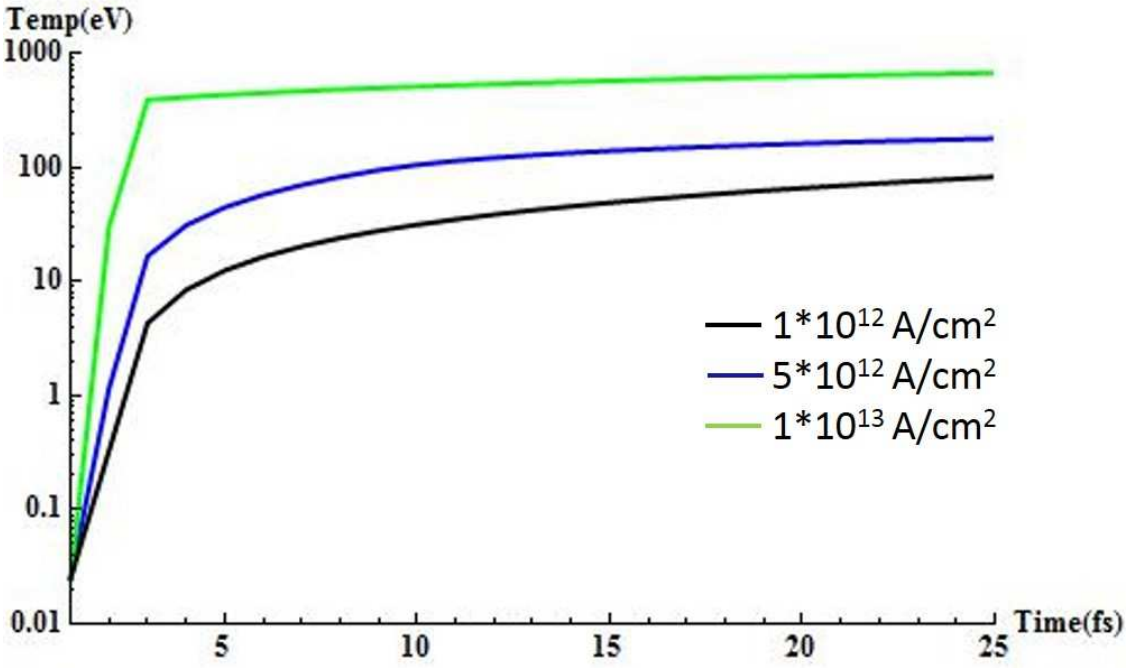

Figure 11: Time evolution of the bulk electron temperature as calculated using equation 42. Hot electron current was assumed to be 1MA contained in a cylinder of radius ~4μm. The return current is calculated at the surface of the hot electron beam.

4.4 ELECTRICAL CONDUCTIVITY

The Drude model depicting a metal as immobile ions surrounded by a free electron gas is the starting point for deriving electrical conductivity [62]. If we consider electrons moving in a wire, the current density is given by $j = n_e ev$ where e is the electron charge, n_e is the number of electrons, and v is the average electron velocity. When an external electric field is applied, the average electron velocity can be written as

$v_{avg} = -\frac{eE\tau}{m}$ where τ is the average collisional relaxation time. Plugging in the average velocity, yields an expression for the current density $j = \left(\frac{n_e e^2 \tau}{m}\right) E$ which is related to the conductivity through $j = \sigma E$. The conductivity of a metal is then written $\sigma = \frac{n_e e^2 \tau}{m}$.

The free electron gas model can also calculate the conductivity as a function of frequency. Consider an external electric field applied to a metal, the electron momentum equation of motion is written.

$$\frac{dp_e}{dt} = -\frac{p_e}{\tau} - eE \quad . \tag{43}$$

A solution is written in the form $p_e(t) = \mathrm{Re}\left(p_e(\omega)\exp(-i\omega t)\right)$ and plugged into the equation of motion. The current density can then be written as $j(\omega) = -\frac{n_e e p_e(\omega)}{m} = \frac{\left(n_e e^2/m\right)E(\omega)}{(1/\tau) - i\omega}$. The frequency dependent conductivity is then

$$\sigma(\omega) = \frac{\sigma_o}{1 - i\omega\tau} \tag{44}$$

where $\sigma_o = \frac{n_e e^2 \tau}{m}$.

High intensity laser interactions with overdense targets are characterized by rapid heating with plasma temperatures of ~1keV are common for laser intensities of $1*10^{19} W/cm^2$. For a short pulse laser, this means the target changes from a degenerate solid to a fully ionized nondegenerate plasma at solid density. In the degenerate limit, the electron distribution is described by the Fermi-Dirac distribution [60] $f(\varepsilon) = \frac{1}{\exp\left(\varepsilon - \mu / kT\right) + 1}$ where μ is the chemical potential, kT is the temperature and ε is the energy. The distribution gives the probability that a state with energy ε and chemical potential μ is occupied by fermions (electrons). At absolute zero, T=0K, the electrons fill up all available states according to the Pauli Exclusion principle beginning

with the lowest energy states available up to the Fermi energy $E_F = \frac{\hbar^2}{2m}\left(3\pi^2 m_e\right)$. Above the Fermi energy, no state is occupied and the distribution resembles a step function. At this temperature, the chemical potential is referred to as the Fermi energy. The Fermi energy in metals is quite large ~5-10eV and so the step function condition is a good approximation at room temperatures. At temperatures slightly above room temp, only the electrons in the range +/-kT will be able to contribute. When the energy equals the chemical potential, the distribution is ½ regardless of the temperature. This means half the electrons are in the degenerate state and half have been promoted to an excited state. These distributions are plotted in figure 12.

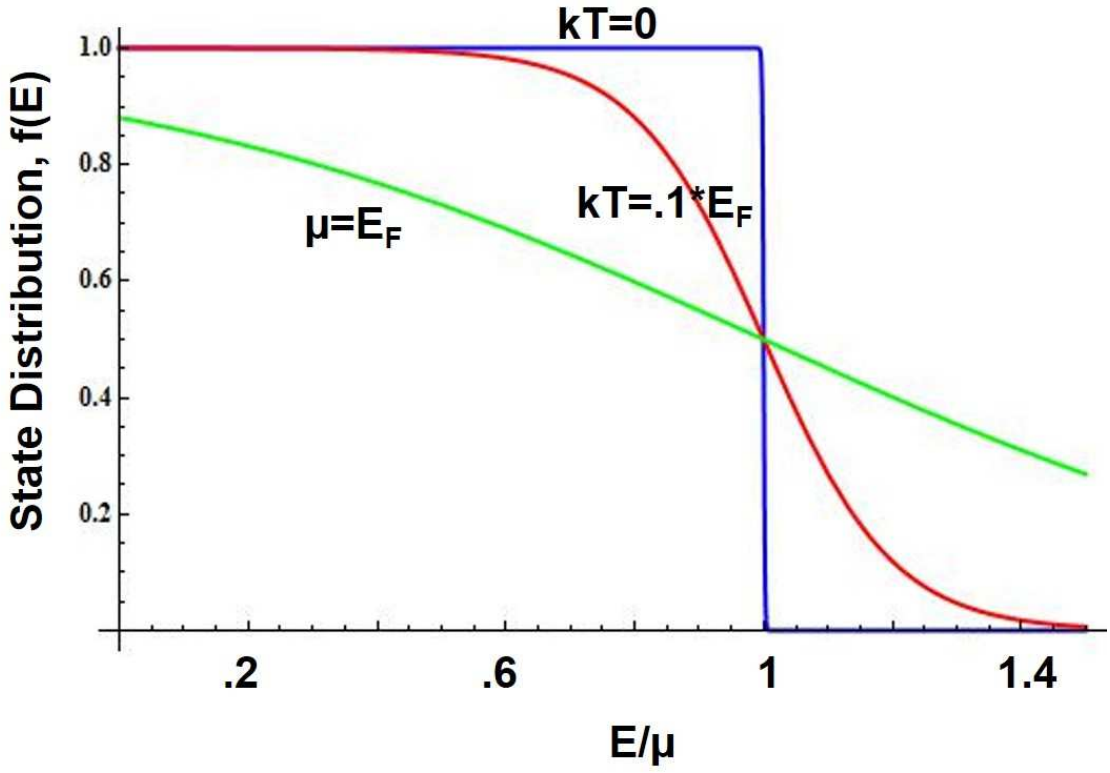

Figure 12: The Fermi-Dirac distribution at different temperatures.

The Fermi energy can be referred to as the Fermi temperature, T_F as plasma distributions are typically described in terms of temperature. At temperatures greater than T_F, the chemical potential becomes negative as more than half of the electrons are in excited states. At $T>>T_F$, the Fermi distribution then approximates an ideal gas. The chemical potential for a classical ideal gas is $\mu = -kT \ln\left(\frac{Z}{N}\right)$. The occupancy of single states is then very small analogous to an ideal gas obeying a Maxwell-Boltzmann distribution.

The Fermi energy can be related to the material conductivity through the band structure of the material. In a single atom, electrons orbits the nucleus in discrete energy levels. When large number of atoms are combined to for a macroscopic solid, the energy levels merge together to form broad bands. A material can be classified according to its representative band structure. The band structures of a metal, semiconductor and insulator are shown in figure 13. In a metal, the Fermi energy is located in the conduction band while in an insulator the Fermi energy is located in the band gap between the conduction and valence band. Only electrons with enough energy equivalent to the band gap energy can be excited to the conduction band.

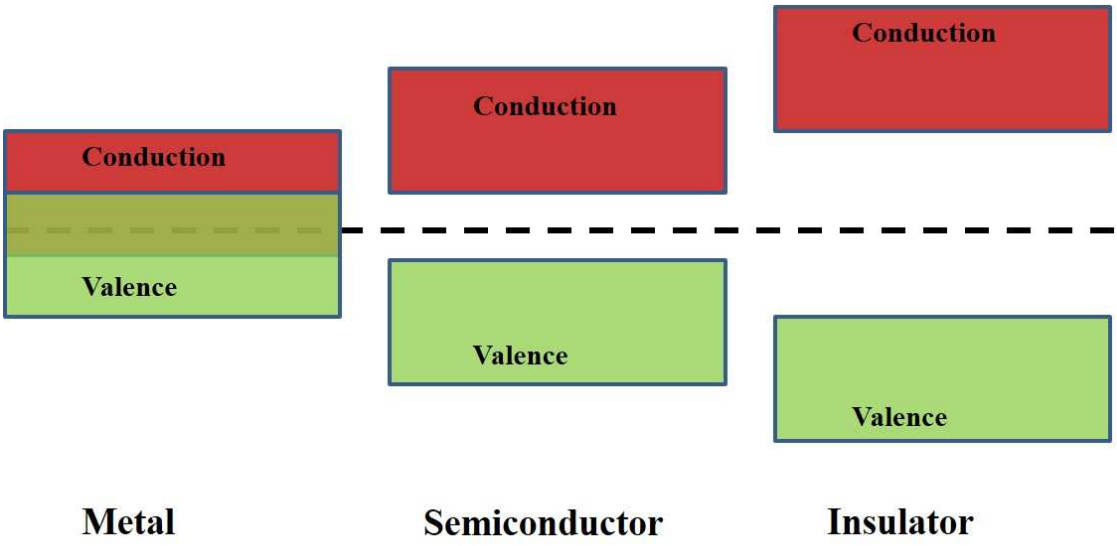

Figure 13: Fermi level location in band structure of a metal, semiconductor and insulator.

If we consider that the melting temperature of Al is ~.1eV then it becomes clear that the Drude model alone cannot explain conductivities observed in high intensity laser solid target interactions. A more comprehensive model is required to accurately describe the change in conductivity from a solid to plasma as a function of temperature. The Lee and More model solves completely the transport coefficients obtained from the solution of the Boltzmann equation in the relaxation time approximation [63]. A full quantum mechanical model using quantum molecular dynamics based on density functional theory [64]. A qualitative plot of aluminum conductivity versus temperature is shown in figure 14 using the equations from a hydrodynamic simulation model [61].

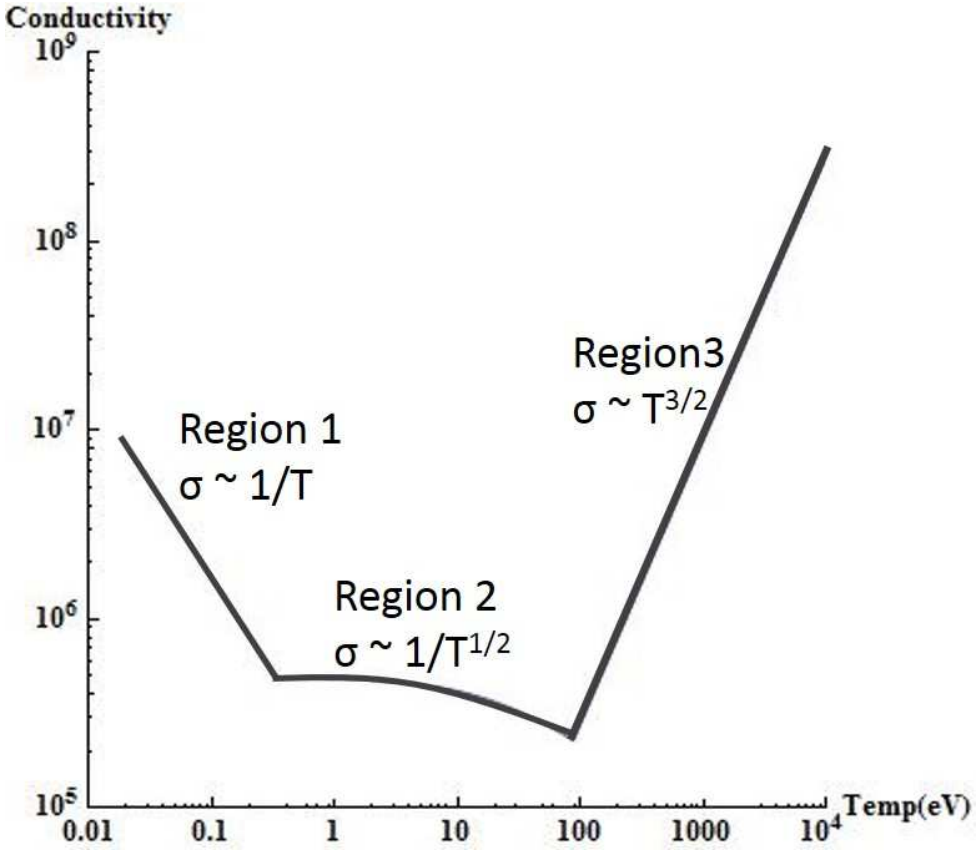

Figure 14: Log plot of aluminum conductivity versus temperature. The three regions are based on different electron collisional models given in Ref [58].

The plot was generated using conductivity in the form $\sigma = \frac{n_e e^2}{m\nu}$ where ν is the electron collision frequency. The plot shows three different regions: 1, 2, and 3 with each region having a unique electron collisional model. The different models yield different conductivity temperature dependences.

4.4.1 Region 1 – Solid state Conductivity

The conductivity in region 1 is governed by traditional solid state theory. The electron collisional frequency is dominated by collisions with phonons. As the temperature is increased $T \gg T_{Debye}$, the phonon wavelength is on the order of the lattice

spacing $\lambda \simeq a_o$. The scattering of electrons occurs predominantly through thermal vibrations of the ions. The rms amplitude of the ion motion is directly related to the temperature $M_i \omega_o^2 \left\langle r^2 \right\rangle \simeq T$. The electron-phonon relaxation time can be expressed as $\frac{1}{\tau} = n_i v_F A \simeq n_i v_F \left\langle r^2 \right\rangle \simeq \frac{1}{a_o^3} \frac{1}{m_e a_o} \frac{T}{M_i \omega_o^2}$. When the relaxation time is plugged into the conductivity, we see that the conductivity scales as $\sigma = \frac{n_e e^2 \tau}{m_e} \sim \frac{1}{T}$. This can also be understood by considering that the phonons in any normal mode are given by [62] $n(q) = \frac{1}{e^{\beta \hbar \omega(q)} - 1} \approx \frac{k_B T}{\hbar \omega(q)}$. The total number of phonons on the surface of allowed wave vectors for the scattering of a given electron is proportional to T. Since the number of scatters scales with T, so will the resistivity $\rho \sim T$.

At room temperature, we can use our knowledge of the material band structure to estimate the difference in conductivity between a metal and an insulator. For aluminum, which has three conduction electrons, the density of conduction electrons is $1.8*10^{29}$ m^{-3}. For polyethylene, which has a band gap of ~7.5eV [65] we can solve for the density by integrating the Fermi distribution over the density of states ~ $N \simeq \frac{2V}{v_Q} \exp\left[-\Delta\varepsilon \big/ kT \right]$ where V is the volume, $\Delta\varepsilon$ is the bandgap energy, and v_Q is the quantum volume. The exponent is $\exp\left[-1.5eV \big/ .025eV \right] \sim 4*10^{-26}$ where the distance from the Fermi level to the conduction band is 1.5eV and the quantum volume is $v_Q = \left(\frac{h}{\sqrt{2\pi m k T}} \right)^3 \simeq 8*10^{-26} m^3$. The density of conduction electrons is given by $\frac{N}{V} = \frac{2*\left(4*10^{-26}\right)}{8*10^{-26} m^3} \simeq 1 m^{-3}$ which is quite nonconductive.

4.4.2 Region 3 – Ideal Plasma (Spitzer) Conductivity

As the temperature increases (>100eV), the target becomes a fully ionized, non-degenerate plasma and collisions are dominated by coulomb collisions. The change of momentum for a large angle collision is $\Delta(mv) = \frac{e^2}{r_o v}$ where v is particle velocity and r_o is the impact parameter. The cross section is written as $\pi r_o^2 = \frac{\pi e^4}{m^2 v^4}$ and increasing the temperature serves to decrease the cross section as a function of velocity $\sim 1/v_e^4$. The collision frequency is written in terms of the cross section $\nu_{ei} = n\sigma v$ and is given by [66]

$$\nu_{spitzer} = \frac{4}{3}(2\pi)^{1/2} \frac{Z_{avg} e^4 m_e n_e}{(m_e k_B T_e)^{3/2}} \ln\Lambda \tag{45}$$

where Z_{avg} is the ionization degree, T_e is the electron temperature, and $\ln\Lambda$ is the coulomb logarithm. Λ is defined as $\frac{\lambda_D}{r_o}$ which is the ratio of the maximum/minimum collisional impact parameter. λ_D is the Debye length. The conductivity is called the Spitzer conductivity and written as

$$\sigma_{Spitzer} = \frac{3}{4\sqrt{2\pi}} \frac{(k_B T_3)^{3/2}}{Ze^2 m_e^{1/2} \ln\Lambda}. \tag{46}$$

4.4.3 Region 2 –Warm Dense Matter Conductivity

In this temperature regime, 1eV - 100eV, neither solid state nor traditional plasma theory adequately describe the governing physics. The material is no longer solid with transition to metal occurring (Al at 1eV is ten times greater than the melting temperature) while at constant density. At temperatures exceeding the Fermi temperature $(T_F \sim 10eV)$, an extremely large number of energy bands is required in addition to dealing with multiple particle species. Traditional plasma physics theory is not applicable due to the strong degeneracy within the dense plasma. This can be observed through the plasma coupling parameter which is the ratio of the potential energy to the thermal energy

$\Gamma = \frac{Ze^2}{r_o kT}$. Z is the atomic number of the atom and r_o is interatomic distance $r_o = \left(\frac{3}{4\pi n}\right)^{1/3}$. At these densities and temperatures, the plasma has a coupling ratio of ~1 meaning electron degeneracy must be addressed and strong ion correlation exists. The degeneracy reduces the number of electrons available to participate in conduction and as such the Spitzer conductivity overstates the electron conductivity by a large factor [62]. This is represented in the Coulomb logarithm term which give the upper and lower cutoffs for a Coulomb scattering event. At high temperatures and low densities, the maximum screening length of the plasma is governed by the Debye length which is not applicable for the densities encountered here. To correct for the electron degeneracy, the electron contribution is multiplied by the logarithm derivative of the Fermi Integral which represents the ratio of the actual field density to the free field density. The Debye shielding is modified as $\frac{1}{\lambda_{DH}^2} = \frac{4\pi n_e e^2}{kT_e}\frac{F_{1/2}^{'}}{F_{1/2}} + \frac{4\pi n_I (eZ)^2}{kT_I}$ where T_e and T_I are the electron and ion temperatures respectively. The following approximation can be made to avoid the computation of the Fermi integrals $T_e = \left(T_e^2 + T_F^2\right)^{1/2}$. The approximation was found to match within 5% of the Fermi integral [67] and provides a smooth fit between the solid state and ideal plasma regimes. A similar argument can be extended to the lower cutoff parameter, the denominator in the Coulomb logarithm. In a non-generate, high temperature plasma, the parameter is described by the classical distance of closest approach $b_o = \frac{Z_1 Z_2 e^2}{m v_e^2}$ at low energies and the uncertainty principle at high energies $\frac{\lambda}{2} = \frac{h}{2mv} = \frac{h}{2(3mkT_e)^{1/2}}$ with λ being the de Broglie wavelength. At these temperature and density conditions, the screening length of the plasma becomes less than the interatomic distance r_o. When this occurs, defining a collisional impact parameter less

than the interatomic distance is not valid. Therefore, we seek to express the minimum impact parameter in the context of the uncertainty principle. At the fully degenerate limit, the minimum parameter is expressed as $\frac{\lambda}{2} = \frac{h}{2\left(3mkT_F\right)^{1/2}}$ where the electron temperature is replaced by the Fermi temperature. In a similar manner to the max impact parameter, we can connect the de Broglie and Fermi wavelength by the interpolation $b_{\min}^2 = \frac{h^2}{12mk\left(T_e^2 + T_F^2\right)^{1/2}}$ [67].

In section 4.4.1, we derived the number of conduction electrons as $N \simeq \frac{2V}{v_Q}\exp\left[-\Delta\varepsilon \big/ kT\right]$. In this region, let's consider the material hot enough to completely bridge the band gap in an insulator, i.e. $\exp[-\frac{\Delta\varepsilon}{kT}] \approx .5$. The number of conduction electrons is now $\sim 1*10^{25} m^{-3}$. The number of electrons begins to approach to number of electrons in aluminum at room temperature. At the temperatures and density of WDM, the conductivity is not trivial, but it can be easily inferred that the conductivity of an insulator and a metal could be quite favorable around the Fermi temperature.

In the context of the conductivity model presented here, the dense plasma effects on the collision frequency can be understood by noting that the electron mean free path becomes less that the interatomic distance. If we require the mean free path to be not less than the ion sphere radius [61] $\lambda_{MFP} > \left(\frac{3}{4\pi n_i}\right)^{1/3}$, this is identical to requiring the collision relaxation time be $\frac{1}{\tau} < \frac{v_e}{r_o}$ where r_o is the ion sphere radius and v_e is an electron velocity. The electron velocity is an interpolation between regions 1 and 3 $v_e = \left(v_F + \frac{k_B T_e}{m_e}\right)^{1/2}$. Plugging the relaxation time into the conductivity formula, we get

$$\sigma = \frac{e^2 n_e}{m_e} \frac{\left(\frac{4}{3}\pi n_i\right)^{-1/3}}{\sqrt{2/m_e\left[\left(3/2kT_e\right)^2 + \left(3/2kT_F\right)^2\right]^{1/2}}} \sim \frac{1}{T^{1/2}}. \quad (47)$$

4.5 ADDITIONAL ELECTRON PROPAGATION EFFECTS

The laser has accelerated a small population of hot electrons whose motion is opposed by a current of colder electrons in the bulk of the material. The interaction of the counterpropagating currents and their respective fields greatly influences the characteristics of the hot electron transport. Any anisotropy in this interaction will lead to changes in the current density distribution resulting in filamentation.

In this specific experiment, the electrons are propagating through a thin, 1.5 micron target. This is relevant because virtually all comparable experimental data in the literature is measured with thicker targets from 10-100 μm. Also, our diagnostic of transition radiation measures only the high energy tail of the accelerated electrons. Each electron bunch accelerated by the laser propagates through the target in approximately 5 fs with the entire population of hot electrons passing through the target in roughly 100 fs. The experimental observations of the number of filaments and occurrence with experimental parameter are shown in figures 15 and 16. Typical images of 1ω filaments from both an aluminum target and an Al/plastic target are shown in figure 17.

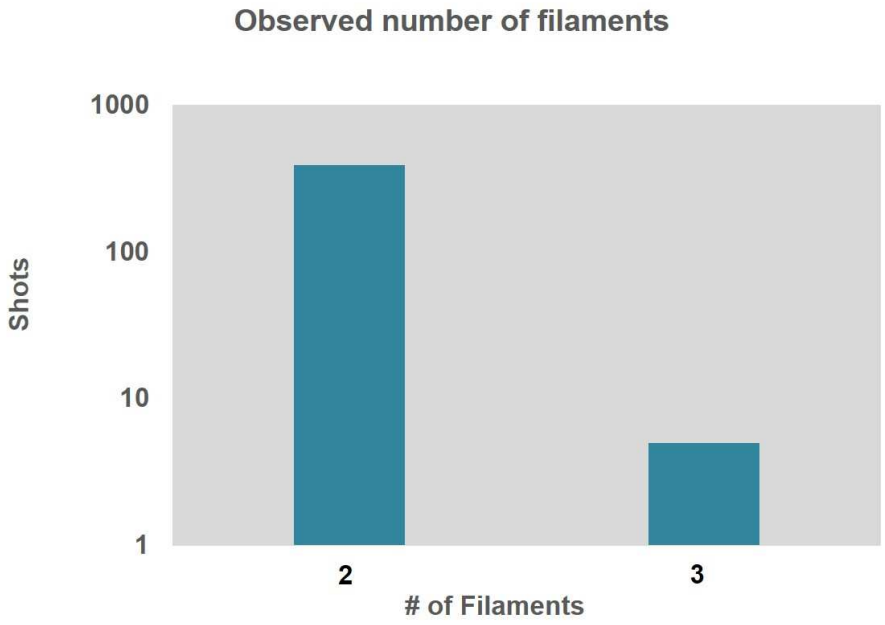

Figure 15: Number of filaments observed for all targets.

Figure 15 shows that two filaments are observed in the majority of cases with only five instances of three filaments out of almost 400 total. Figure 16 shows the frequency of filament occurrence by experiment type. In aluminum, filaments were observed in approximately 7% of all shots. This is contrast to the Al/plastic target with filaments occurring in almost 30% of the targets. In aluminum targets, there is little difference in the frequency of filament occurrence for both acceleration processes – 1ω, 2ω radiation and whether the target is heated/unheated. The next few paragraphs will introduce some of the standard mechanisms attributed to filament generation and evaluate their influence in the context of the experimental results shown above.

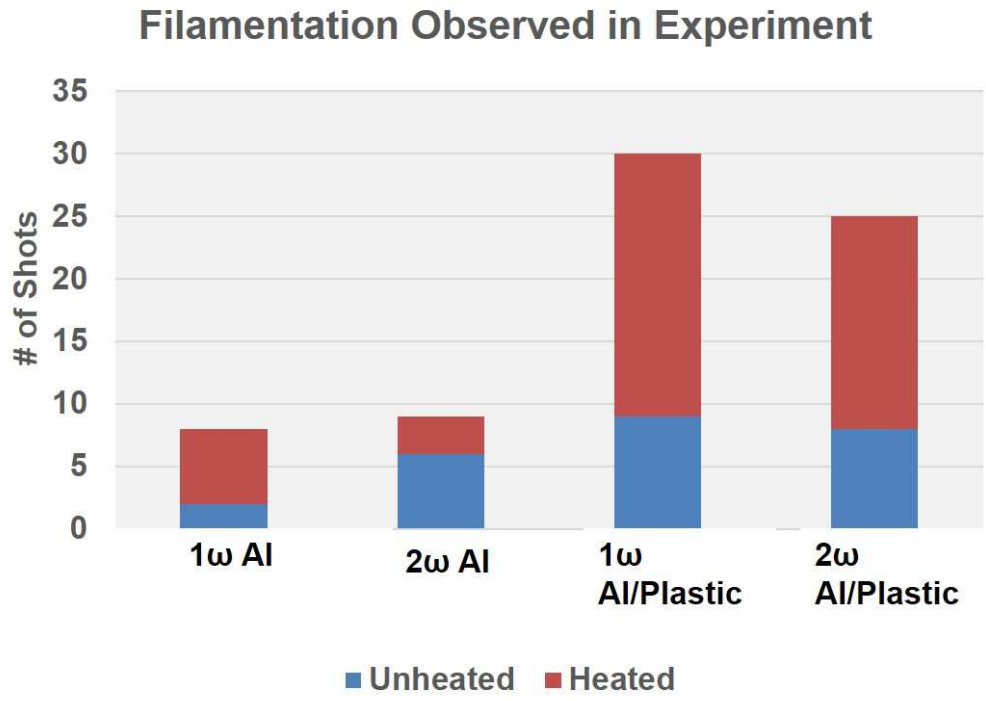

Figure 16: Frequency of filament occurrence as a function of experimental parameter.

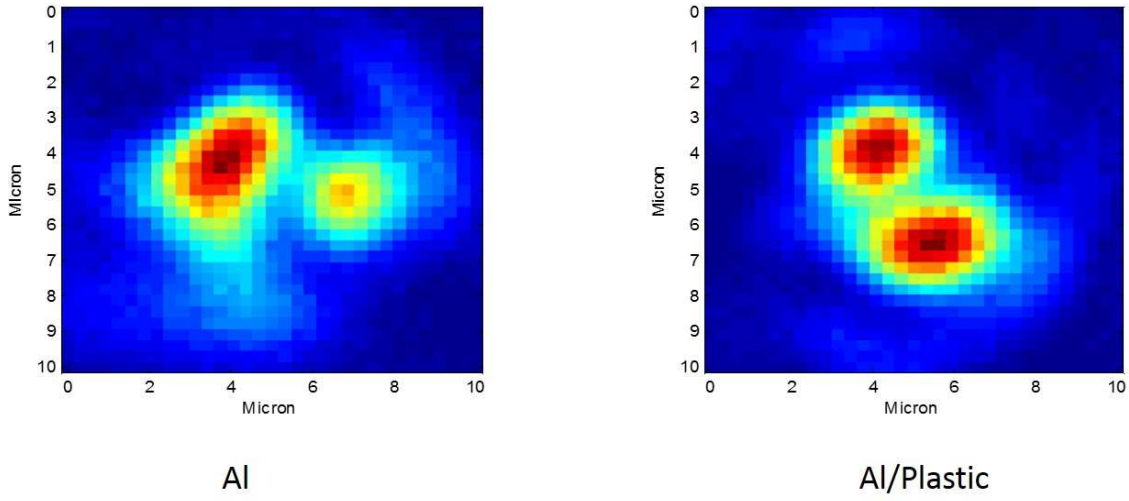

Figure 17: Typical images of 1ω filaments. Al target is on the left and Al/plastic is on the right. The viewing window is 10 x 10 µm.

Both the hot electron and opposing return current have magnetic fields associated with them. Any perturbation of the magnetic fields leads to displacement of that currents which in turn further amplifies the magnetic field. This process is called the collisionless Weibel Instability [68]. As the currents are separated transversely, current neutralization goes away and the beam filaments. The instability can be suppressed if the outward thermal force of the electron beam can balance the magnetic force [69]. Consider an electron beam with density n_B and radius r_o moving through a solid with density n_o. The magnetic field with exert a pinching force on the electron beam given by $F_{pinch} \approx 2e^2 n_B r_o (v_B/c)$ [70]. The electron beam has a temperature and divergence which generate a thermal pressure $F_P \approx \frac{k_B T}{r_o}$ causing the electron beam to expand. The ratio of the forces yields a threshold condition for filamentation to occur $\frac{n_B}{n_o} > \frac{2\pi k_B T}{m_e c^2}$ when the beam radius is considered to be a filament of size $r_o \approx \frac{c}{\omega_p}$ which is equivalent in size to the collisionless skin depth. It should be noted that the skin depth dimension is approximately .1μm which is less than the spatial resolution for this experiment (~2 μm). In calculating the beam number, the beam was approximated as a cylinder with radius 4μm and length cτ where τ is the laser pulse duration. From CTR analysis in section 7.5.2, the number of hot electrons was determined to be ~1.4*10^{12}. This yields a beam density of 1*10^{27} m^{-3} which gives a ratio of $\frac{n_B}{n_o} \sim .01$ with the plasma. For this experiment, the condition for filamentation $.01 >\sim 10$ is not satisfied and this instability doesn't becomes important until the beam encounters plasma regions of low density. Additionally, the growth rate can be expressed as a function of the beam density $\Gamma_{weibel} \approx \omega_B \left(\frac{n_B}{\gamma n_o} \right)^{1/2} \frac{v_B}{c}$ where v_B is the beam velocity and ω_B is the beam frequency.

Assuming the same beam density in our previous analysis, yields a growth rate of 17 fs which corresponds to a distance of 5 μm a distance three time longer than the targets used here. Features attributable to the Weibel instability have been observed experimentally in low density targets (foams) and overdense targets with an induced plasma [71, 72]. In the case of [71], a plasma was generated on the rear surface by a 2nd laser pulse. The electrons exiting the target propagated through a plasma with a decaying density profile with the critical density as a maximum. The electrons eventually propagated through a density region suitable for the instability to occur.

The influence of the magnetic field on hot electron propagation has been characterized [73] by solving the Fokker-Planck equations. As the laser intensity increases, the magnetic field plays a greater role in the electron propagation. At intensities $\sim 10^{18} W / cm^2$, the magnetic field reduces the radial spread of the electrons and increases the electron penetration depth when compared to purely collisional models. This has been observed in both simulations [74] and experiments [75]. However, there have been contradictory simulations [76] which show deflection of electrons from the magnetic field highlighting the complexity of the problem.

The magnetic field is related to the resistivity via [42]

$$\frac{\partial B}{\partial t} = \eta\left(\nabla \times j_f\right) + \nabla\eta \times j_f . \tag{48}$$

The magnetic field grows in regions with spatial variations in either current or resistivity. The first term gives rise to a B-field which pushes electrons into regions of higher density. In a cylindrically symmetric beam, this generates a radial force which serves to pinch the beam about its axis. Collimation can occur if the B-field deflects the fast electrons through an angle θ over the distance r_o / θ in which the beam radius doubles [42]. For small angles, a condition for collimation can be written $\frac{r_o}{r_g} > \theta^2$ where r_g is the

electron gyroradius. Collimation occurs for divergence half-angles less than 15° and B-fields greater than 10T which are attainable for this experiment.

The second term in equation 46 arises due to resistive gradients in the material. The B-field direction depends on the shape of the material resistivity. If the temperature on axis is higher leading to a lower resistivity than the bulk material, then the electrons will be pushed out of the beam increasing the divergence. This effect has been observed in insulators due to the large difference in material resistivity [77]. For a metal, if we assume a hot temperature of ~1keV on axis and room temperature for the bulk material, the difference in resistivity values (figure 14) is approximately a factor of 2 different. However, if the bulk material is preheated to ~10eV and then compared with a 1keV temperature on axis, then the 2nd term increases in size serving to push electrons away from the axis.

Resistive filamentation instabilities can occur when the return current is collisional [78]. This a transverse instability driven by magnetic field fluctuations from counter propagating electron currents. This is similar to the Weibel instability with the main difference being collisions drive the resistive instability and the Weibel instability is collisionless. Increases in the resistivity due to collisions lead to an increasing magnetic field which then drives the instability resulting in the electron current filamenting. The growth rate peaks for reduced beam temperatures and larger wavenumbers. This is analogous to the Weibel instability in that the thermal pressure of the electron beam can balance the pinching force exerted by the magnetic field suppressing the instability.

Experiments have been conducted where filamentation has been experimentally observed in insulators, but absent in conductors [79]. The generating mechanism is considered to be a spatial variation in the ionization front or leading edge of the electron beam [80]. The ionizing front velocity increases or decreases due to local increases or

decreases in the electron beam density. A localized increase in the electron beam density accelerates the ionization front with respect to the rest of the beam. This further increases the local beam density leading to filamentation. A qualitative picture of the mechanism is shown in figure 18.

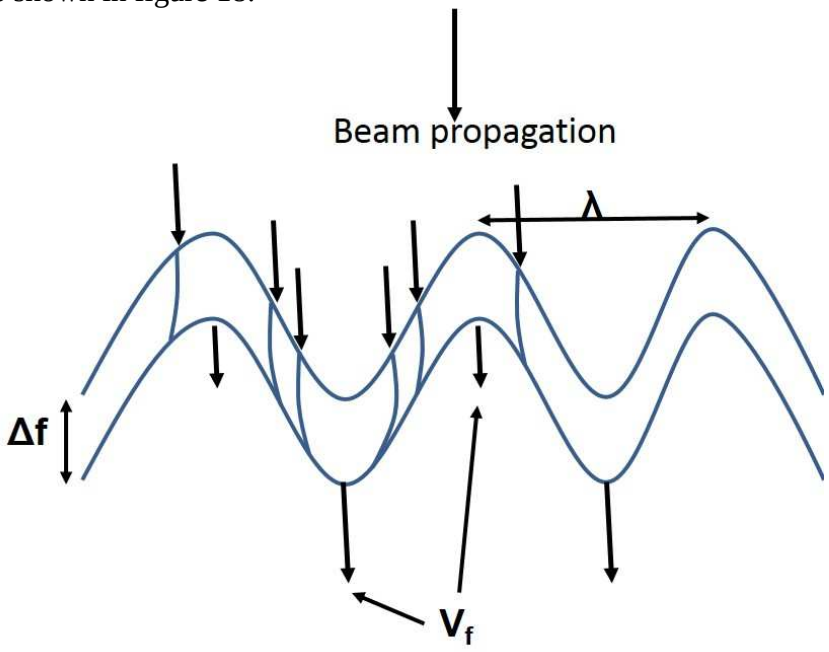

Figure 18: Qualitative picture of the instability of the ionization front in an insulator. V_f is the velocity of the ionization front.

The electric field of the ionization front has been estimated to be approximately 10% of the atomic electric field and the width of the ionization front can be estimated from Poisson's equation [80] $E_a = \frac{4\pi n_b \Delta f}{\varepsilon_o}$ where E_a is the atomic electric field, n_b is the beam density, and Δf is the width of the front. Assuming 10% of the hot electrons participate in the ionization process, a width of ~.1μm is calculated from Poisson's equation. This means that the maximum growth rate would correspond to perturbations

on the order of the front thickness $\lambda \approx 2\pi f$. This wavelength compares favorably to the images shown in figure 17.

In summary, filaments were observed in heated and unheated aluminum less than 10% of the time and were observed in a heated/unheated insulator almost four times greater rate than metal. The target thickness of ~1 μm allows to exclude several filamentation process due to the growth rate of such processes being on the order of several microns. Additionally, the Weibel instability was excluded due to the high plasma density associated with the overdense target and the transverse thermal electron pressure opposing the magnetic pinching force.

The occurrence frequency of filaments in aluminum was similar whether the material was heated or not. This suggests that changes in the resistivity on the order of several orders of magnitude do not influence the generation of filaments. In the insulator, filaments are observed with greater frequency when the material was heated. An insulator that is heated should have a lower resistivity than at room temperature. Based on these observations, neither the resistive filamentation instability nor the magnetic field are the leading cause of filamentation. Spatial variations in the ionization front propagating through an insulator have been found to generate filaments. The filaments observed here fit with the analysis performed in the preceding paragraph describing the ionization front instability. The number of filaments observed is two and in a few shots three. This low number seems to exclude filament recombination or like processes instead suggesting a single perturbation causing the beam to split. This would explain the increase in frequency of observed filaments in the insulator as compared to metal. In the insulator, a greater occurrence of filaments was observed when the target was heated. A possible explanation is the heating beam generates a small perturbation in the electron density that in turn is magnified by the main beam. A similar explanation can be

extended to aluminum. The low frequency of filaments observed in aluminum, ~7% suggests the interplay of multiple experimental parameters: material defects, irregular laser performance, etc as opposed to a single effect that contributes to variations in the electron density. A more rigorous analysis of the filamentation is beyond the scope of this paper and would require additional experimental data. It is worth repeating that the spatial resolution is limited to 2μm and improving the resolution would yield valuable insight into the potential existence of smaller filaments.

4.6 ELECTRON STOPPING POWER

4.6.1 Collisions

The propagation of hot electrons dominated by collisions is given by the Bethe-Bloch [81] formula modified for electrons

$$-\left\langle \frac{dE}{dx} \right\rangle = \frac{K}{2}\rho\frac{Z}{A}\frac{1}{\beta^2}\left[\ln\left(\frac{\tau^2 * (\tau+2)}{2\left(\frac{I}{m_e c^2}\right)^2} \right) + F(\tau) - \delta(\beta\gamma) \right] \tag{49}$$

Here ρ is the material density, $\beta = \frac{v}{c}$, Z is the charge number of the medium, A is the atomic weight, τ is the kinetic energy divided by the electron rest mass, K is the constant terms $\sim 4\pi N_A r_e^2 m_e c^2$, I is the excitation energy of the medium, δ is a density correction term, and F $\sim \beta^2$ is a function where the relativistic terms where combined. Using the ESTAR database at NIST, a 1MeV electron has a range of approximately 2mm. It is reasonable to assume that ~MeV electrons will travel at least on the order of 1mm if only collisions are considered.

4.6.2 Collective

The bulk electrons associated with the return current will generate an electric field in opposition to the fast electron current. The effect of the field can be found by considering a Maxwellian distribution confined by an electric field [82] $E = -\nabla\phi$. Writing the electric field in terms of the electron temperature and plugging into the continuity equation yields

$$\frac{\partial n}{\partial t} = \nabla \bullet \left(\frac{\sigma T_H}{en} \nabla n \right). \tag{50}$$

This is a nonlinear diffusion equation with the solution

$$n = n_o \left(\frac{t}{\tau_{laser}} \right) \left(\frac{z_o}{z + z_o} \right)^2 \tag{51}$$

where $n_o = \frac{2 I_{abs}^2 \tau_{laser}}{9 e T_H^3 \sigma}$ and $z_o = \frac{3 T_H^2 \sigma}{I_{abs}}$. The electron propagation distance z_o can be written as a function of laser intensity, conductivity, and hot electron temperature [82]

$$z_o = \left(\frac{T_H}{200 keV} \right)^2 \left(\frac{\sigma}{10^6 \Omega^{-1} m^{-1}} \right) \left(\frac{I_{abs}}{10^{18} \frac{W}{cm^2}} \right)^{-1} 12 \mu m . \tag{52}$$

Conductivity values in the region of 10eV have been measured [34] to be approximately $1 * 10^6 \Omega^{-1} m^{-1}$. If 40% laser absorption is assumed from a $1.5 * 10^{19} W / cm^2$ laser pulse, electron temp of 1.5MeV, and a conductivity $\sim 1 * 10^6 \Omega^{-1} m^{-1}$, a propagation distance of 120μm is obtained. This distance is notably less than the collisional mean free path. The model has some shortcomings as the Spitzer conductivity is used for a dense plasma, but establishes the fact that electric field inhibition is a greater effect than collisions on electron penetration and dominates target heating on short time scales [19].

Chapter 5: Transition Radiation

A charged particle uniformly moving in a homogeneous medium emits no radiation. An exception is Cherenkov radiation. If the particle is traveling with phase velocity greater than light in that medium, then the particle can emit radiation [83]. However, radiation can be emitted when the uniformly moving particle encounters a sharp interface between two different media called transition radiation [84]. The moving particle has an electric field with certain characteristics in one region and different characteristics in the other. At the interface, the electric fields are dissimilar and a transverse current is generated to satisfy the boundary conditions. The current is then the source term for the emitted radiation in both the forward and backward direction. In order for a sufficient current to be generated, the dielectric properties of the two materials should be sufficiently different. Specifically, in laser-target interactions, the sharp interface typically occurs between a metal target and vacuum although plasma-vacuum interfaces have been observed [85]. Transition radiation was initially derived in the context of a single particle crossing an interface. Recent papers have included theory applicable to transition radiation from electrons accelerated by a laser.

5.1 Single Particle Transition Radiation

Transition radiation is traditionally described by the pseudo-photon method [86]. The pseudo-photon method is a calculation simplification of the perturbation method for electromagnetic processes. The electric field of a particle can be replaced by a similar field of photons when the particle nears relativistic velocities $v \to c$. The longitudinal field of the particle is small enough to be ignored and the particle is assumed to propagate with purely transverse fields like a photon as shown in Figure 19.

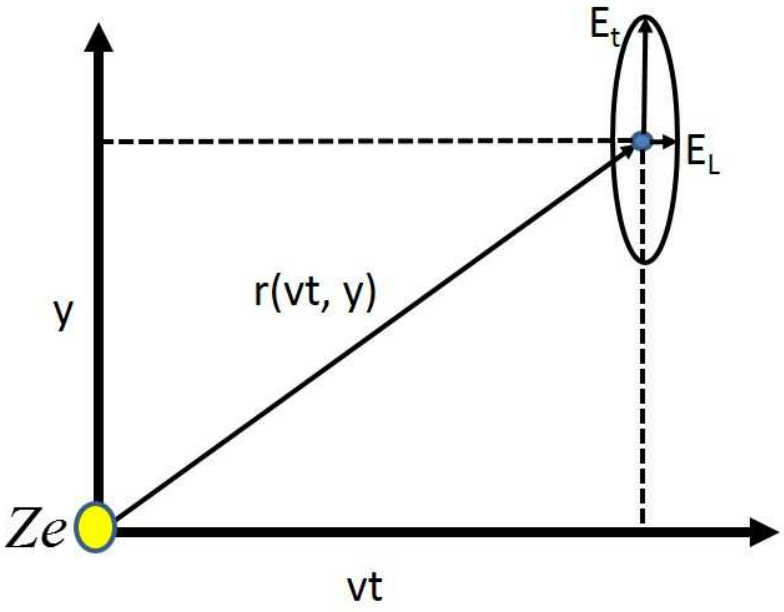

Figure 19: Electric field at point r and time t of a particle, Ze moving with velocity v. At the velocity increases, the transverse field becomes larger than the longitudinal, $E_T >> E_L$.

Following the formalism of [87], we consider the transition radiation of a single particle traveling perpendicular to one interface. Figure 20 illustrates the particle-interface layout.

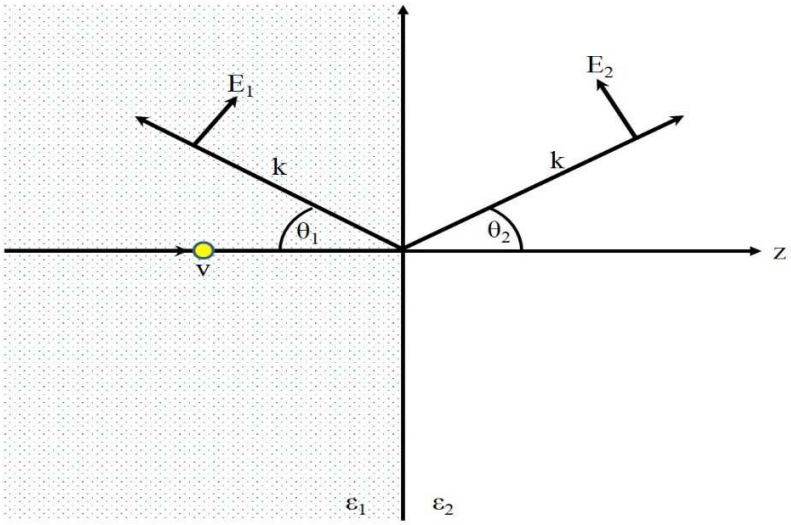

Figure 20: Illustration of transition radiation of a single particle traveling normal to an interface. $\varepsilon_1, \varepsilon_2$ are the dielectric constants of the first and second media and z=0 is the interface.

The particle is traveling in the z-direction with the interface defined to be the plane xy (z=0) and the angles θ_1, θ_2 determine the angles of radiation into the forward and backward directions. The Maxwell equations for the potentials are of the form:

$$\begin{aligned} \Delta A - \frac{\varepsilon_1}{c^2}\frac{\partial^2 A}{\partial t^2} &= -\frac{4\pi}{c} ev\delta(r - vt) \\ \Delta\varphi - \frac{\varepsilon_1}{c^2}\frac{\partial^2 \varphi}{\partial t^2} &= -\frac{4\pi}{\varepsilon_1} e\delta(r - vt) \end{aligned} \tag{53}$$

where the subscript 1 refers to the left of the interface and subscript 2 describes the fields on the right side. The solution for the potentials is found by expanding into Fourier integrals and the electric field will be expressed as

$$E(k,\omega) = \frac{i\omega}{c} A(k,\omega) - ik\varphi(k,\omega). \tag{54}$$

The complete solution for the electric field consists of the charge and the radiation fields $E_1^{Tot} = E_1^{'} + E_1^{rad}$. The radiation fields can be solved for by applying the boundary conditions of the electric field at the interface z=0. The tangential component is written

$E_{1t}^{'} + E_{1t}^{rad} = E_{2t}^{'} + E_{2t}^{rad}$ and the normal component $\varepsilon_1\left(E_{1n}^{'} + E_{1n}^{rad}\right) = \varepsilon_2\left(E_{2n}^{'} + E_{2n}^{rad}\right)$. The additional requirement $\nabla \bullet E_{1,2}^{rad} = 0$ combined with the boundary conditions and electric field solutions for heterogeneous equations allow a solution for the radiation electric fields. The radiation field in the 2nd medium is

$$E_2^{rad} = \frac{-iek_{z2}q^2}{\pi^2 v\left(\varepsilon_1 k_{z2} + \varepsilon_2 k_{z1}\right)} \frac{\left(\varepsilon_1 - \varepsilon_2\right)\left(1 - \beta^2\varepsilon_2 + \beta\sqrt{\varepsilon_1 - \varepsilon_2 \sin^2\theta_2}\right)}{\left(1 - \beta^2\varepsilon_2 \cos^2\theta_2\right)\left(1 + \beta\sqrt{\varepsilon_1 - \varepsilon_2 \sin^2\theta_2}\right)} \tag{55}$$

where $\beta = \frac{v}{c}$, and the photon radiation angles are $q = \frac{\omega}{c}\sqrt{\varepsilon_1}\sin\theta_1$ and $k_{z1} = \frac{\omega}{c}\sqrt{\varepsilon_1}\cos\theta_1$ to the left on the interface. The angles on the right of the interface are similar, but with the subscript 2. The angular and frequency dependence of the radiation is given by the energy flux through the interface $S_z = \frac{c}{4\pi}\int\left(E \times H\right)_z dxdydt$. Plugging in for the expression for the fields, yields an expression for the angular distribution of the radiation

$$\frac{dI_2}{d\Omega d\omega} = 4\pi^2 c\sqrt{\varepsilon_2}\left|\frac{E_2^{rad}}{2k_{z2}}\right|^2 k^2. \tag{56}$$

This equation is referred to as the Ginzburg-Frank formula in the literature.

5.2 LASER ELECTRON TRANSITION RADIATION

The concept of single particle transition radiation can be extended to the situation where a high intensity laser accelerates large numbers of electrons available to produce transition radiation. Hot electrons have a divergence angle and temperature distribution that must be accounted for. The transition radiation consists of two distinct components, incoherent transition radiation (ITR) which is the sum of the radiation spectra from individual electrons and coherent transition radiation (CTR) which is governed by the interference between the electrons. The collisionless acceleration mechanisms, resonance absorption, J x B heating etc., can generate large number electron bunches at harmonics

of the laser frequency. If the bunch form is maintained through the target, coherent radiation is emitted at specific frequency corresponding to the acceleration process present and at an angle related to the transverse bunch spread [88].

Following the formalism of Zheng [88], the radiation field can be written as a summation $E_2^r = \sum_i^N E_i(w_i, u_i)\exp[i\omega t_i - iq \bullet p_i]$ for the configuration shown in figure 21.

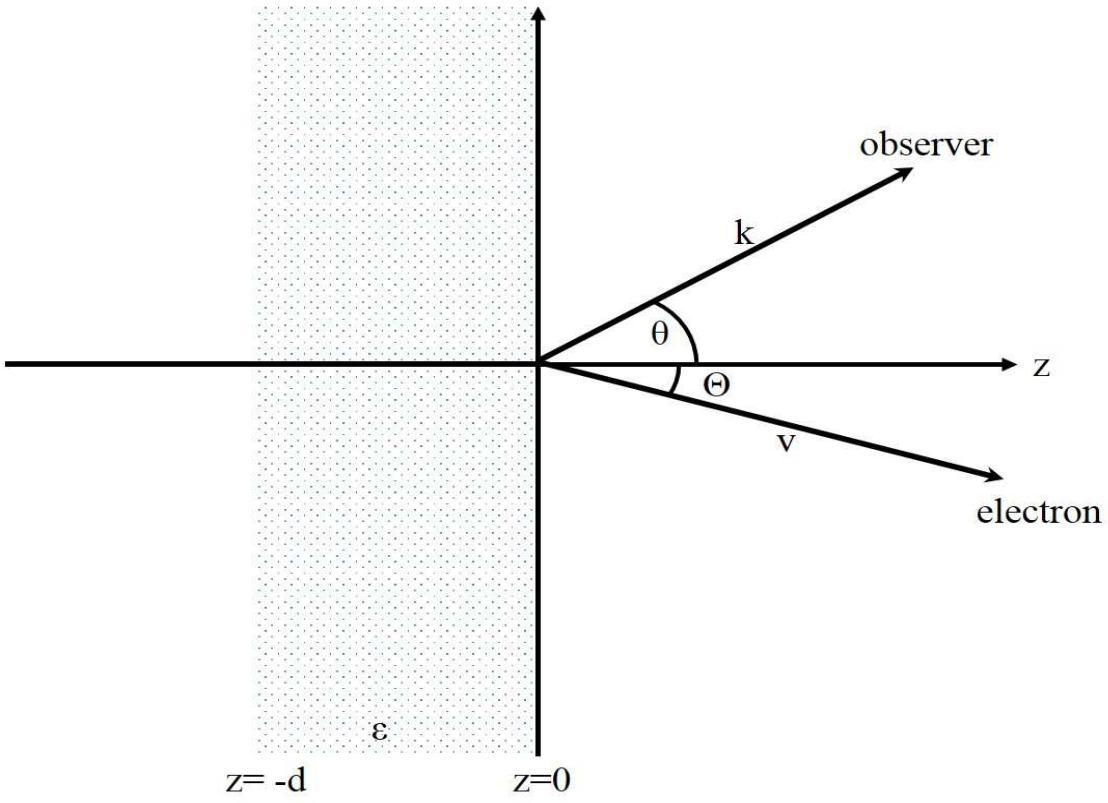

Figure 21: Configuration of the transition radiation calculation. Θ is the electron propagation angle, and θ is the radiation emission angle.

Electrons move from left to right and the interface again is located at z=0. The particle velocity, **v**, coordinate, **r**, and the radiation wave vector **k** are broken down into the tangential and normal components: $v = (w, u) = (v_x, v_y, v_z)$, $r = (\rho, z) = (x, y, z)$, and

$k=(q,\eta)=(k_x,k_y,k_z)$. The particle and radiation emission direction are described by two sets of angles, (Θ,Φ) and (θ,ϕ) respectively. The energy spectrum, the Ginzburg-Frank formulas, is expressed as

$$\frac{d^2E}{d\omega d\Omega}=\frac{c}{4(2\pi)^6\sin^2\theta}\left|\sum_{i=1}^{N}E_i(w_i,u_i)\exp[i\omega t_i-iq\bullet p_i]\right|^2. \quad (57)$$

The spectrum can be separated into two parts: incoherent transition radiation (ITR) given by

$$\frac{d^2E_{ITR}}{d\omega d\Omega}=\frac{c}{4(2\pi)^6\sin^2\theta}\left|\sum_{i=1}^{N}E_i(w_i,u_i)\right|^2 \quad (58)$$

and coherent transition radiation (CTR) given by:

$$\frac{d^2E_{CTR}}{d\omega d\Omega}=\frac{c}{4(2\pi)^6\sin^2\theta}\sum_{\substack{i,j=1\\(i=j)}}^{N}E_i(w_i,u_i)E_j^*(w_j,u_j)\exp\left[i\omega(t_i-t_j)-iq\bullet(p_i-p_j)\right]. \quad (59)$$

5.2.1 Incoherent Transition Radiation

The spectrum of incoherent transition radiation is governed by the radiation spectra, or energy of the individual electrons. A large number of electrons are produced by a high intensity laser and can be described by the appropriate distribution function. We can select a distribution function and plug into equation 59. The summation can be replaced by an integral and the dielectric function can be approximated by $|\varepsilon|\gg 1$ which is the case when the target is a metal. Plugging in the electric fields yields

$$\frac{d^2E_{ITR}}{d\omega d\Omega}=\frac{e^2N}{\pi^2c}\int d\varepsilon d\Theta d\Phi\frac{\beta^2\sin\Theta\cos^2\Theta[\sin\theta-\beta\sin\Theta\cos(\phi-\Phi)]^2f_\varepsilon(\varepsilon,\Theta,\Phi)}{\left[(1-\beta\sin\theta\sin\Theta\cos(\phi-\Phi))^2-\beta^2\cos^2\theta\cos^2\Theta\right]^2}. \quad (60)$$

For the distribution function, a Boltzmann distribution is assumed and written $f_\varepsilon=\frac{3}{2\pi T}\exp[-\varepsilon/T]\cos^2\Theta$, where T is the normalized hot electron temperature, $\beta=\frac{v_i}{c}$ is the normalized particle velocity, $\cos^2\Theta$ is the electron divergence, and

$\varepsilon = \left(1-\beta^2\right)^{-1/2} - 1$ is the normalized electron kinetic energy. In the high temperature limit T>>1, integration over the angles yields

$$\frac{d^2E_{ITR}}{d\omega d\Omega} \sim \frac{3e^2N}{2\pi^2Tc}\int d\varepsilon \exp[-\varepsilon/T]\ln[2(1+\varepsilon)]\cos^2\theta \propto \cos^2\theta\,. \tag{61}$$

In the other limit, we assume $\beta \ll 1$ and can approximate for low velocities

$$\frac{d^2E_{ITR}}{d\omega d\Omega} \sim \frac{3e^2N}{5\pi^2Tc}\int d\varepsilon \exp[-\varepsilon/T]\beta^2\sin^2\theta \propto \sin^2\theta\,. \tag{62}$$

The angular distribution of the ITR varies as a function of the electron temperature. The ITR energy is proportional to the electron distribution temperature.

5.2.2 Coherent Transition Radiation

The spectrum of coherent transition radiation (CTR) is more complex and demands a more rigorous distribution function. The spectrum depends not only on the electron velocity, but on the shape of the electron bunches. The distribution function can be written as a function of two independent parts

$$f_\tau(\tau,\rho,v) = n(\tau,\rho)\, f_v(v)\,. \tag{63}$$

The CTR spectrum can be written as

$$\frac{d^2E_{CTR}}{d\omega d\Omega} = (N-1)\left|\tilde{n}(w,q)\right|^2 \frac{d^2E_{ITR}}{d\omega d\Omega} \tag{64}$$

where $\tilde{n}(\omega,q)$ is the Fourier transformation of the function $n(\tau,\rho)$. The CTR signal will be large in the frequency region where $\tilde{n}(\omega,q)$ is far from zero. We can also separate n into the longitudinal and transverse components $\tilde{n}(\omega,q) = \tilde{n}_l(\omega)\tilde{n}_\perp(q)$. The longitudinal component is given by

$$\tilde{n}_l(\omega) = \frac{1}{1+\Delta\exp\left(-\omega_o^2\tau_o^2/2\right)}\left[\exp\left(\frac{-\omega_o^2\tau_o^2}{2}\right)+\frac{\Delta}{2}\exp\left(-\frac{(\omega-\omega_o)^2\tau_o^2}{2}\right)\right]. \tag{65}$$

The laser pulse duration is τ_o, the electron bunching frequency is ω_o, and Δ is the electron bunching amplitude. It is seen that the longitudinal component will be largest in the regions near $\omega \approx \omega_o$. The transverse component is given by

$$\tilde{n}_{\perp}(q) = \exp\left(\frac{-q^2a^2}{2}\right) = \exp\left(-\frac{\omega^2a^2}{2c^2}\sin^2\theta\right). \tag{66}$$

From this equation, the angular distribution of CTR is mainly contained in an angle described by $\theta \le \frac{\lambda}{2\pi a}$ where a is the beam radius. For most experiments, the laser wavelength is smaller than the beam radius. This conditions yields a small emission angle. The distribution function described above gives insight into the electron bunch, but does not address how the electrons propagate through the target. A more complete distribution function is derived that satisfies the kinetic equation $\frac{\partial f}{\partial t} + v \bullet \frac{\partial f}{\partial r} = 0$. The distribution function is written

$$f_{\tau}(\tau, \rho, v) = \frac{1}{2\pi a^2}\delta(\tau - d/u)\exp\left(-\frac{(\rho - w\tau)^2}{2a^2}\right) f_v(v) \tag{67}$$

where a δ-like electron pulse is assumed to originate at the front surface at t=0. Plugging in the distribution function and consider electrons propagating in one dimension gives

$$\frac{d^2E_{CTR}}{d\omega d\Omega} = \frac{e^2N_b^2}{\pi^2 c}\sin^2\theta\exp[-q^2a^2]\left|\int d\tau d\beta \exp[i\omega\tau]\times\sum_{\alpha=1}^{\Lambda}\delta(\tau - \tau_\alpha - t_o/\beta)\frac{\beta f_v(\beta)}{(1-\beta^2\cos^2\theta)}\right|^2 \tag{68}$$

where N_b is number of electrons in an individual bunch, $t_o = d/c$ where d is the target thickness, Λ is the number of bunches, θ is the incidence angle, and τ_n is the time when the nth bunch is generated. The distribution function is given by $f_v(\beta) = \frac{\beta}{T(1-\beta^2)^{3/2}}\exp[-\varepsilon/T]$. Integrating over β and rewriting yields an expression for the CTR spectrum,

$$\frac{d^2E_{CTR}}{d\omega d\Omega} = \frac{e^2N_b^2}{\pi^2 cT^2 t_o^2}\sin^2\theta \exp[-q^2a^2]\left|\tilde{g}(\omega,\theta,T,d)\right|^2. \tag{69}$$

The function $\tilde{g}(\omega,\theta,T,d)$ is the Fourier transform of the function

$$g(\tau,\theta,T,d) = \sum_{\alpha=1}^{\Lambda} \frac{\left(t_o/(\tau-\tau_\alpha)\right)^4 \exp\left[-\left(1/\sqrt{1-\left(t_o/(\tau-\tau_\alpha)\right)^2}-1\right)/T\right]}{\left[1-\left(t_o/(\tau-\tau_\alpha)\right)^2\cos^2\theta\right]\left[1-\left(t_o/(\tau-\tau_\alpha)\right)^2\right]^{3/2}}. \tag{70}$$

$\left|\tilde{g}(\omega,\theta,T,d)\right|^2$ is the defining term for the CTR spectrum. The energy radiation spectrum is plotted in figure 22 for several different scenarios.

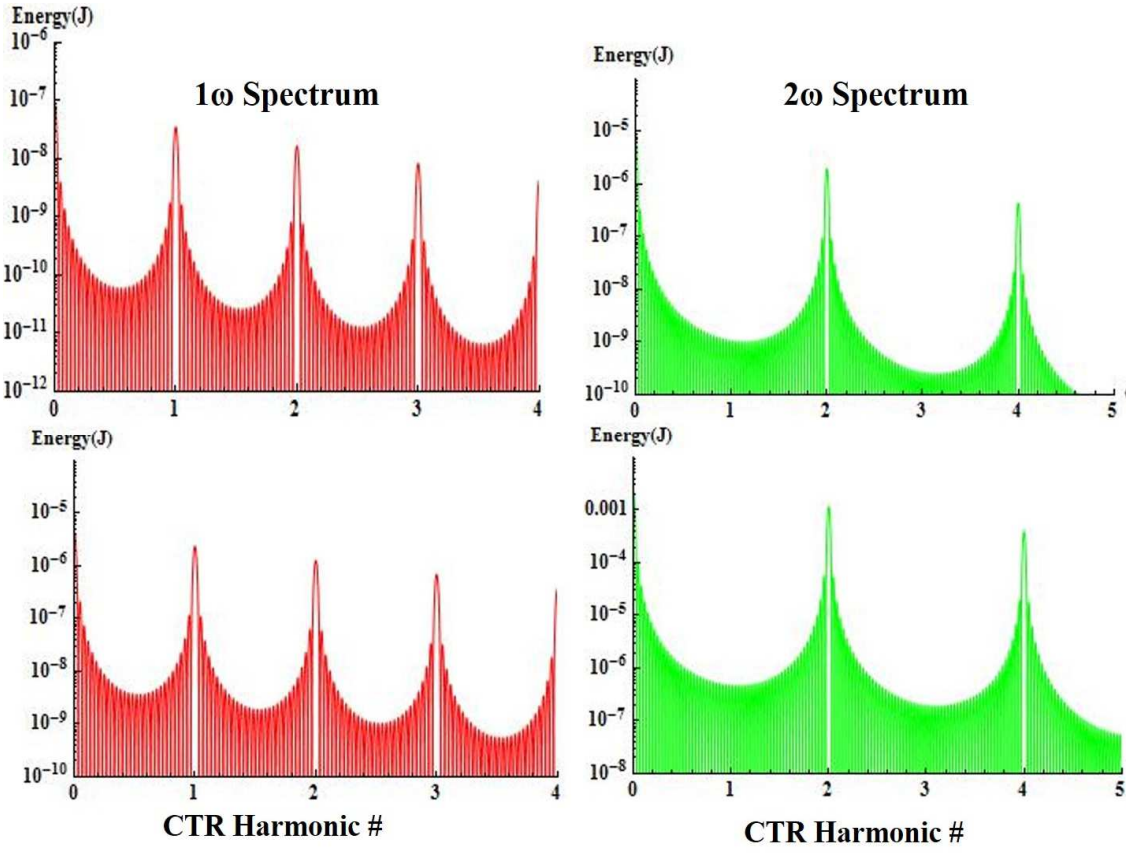

Figure 22: Spectrum of CTR plotted for θ=15deg and t=1.5 micron. The left column consists of electron bunches once a laser cycle and the right hand twice a cycle. Electron temperature of t=750keV are plotted for the top row and 3MeV for the bottom row.

The change of the electron bunch characteristics as it propagates through the target can be seen through the function

$$N(\tau)=\frac{N}{\Lambda T}\sum_{\alpha=1}^{\Lambda}\frac{\left(t_o/(\tau-\tau_\alpha)\right)^3\exp[-\left(1/\sqrt{1-\left(t_o/(\tau-\tau_\alpha)\right)^2}-1\right)/T]}{t_o\left[1-\left(t_o/(\tau-\tau_\alpha)\right)^2\right]^{3/2}}. \qquad (71)$$

This is the number of electrons crossing the rear surface in unit time. The number of electrons for two different target thickness at an electron temperature of 1.5MeV is shown in figure 23.

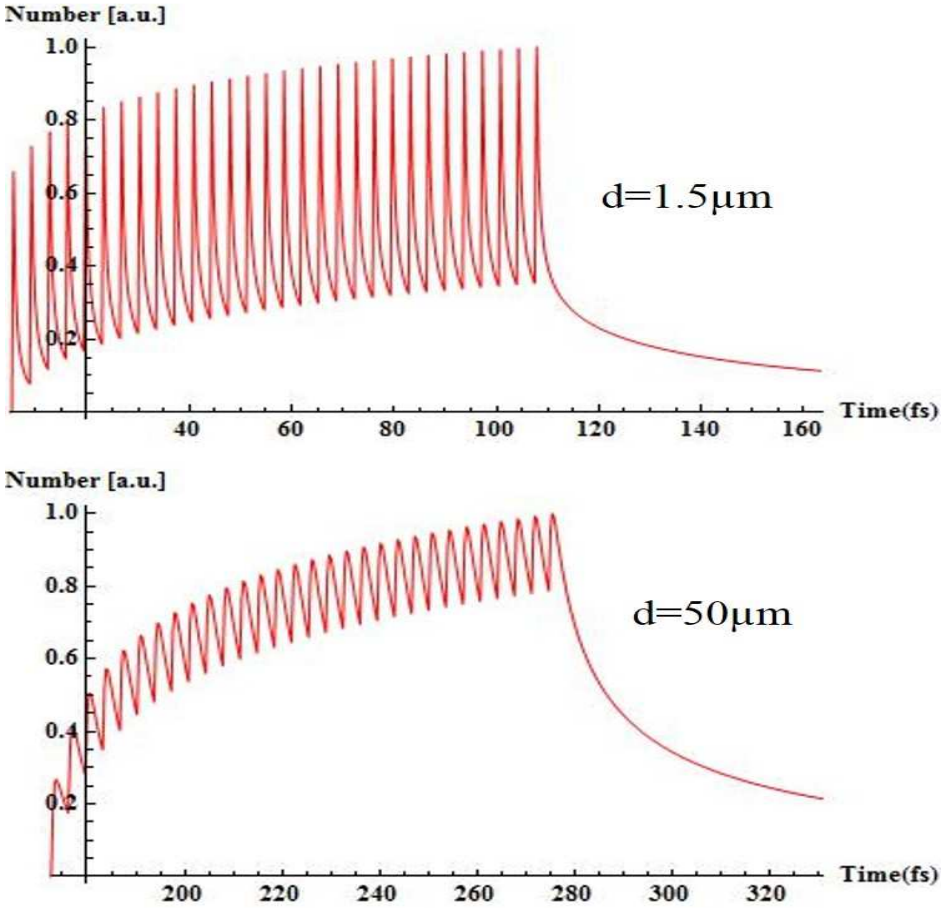

Figure 23: Normalized number of electrons crossing the rear surface in unit time. At top, a 1.5μm thick target and at bottom is a 50μm thick target.

Chapter 6: Experimental layout

This experiment was performed on the GHOST (Glass Hybrid OPCPA Scale Test) laser system. The GHOST laser architecture consists of an OPCPA front end with mixed glass, silicate & phosphate, amplification stages with center wavelength at 1055nm. The baseline operating specifications are 2J compressor input energy, 120fs FWHM pulse duration with on-target intensities of $2*10^{19}$ W/cm^2. The laser layout is presented in figure 24 with the baseline operating parameters for each laser stage. The operating parameters of the GHOST laser will be summarized below. A more detailed description of the GHOST laser can be found here [90, 91]. In addition, the target experimental chamber layout and experimental method is discussed.

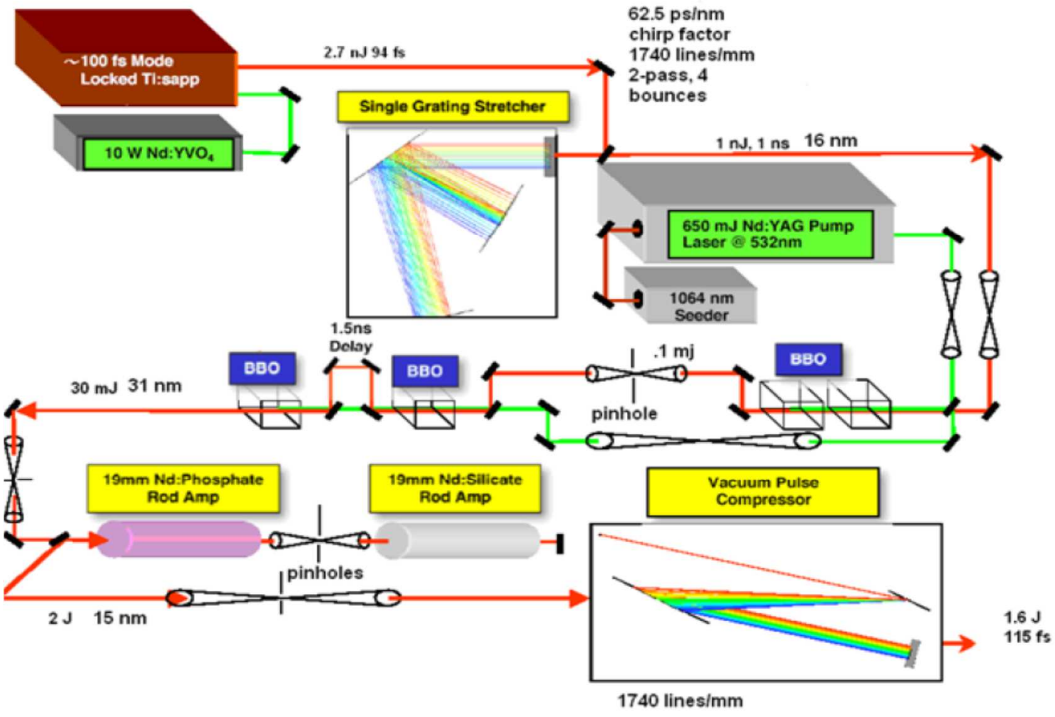

Figure 24: Overview of GHOST laser layout.

6.1 GHOST LASER

6.1.1 Front End

The GHOST oscillator is a Coherent Mira 900 using a Ti:Sapphire crystal pumped by a Verdi V-10 diode laser. The V-10 provides 1064nm light from a Neodymium Vanadate crystal doubled to 532nm by an intercavity type 1 LBO crystal. The output power is 10 watts continuous wave (cw) on the Ti:Sapphire crystal. The Mira 900 oscillator produces modelocked pulses at a frequency of 76MHz with a full width half-max (FWHM) pulse duration of 94fs. The output pulse has 18nm FWHM bandwidth centered at 1055nm. Ultrashort pulse production is due to two basic concepts: modelocking of pulses and the ability to discriminate between a modelocked and a cw pulse.

Laser output consists of longitudinal modes with integral half wavelength equivalent to the laser cavity length. If the modes are all at a fixed phase from each other, the modes are said to be modelocked. The laser typically starts in cw mode. A fluctuation is created by altering the cavity length, in this case tilting the angle of a glass plate. If done fast enough, this allows amplification of a much larger set of modes resulting a higher intensity. When high light intensities are incident on a medium, the index of refraction of the medium changes as a function of intensity $n = n_o + n_2 I$. This is known as the optical Kerr effect [92]. In the Mira 900, the Ti:Sapphire crystal is the Kerr medium. The high intensity pulse is refracted and is smaller than the cw modes. A slit is

installed in the cavity favorably selecting the high intensity pulse as shown in Fig 25.

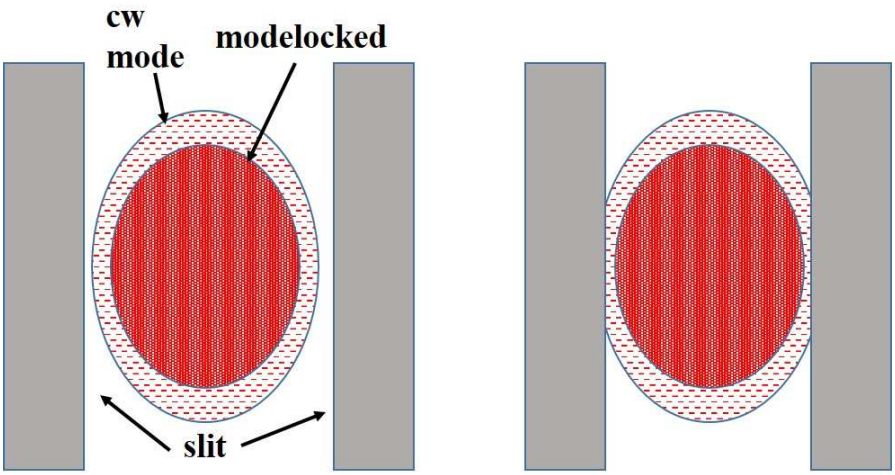

Figure 25: Image at left shows the oscillator slits open allowing both the cw and modelocked beam to lase. At right, the cw mode is blocked biasing gain for the modelocked mode.

Once the modelocking process has been initiated, it does not require additional fluctuations for it to continue. The modelocked oscillator output beam then passes through a Pockel's cell to the stretcher. The Pockel's cell operates at 10Hz with a 300ps rise time allowing the filtering of a single pulse. The stretcher is based on the Martinez design [93]. The beam makes four passes off of a gold 1740 groove/mm stretcher at an angle of $\theta = 74.7$ and is stretched to 1ns. The oscillator (typically referred to as the seed) pulse then enters the 1st OPA stage.

6.1.2 OPCPA

The OPCPA consists of two amplification stages of barium borate (BBO) crystals. Each amplification stage consists of a pair of crystals. The crystals have a 1deg wedge in order to reduce parasitic lasing. The crystal dimensions are 7mm x 7mm x 15mm for the first stage and 10mm x 10mm x 15mm for the second.

The BBO crystals are pumped by a Spectra Physics GCR PRO350. The GCR is a q-switched Nd:YAG operating at 10Hz. The beam is frequency doubled by a KD*P nonlinear crystal to 532nm yielding an output energy of 1J. The beam is separated via polarizer and waveplate into two beams to separately pump the first and second OPA stages. Both beams are down collimated and relay imaged to the face of the BBO crystal by a telescope. The first stage beam has 130mJ of energy with a beam diameter of 2.37mm and the second stage has 550mJ with a beam diameter of 4.7mm. In the first stage, the input seed energy of 1nJ is amplified to 100µJ, a factor of $\sim 10^5$. In the second stage, the beam is amplified from 100µJ to 30mJ. The 2nd BBO crystal is separated by a 2ns delay stage from the 1st crystal to extract the maximum amount of pump energy. The output spectrum saturates and as a results broadens to a FWHM of ~30nm compared to a FWHM of 16nm for the oscillator output as seen in figure 26.

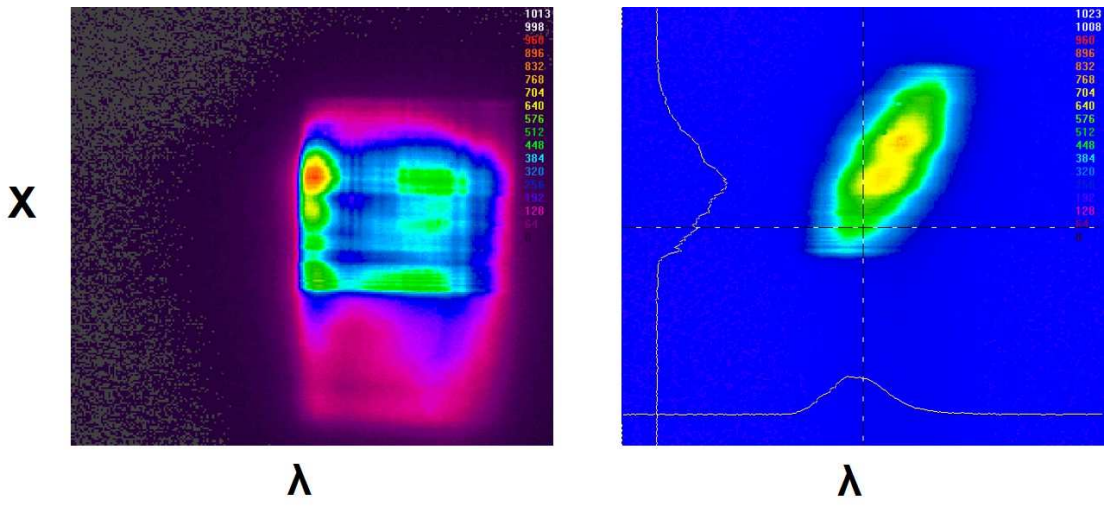

Figure 26: Bulk spectrum images of the GHOST laser. AT left, 2nd stage OPA beam with a FWHM of 30nm. Image at right is the modelocked oscillator only. The spatial chirp is due to the slight off-axis design of the stretcher.

6.1.3 Glass Rods

The beam now double passes through a pair of 19mm diameter glass rods. One rod is Nd:Phosphate glass and the other Nd:Silicate. The rods are flashlamp pumped by an external pulse forming network (PFN). The different glasses amplify the seed pulse in different spectral regions overlapping one another. The gain in each glass is basically the same, but the combined spectrum after amplification permits very shots pulses ~100fs. The appropriate PFN settings for each rod were experimentally determined to obtain the operating specifications of 2J energy output.

The compressor consists of two 35 x 15cm dielectric gratings. The beam is recompressed through four passes of the gratings. The four pass energy efficiency is 78% yielding a baseline output of 1.5J and 120fs pulse duration.

6.1.4 Autocorrelation

The recompressed pulse duration is measured with a 2^{nd} order autocorrelation. The autocorrelation is typically aligned with just the OPA beam. Typical images are shown in figure 27. The image on the top left is a typical autocorrelation of only the OPA beam. The lineout below is the average of the rectangular highlighted region. Assuming a Gaussian profile, the FWHM of the pulse corresponds to 68fs. A spatial to temporal reference was obtained by moving a micrometer stage in the autocorrelation setup. The micrometer delays one pulse in time with respect to the other pulse corresponding to movement of the autocorrelation trace from side to side on the camera. The micrometer is moved a precise distance corresponding to a range of pixel values. This gives a temporal/spatial (fs/pixel) calibration for the viewing region.

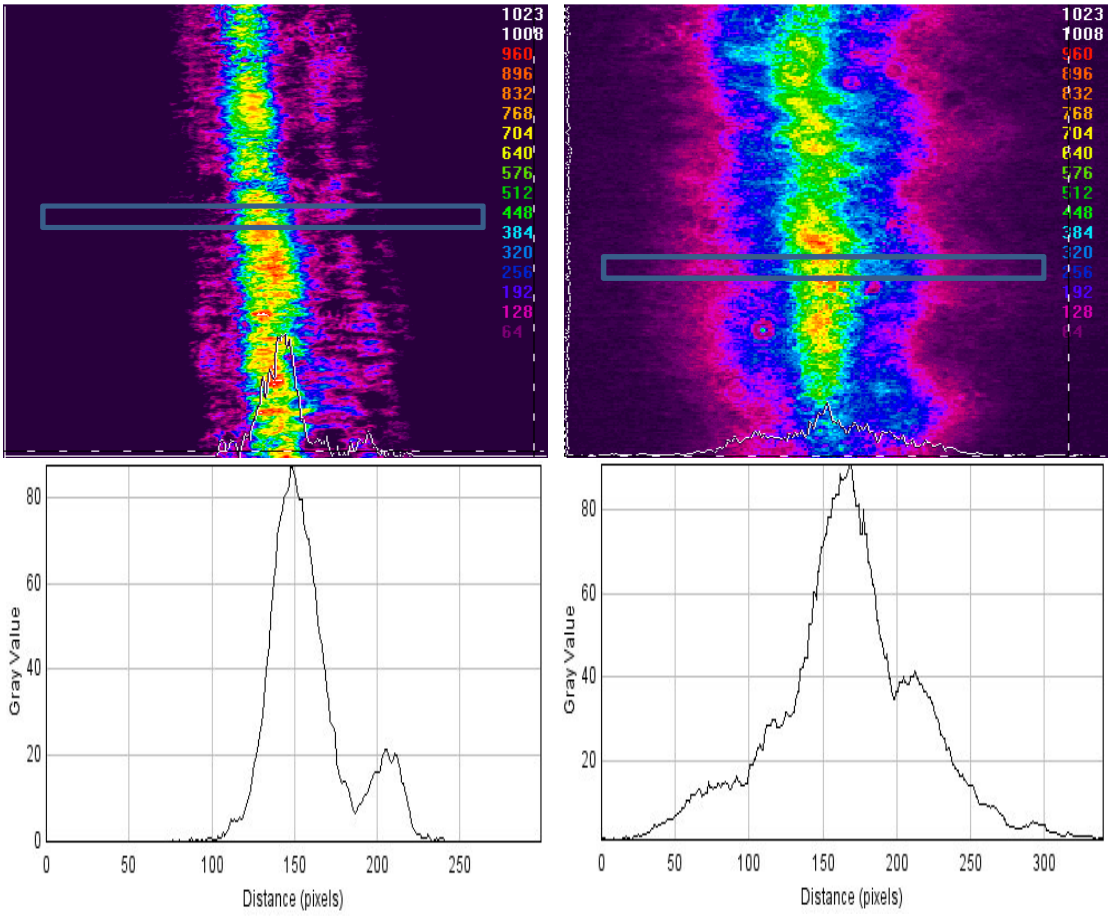

Figure 27: Autocorrelation images of the GHOST laser. The top left is an OPA beam autocorrelation with line out average of the highlighted region of interest at bottom left. The top right is a 2J full energy shot autocorrelation with the line out of highlighted region below.

A 2nd order autocorrelation gives information only about the intensity of the pulse. Information is desired about the temporal profile of the pulse in which case a 3rd order autocorrelation is typically employed. The 3rd autocorrelator was built by Toma Toncian as shown in Figure 28.

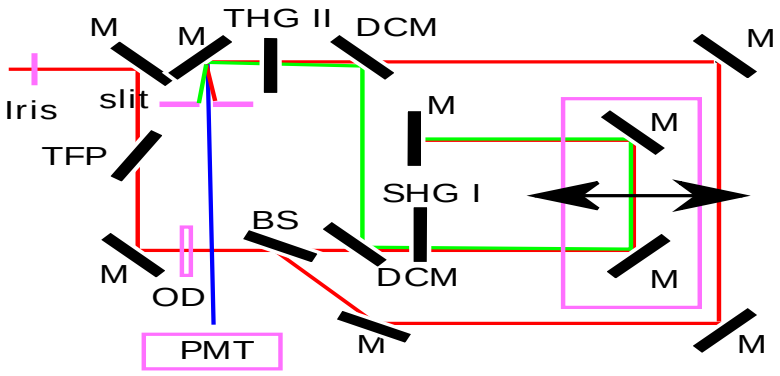

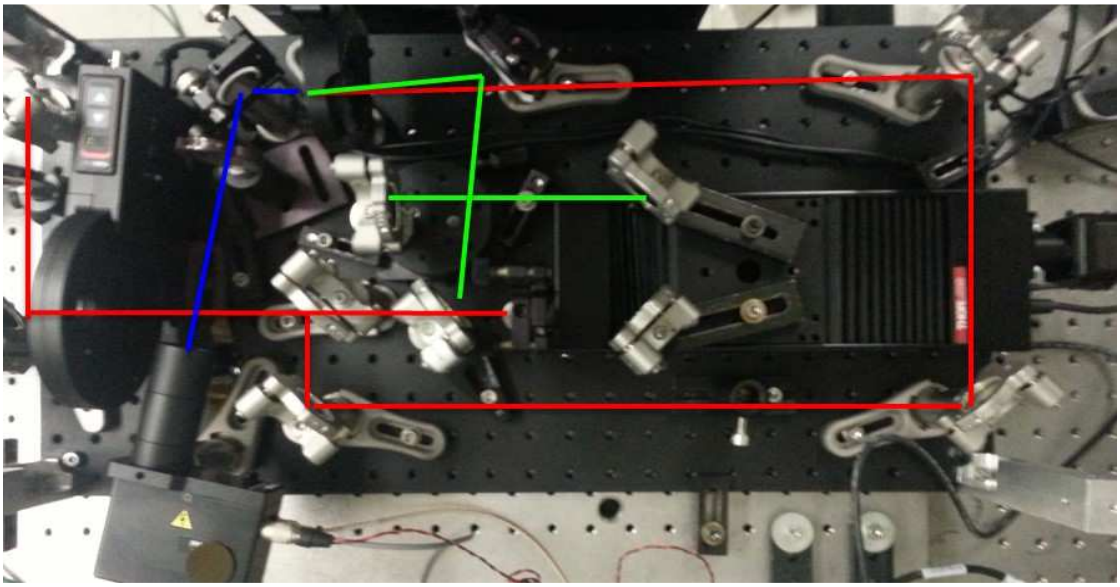

Figure 28: Layout of the 3rd order autocorrelator.

The 3rd order autocorrelator was used to get a detailed look at the temporal pulse profile. The beam is split into two arms – one at the fundamental laser frequency and the other frequency doubled. The two beams are recombined in a KDP crystal yielding 366nm. The 3rd order signal was measured with a ThorLabs PMT. The 3rd order was used to look

at the laser profile due to suspected prepulse. A typical trace from the 3rd order autocorrelator will be discussed in section 7.3.

6.2 EXPERIMENTAL CHAMBER

A new chamber was commissioned to provide a 2nd target chamber for the GHOST laser. The chamber was outfitted with vacuum gauges, motor control feedthroughs and window flanges. Several items were machined better accommodating the footprint of the chamber. The chamber support table was shortened by 1 foot to allow personnel access. The support table was re-leveled with respect to the lab floor. The breadboard had to be machined as every thread was not properly tapped. The tabs supporting the breadboard were not level and had to be redone. Also, a window port was machined in the lid to allow visual access to the target. The chamber with all the experimental equipment is shown in figure 29.

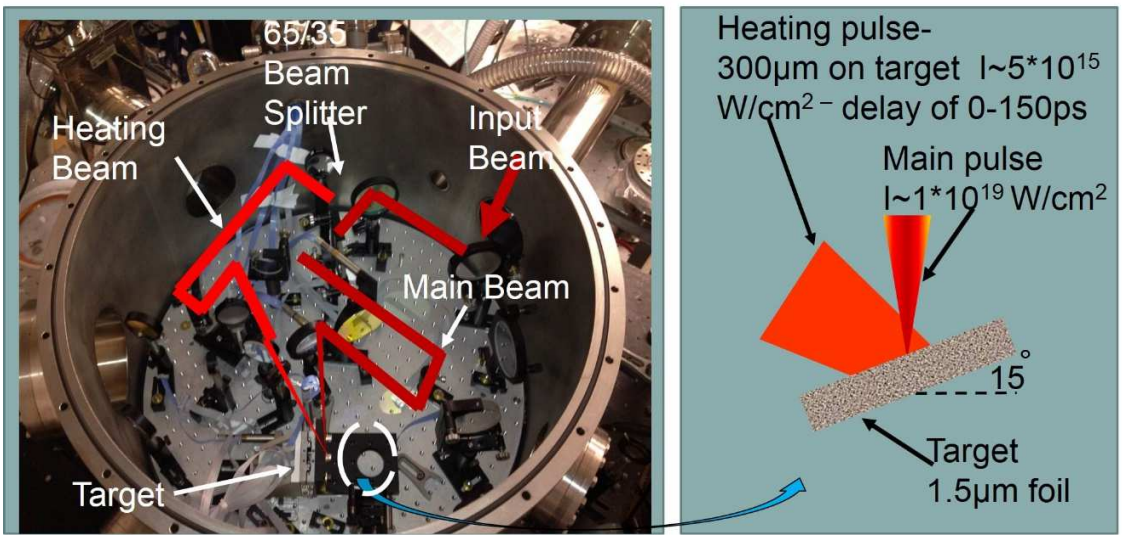

Figure 29: Experimental target chamber layout with beam geometry at target plane.

The beam enters the chamber from the compressor, reflects off a mirror and is split by a 65/35 BK7 beam splitter. The reflected 65% (~800mJ) of the beam is called the main beam while the transmitted 35% (~400mJ) is the heating beam. The main beam is reflected off three additional mirrors and then focused by an off-axis parabola (OAP). The mirror reflections allows the main beam to reach the target plane concurrently with the heating beam. The OAP is protected gold with a 45 degree input angle with an effective focal length of 178.53mm resulting in an f/5.1 focusing optic. The focal spot was characterized using the modelocked oscillator. At best focus, the beam has a FWHM of 6.75µm as shown in Fig 30.

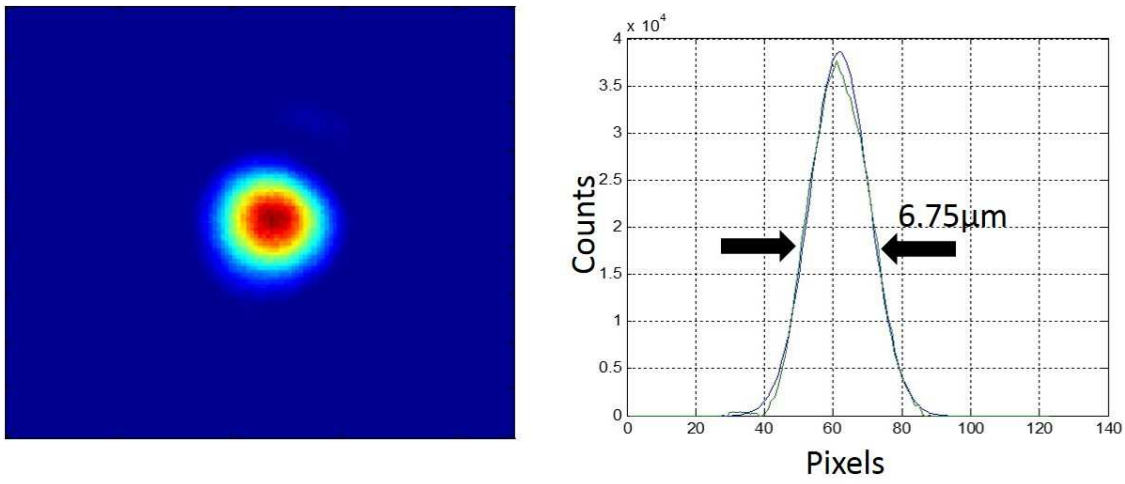

Figure 30: GHOST oscillator focal spot at left. At right, a Gaussian fit of the beam showing a FWHM of 6.75µm.

Gaussian optics defines the diffraction limited beam waist at $1/e^2$ to be [94] $\omega_o = \frac{\lambda}{\pi\theta} = 3.43\mu m$ where θ is .098 with a 35mm diameter beam. So, the beam is close to the diffraction limit.

The main beam was imaged at the target plane by an Olympus PLN 10x infinity corrected microscope objective. The objective has a working distance of 10mm, field number of 22 and numerical aperture of 0.25. The numerical aperture, NA, is defined as [95] $NA = n(\sin\theta)$ where n is the refractive index of the medium and θ is one half of the angular aperture of the objective. Solving for θ yields an angle of 14.48°. The resolution of the objective is then expressed as $R = \frac{\lambda}{2n(\sin\theta)}$ which for 1 micron light is ~2μm, less than a third of the focal spot. The microscope objective images the focal plane directly to a camera. This is slightly unique in that infinity corrected objectives are designed to work in conjunction with a second optical element as an imaging telescope. The location of the camera defines the image plane location of the microscope objective. Since this is outside of the target chamber, the distance to the camera is slightly longer than the standard microscope image distance of 200mm. The microscope objective will now be located at a distance greater than the specified working distance. Since the magnification of an optical element is the ratio of image/object distance, the magnification will be greater than 10x.

A calibrated Air Force target was used to determine the magnification of the viewing area. Similar experiments [96] have observed emission of multiple harmonics. This experiment will use two cameras to separately and simultaneously capture the fundamental and second harmonic. The oscillator light provides the 1055nm light while a 532nm diode is injected through a window port collinear with the oscillator. A dichroic mirror separates the harmonics allowing one camera to view each wavelength. Each camera was equipped with a 10nm bandpass filter centered at the specified wavelength. The filter had an OD4 outside the 10nm window. The AF target was moved into focus on the 1ω camera by moving the target motor. The 2ω camera was moved into focus by

physically moving the position of the camera. An image of the AF target for 1ω and 2ω is shown in figure 31 compared to the laser focal spot.

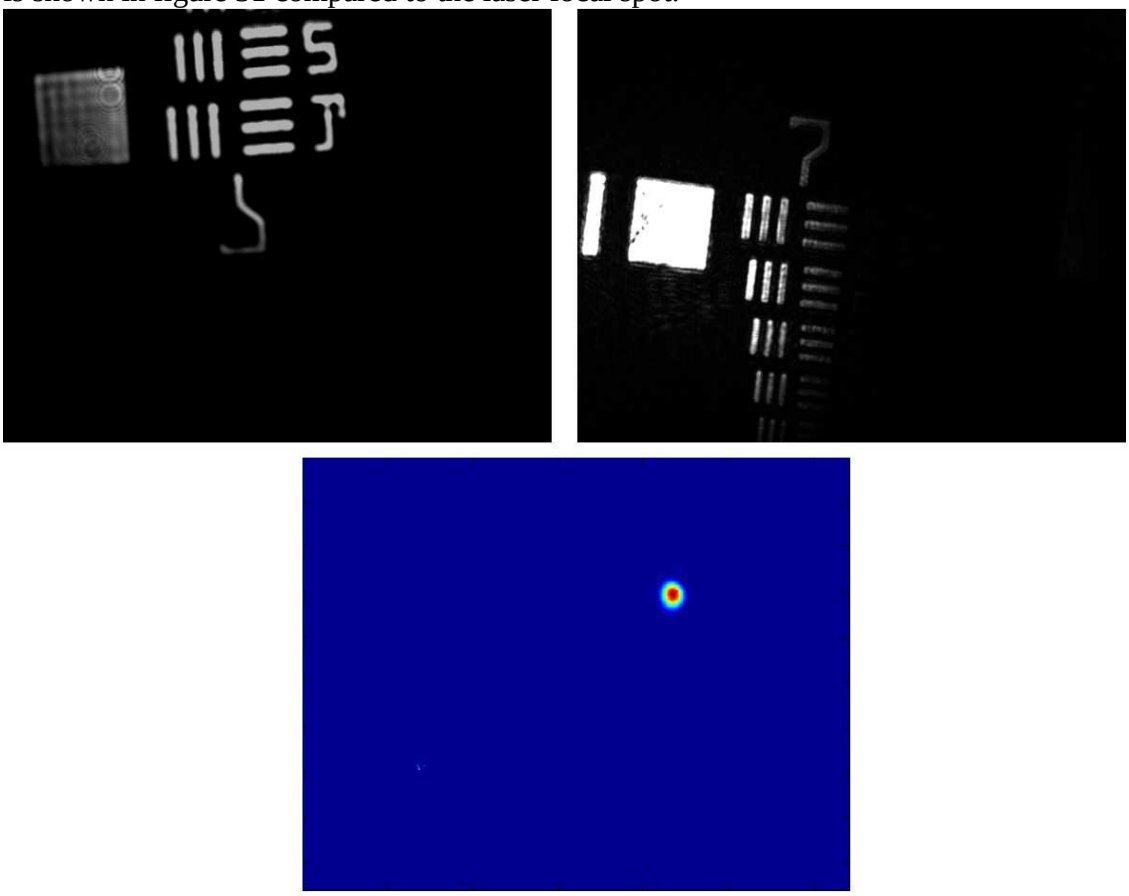

Figure 31: The top left image is AF target from the 1ω camera. The bars next to group 7, element 1 are 3.91µm wide. The top right image is the same air force target imaged with a 532nm diode. Note the cameras are flipped with respect to each other. The laser focal spot is shown below as a reference.

The heating beam consists of the transmitted 35% through the beam splitter. The main components of the heating line consists of a motorized delay stage and a f=250mm plano-convex lens. The heating beam intersects the target plane prior to focus at a diameter of ~300µm. Heating a large area of the target ensures the main beam will efficiently overlap with the part of the target heated by the heating beam.

The heating beam and main beam had to be synchronized temporally to within ~1ps. This was done by comparing the beams with respect to one another. The target chamber was left at atmosphere and only the OPCPA section was used. The focused OPA intensity is $\sim 1*10^{17} W/cm^2$ which is greater than the ionization threshold of air and creates a visible plasma filament. The beams were first aligned only using the oscillator. An iris, corresponding to the target location, was centered on the main beam and the heating beam was aligned through the iris ensuring spatial overlap of the two beams. A single lens was placed in the chamber which imaged the heating beam at the iris to a camera outside the chamber. The OPCPA beam was turned on and the iris was centered on the plasma filament. If required, the heating beam was realigned through the iris. When the main beam arrived earlier than the heating beam, the plasma filament would scatter the heating beam and appear as a dark area as seen in figure 32.

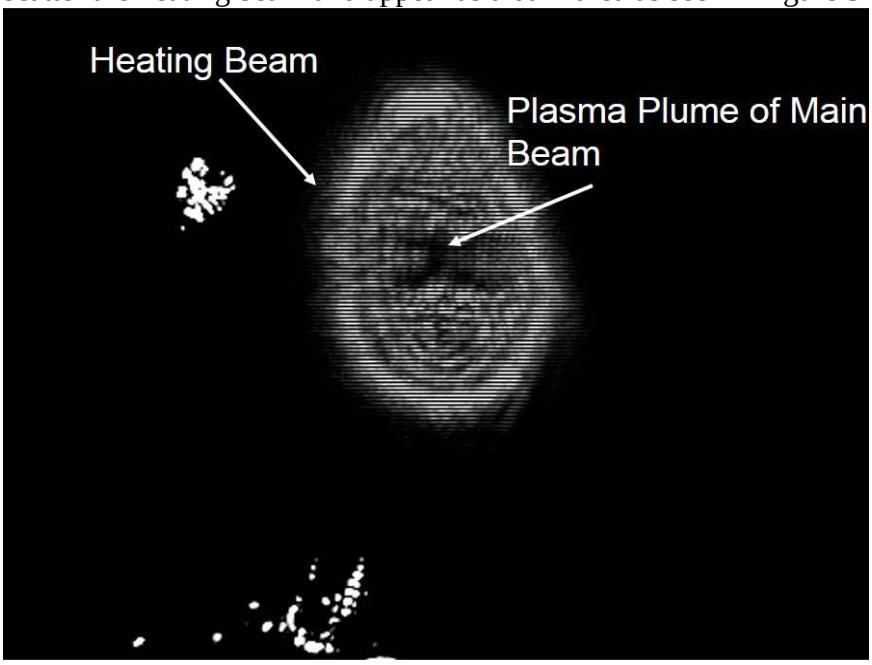

Figure 32: Heating beam imaged at the target plane. The visible dark spot is light scatted from the plasma filament of the main beam ionizing the air. This indicates the main beam crosses the target plane before the heating beam.

As the heating beam was advanced in time by moving the delay stage, the plasma filament would disappear. The indicated that the heating beam is arriving at the image plane before the plasma filament. The delay stage has an encoder that allows precise control of motor positioning. Using the encoder, the beams could be timed up on the order of the pulse duration, ~150fs. It should be noted that this method does not image the experimental target plane. The main beam is intense enough to undergo self-focusing which means beam filamentation occurs earlier than the experimental focus. The heating beam will have to be slightly adjusted which should be minimal (~1ps).

The two beams require spatial synchronization as well. An STM tip was used for this. At focus, the main beam was positioned on the STM tip which completely blocked the beam at focus. The microscope objective was then removed. The heating beam was then visible on an IR card held an inch away from the target. The shadow of the STM tip was quite easily seen on the IR card. A mirror in the heating beam line was adjusted to place the STM tip in the center of the beam.

The target foil was now ready to be positioned in the microscope objective focal plane. Since the target is opaque and not perfectly flat, a z-scatter diagnostic was installed to ensure the target is maintained in the desired z-position. The oscillator beam was apertured by closing an iris upstream of the target chamber. Aperturing the beam changes the f/# of the optical system. The result is a beam with larger diameter and Rayleigh range simulating a collimated light source. An imaged reference point of the target is defined. In this case, the edge of the foil was typically used and shown in figure 33.

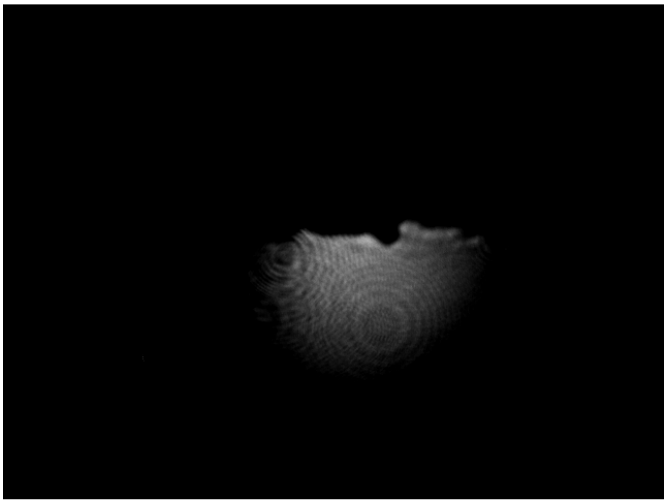

Figure 33: Edge of target foil in image plane. Light scattered from foil is used to define the optimum laser focal plane.

The light reflected off of the target is collected by a lens imaged to a camera outside the chamber. The lens is translated until the reflected light is focused on the camera. Since the target is located at an image plane, the focus of the reflected light on the camera should represent the laser focus corresponding to the target plane. Moving the target in the z direction corresponds to a horizontal displacement on the viewing camera. This is seen in figure 34.

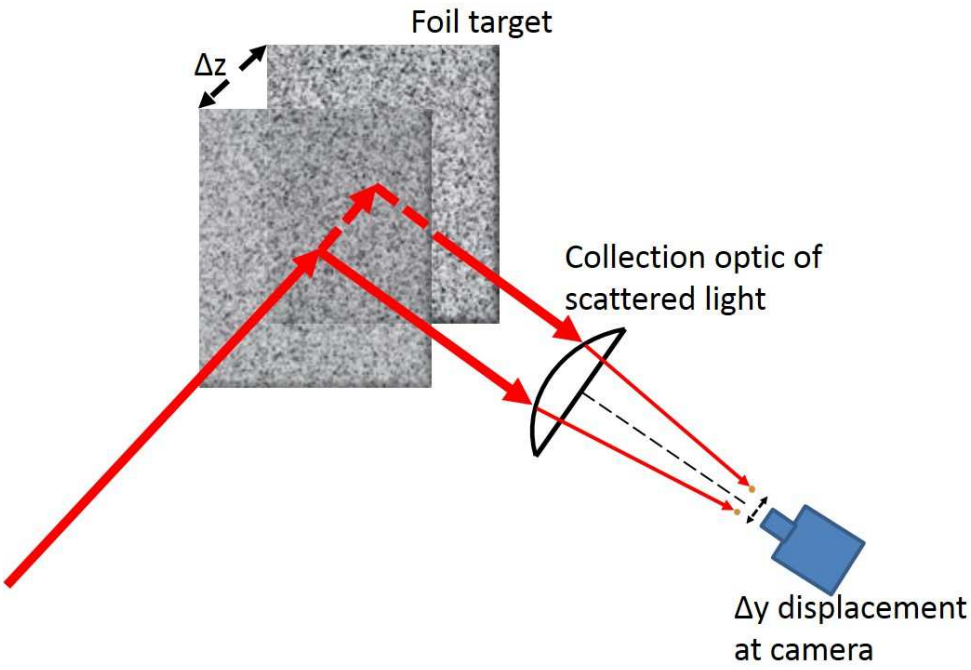

Figure 34: Schematic of the z-scatter positioning system. A z-axis shift in the foil corresponds to a horizontal displacement on the camera screen.

The location of the focus is marked and as the target is moved, the desired z-position can be recovered. This technique allows repeatable target positioning with respect to the same laser z-position.

6.3 TARGETS

Targets used in this experiment were metal foils consisting of different thicknesses and materials. The initial experiment design called for a 90/10 beam splitter used in conjunction with a 200nm thick Al target. 200nm Al foils are not readily commercially available, but can be manufactured using standard equipment in a clean room facility. Photoresist was spin coated on top of a standard microscope slide. The photoresist provided a bonding surface for the aluminum vapor deposited in the

subsequent step. The deposition of the 200nm aluminum layer occurred in the Physics Cryo shop. A cross section view is shown in figure 35.

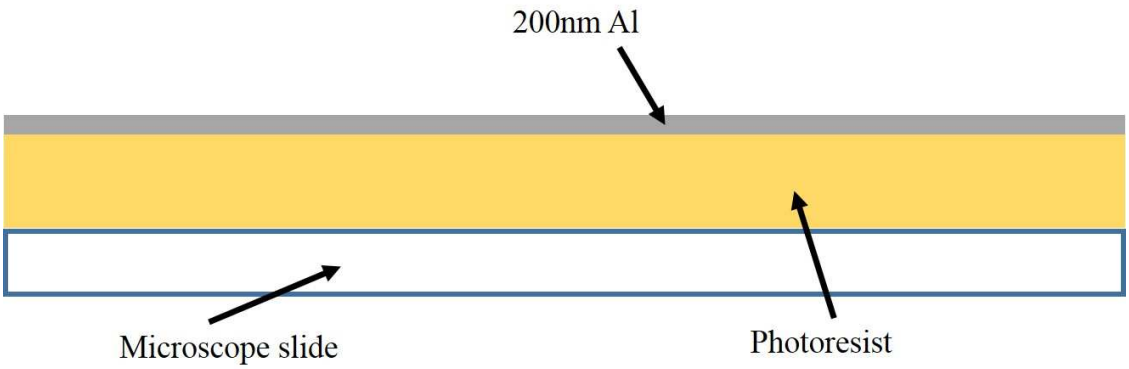

Figure 35: Cross section view of 200nm Al foil slide mounted. The photoresist is spin coated on a microscope slide with Al vapor deposited on top of the photoresist.

The targets were then placed in acetone for approximately 20 minutes to etch away the photoresist. The edges of the target sample were cut with a sharp blade edge to allow the acetone to interact with the photoresist. Once the photoresist was completely etched away, the slide was removed from the acetone and placed into a tub of water. If the target is inserted at a small angle to the water, the Al foil is pulled off the microscope slide relatively intact by the water surface tension. The thin foil floats on the water surface. A target holder is placed underneath the foil. The holder is carefully lifted up until contacting the floating Al foil. The foil then adheres to the holder upon careful removal from the water. The procedure is straightforward, but requires a great deal of dexterity. Additionally, the targets end up quite wrinkled due to the surface tension upon target removal. This creating difficulties in maintaining the z-scatter diagnostic mentioned in section 6.2

The other targets used in tandem with the 65/35 beam splitter were 1.5µm thick. The targets were commercial foils mounted to an aluminum substrate over two machined slits. The foils were attached to the holder with vacuum grease as shown in figure 36.

Figure 36: Typical image of 1.5µm foils mounted on target holders. Foils were mounted on target holder with vacuum grease. The image on right shows the foil with holes from the laser.

One foil was 99% pure aluminum ordered from Alfa Aesar. The other foil consisted of 1.4µm thick polyethylene with "Aluminized" ends from Alexander Vacuum Research. This meant that aluminum was deposited on either side of a polyethylene center. The thickness of the aluminum was not known. Light was readily transmitted through the foil so the thickness was assumed to be 10-20nm. An additional 100nm was deposited on

either side. This ensured the laser would only interact with the aluminum at the front surface.

Chapter 7: Experimental Results

The goal of this experiment is to experimentally quantify the role of return currents in hot electron propagation. The return currents are affected by changing the conductivity of the material. The conductivity was changed in two ways: by heating the material and selecting different material, a conductor and insulator. The primary target selected for this experiment was aluminum due to the availability and large amount of existing theoretical and experimental data. A dielectric target, polyethylene, was selected for comparison with aluminum. Approximately 100nm of Al vapor was deposited on the front and back surface of the polyethylene. This ensured the electron interaction at the front and back surface would be similar, the only difference being the electrons propagation through different material. Additionally, both aluminum and the Al/plastic sandwich target were preheated by a low intensity heating beam.

7.1 HYADES HYDRODYNAMIC SIMULATION

The targets were heated with a 2^{nd} (heating beam) laser beam split from the main laser pulse. The desired effect of the heating beam is to drive a thermal wave propagating the full target thickness. However, a balance must be achieved between initiating a robust thermal wave and minimizing hydrodynamic target effects - front surface expansion, etc. The heating beam-target interaction was modeled with the HYADES hydrodynamic simulation code. The code was written to explicitly model the parameters of the heating beam. The results of the simulation served as the guideline for selecting the appropriate target thickness. The HYADES code is available for our group and runs on a UNIX machine. The user generates an input file which simulates the experimental parameters.

HYADES is a one-dimensional Lagrangean hydrodynamics and energy transport code. The code solves hydrodynamics conservation equations specified on a finite grid and advances them in time to solve problems. The grid is imposed on a region consisting of n zones and $n+1$ mesh points. A region may consist of multiple materials each with associated thermodynamic and hydrodynamic properties referenced in equation of state (EOS) tables. In Lagrangean motion, the mesh moves with the material conserving mass for each zone.

The input to the Hyades code used to simulate the heating beam interaction with both Aluminum and Al/plastic sandwich target is found in Appendix A. The laser is defined to have a Gaussian profile and the Helmholtz wave equation specifies the interaction with the target. The Thomas-Fermi model is the ionization model used. The aluminum is specified as a metal with melting temperature governed by Lindemann's melt model [97]. For the Al/plastic target, polyethylene is the material selected and similar models were used with the appropriate values for polyethylene.

The laser will deposit a majority of its energy in a small spatial scale, the skin depth. To ensure an accurate result, the energy deposited will need to be distributed across multiple zones. Decreasing the zone size is acceptable, however, HYADES only allows a finite number of zones <999 which is not feasible for thick targets. The zone thickness must be adjusted throughout the problem. This must be a smooth adjustment for the conservation equations to hold. The method is to define a dense mesh in the skin depth with a defined size adjustment for adjacent zones. This is called feathering and the following equations describe the relationship between zones [98]:

$$\begin{aligned} (\Delta x)_n &= r(\Delta x)_{n-1} \\ T &= \sum_{n=0}^{NZ} (\Delta x)_n = \left(\frac{1-r^{NZ}}{1-r} \right) (\Delta x)_o \end{aligned} \tag{72}$$

Here r is the feathering ratio, T is the total thickness, NZ is the total number of zones, and $(\Delta x)_o$ is the thickness of the first zone. For increasing thickness, $r > 1$ and less than 1 for decreasing thickness. Feathering ratios are typically around 10%.

The initial plan was to use the GHOST probe line as the heating beam. Energy leakage from the main laser chain is sent into a separate compressor in air and the different beam path allows for variable timing of the probe with respect to the main pulse. However, the air compressor grating had a very low transmission efficiency $\leq 10\%$. The geometry of injecting the probe beam into the target chamber was unrealistic. Instead, a 90/10 fused silica beam splitter was unused from a previous experiment and could be placed directly in the target chamber. This solved the issue of how to route the heating beam into the chamber. Assuming 10% of the laser energy was available for the heating beam and a ~400μm beam diameter, resulted in an on-target intensity of approximately $5 * 10^{13} W / cm^2$. The HYADES simulations for the electron temperature and ion density of an Al foil at this intensity are shown in figures 37 and 38. In all simulations, the laser beam moves from left to right and is incident on the target front surface at 0. The simulations show that the thermal wave could fully propagate a 200nm thick aluminum foil in ~20ps.

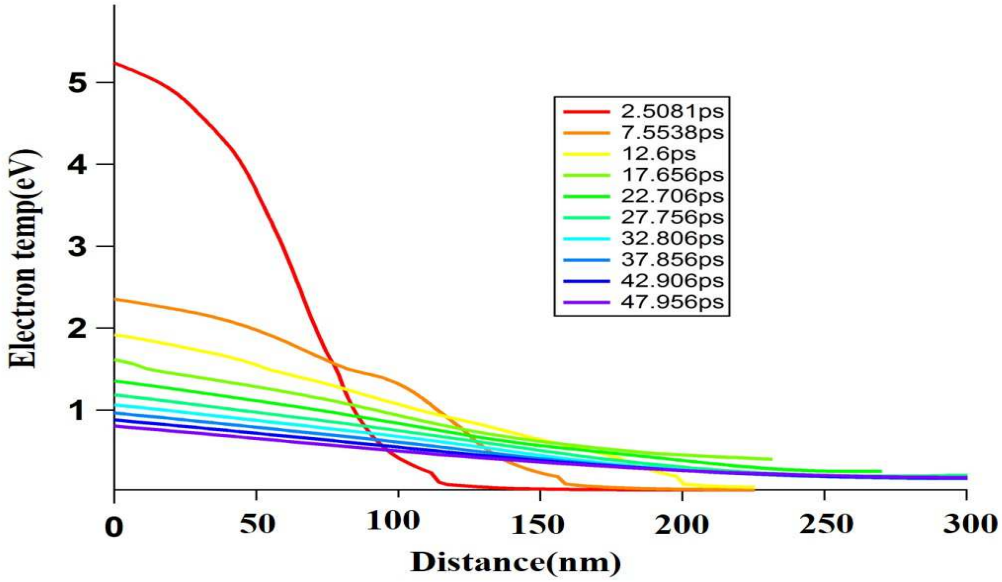

Figure 37: HYADES model of temporal evolution of electron temperature in 200nm Al foil corresponding to a laser intensity of $5*10^{13} W/cm^2$

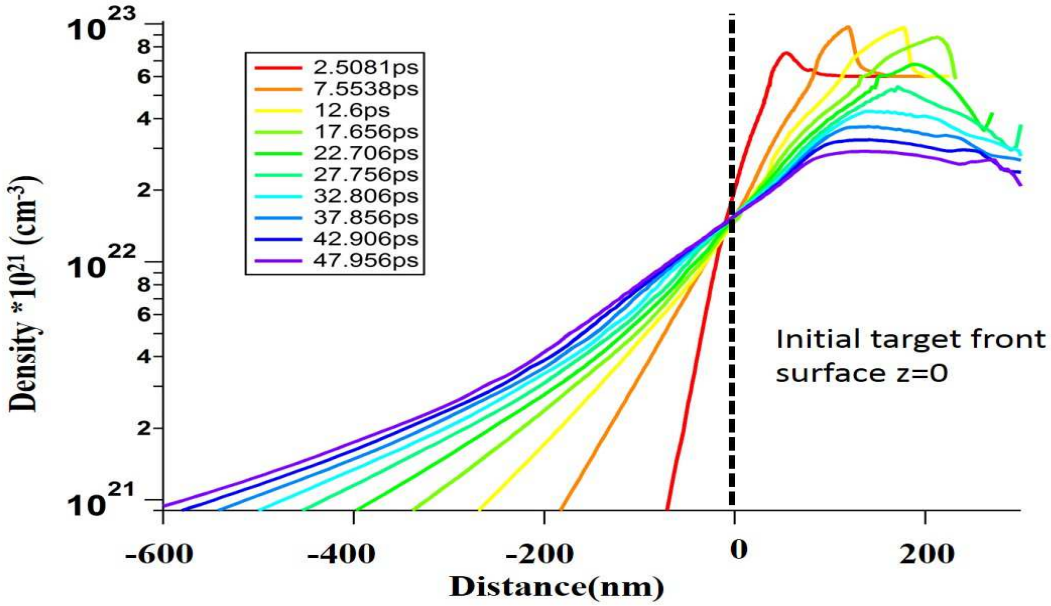

Figure 38: HYADES model of temporal evolution of ion density in 200nm Al foil corresponding to a laser intensity of $5*10^{13} W/cm^2$

In later experiments, a thicker foil was desired and an aluminum foil 1.5µm thick was selected as a target. In order for the heating beam to propagate the full target thickness in a reasonable time frame ~50ps, a new beam splitter was used. A 65/35 beam splitter replaced the 90/10. The heating beam intensity was kept around $\sim 10^{15} W/cm^2$ by reducing the diameter to $\sim 250\mu m$. The HYADES model of the electron temperature corresponding to a heating beam intensity of $5*10^{15} W/cm^2$ is shown in figure 39.

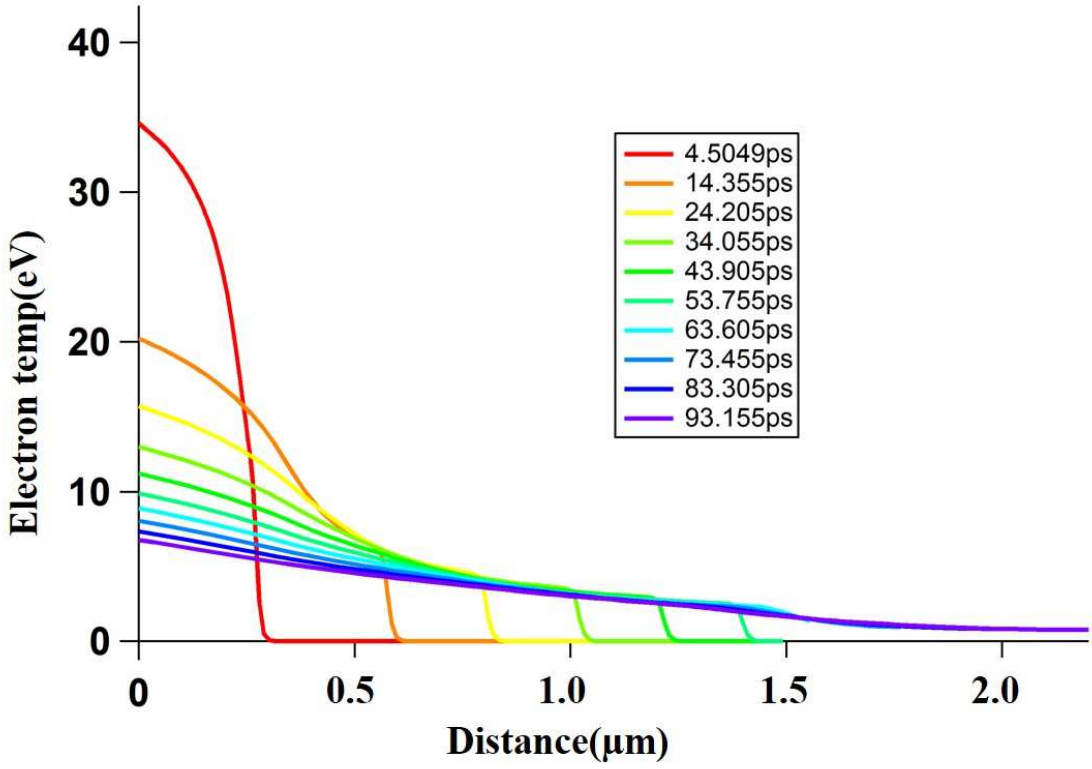

Figure 39: HYADES model of electron temperature in 1.5µm Al target corresponding to a laser intensity of $5*10^{15} W/cm^2$

At 60ps, the thermal wave has reached the back surface of the Al foil. We set that as the maximum heating beam delay required. To measure the return current inhibition related to propagation distance in heated material, we select equal time intervals from 0 to 60ps. The electron temperature distribution for delays of 20, 40 & 60ps are shown in figure 40.

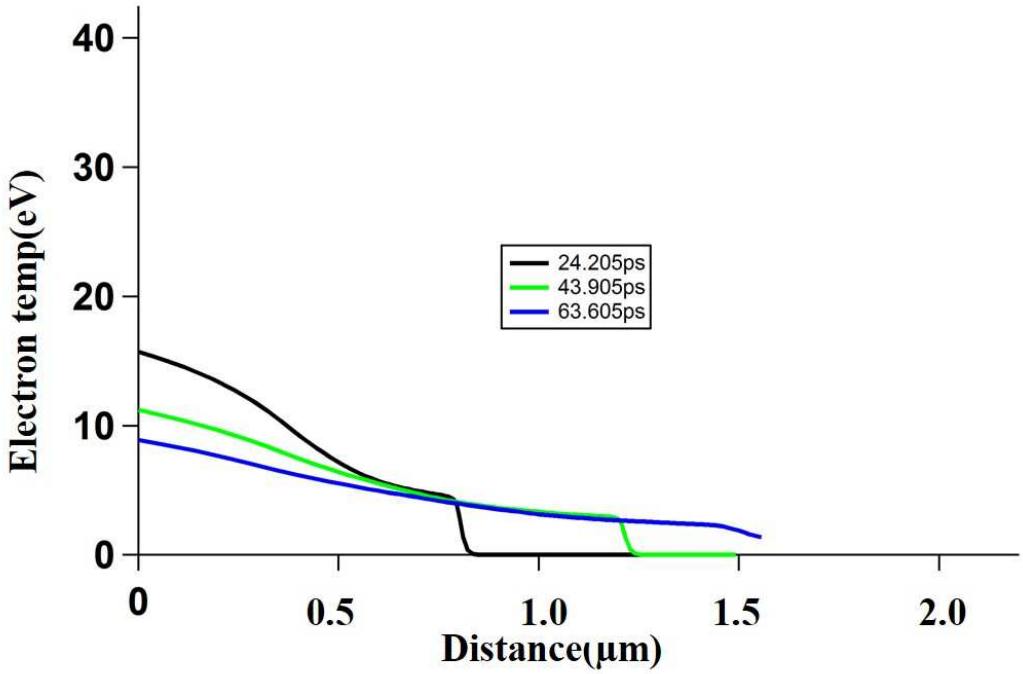

Figure 40: HYADES model of electron temperature at 20, 40, and 60ps time steps in 1.5μm Al target corresponding to a laser intensity of $5*10^{15} W/cm^2$

After 20ps, the heating wave has propagated almost halfway through the target. At maximum delay, 60ps, the entire target has been heated to just under 10eV. The ion density is also modeled in figure 41. The heating beam stiffens the density profile up to 2x room temperature density. The $1/e^2$ preplasma scale length is approximately 1.5μm.

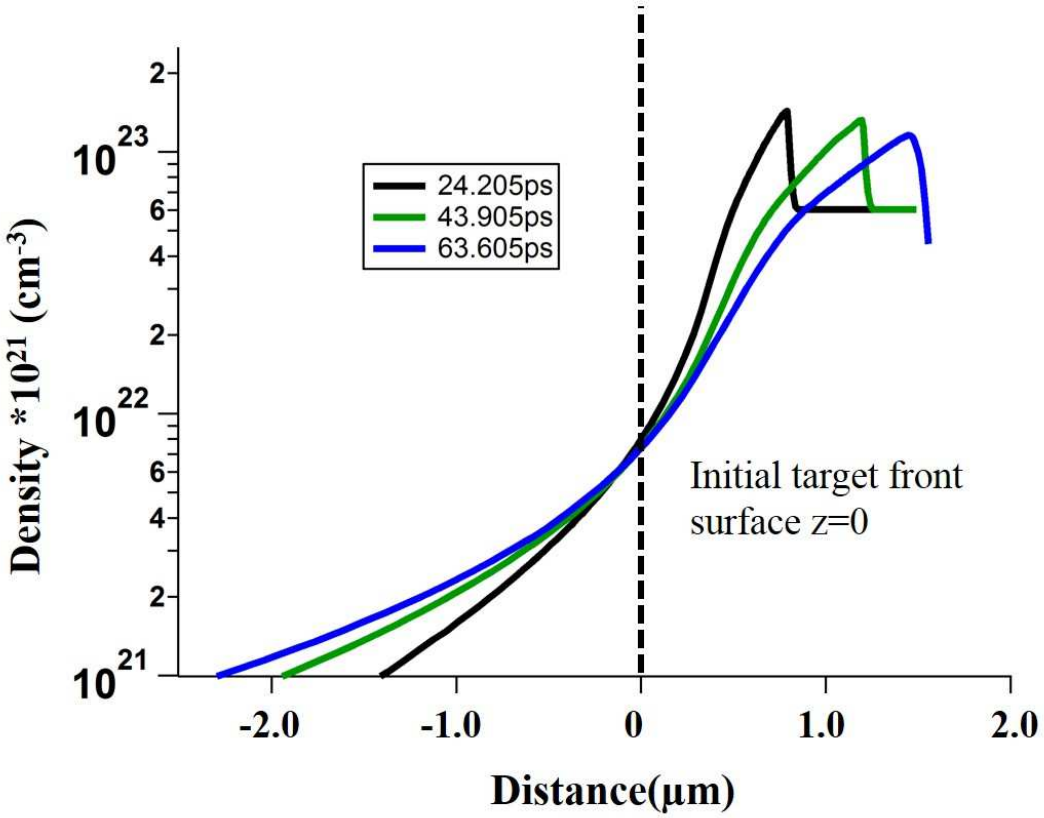

Figure 41: HYADES log plot of ion density at 20, 40, and 60ps time steps in 1.5µm Al target corresponding to a laser intensity of $5*10^{15} W/cm^2$.

7.2 EARLY EXPERIMENTS

The initial experiments were performed on a 200nm Al foil. The goal was to first quantify CTR from the foil first using only the main beam. After a repeatable signal was confirmed, the heating beam would then be unblocked and CTR images taken at the desired time steps between the heating and main beam. The experimental chamber is shown in figure 42.

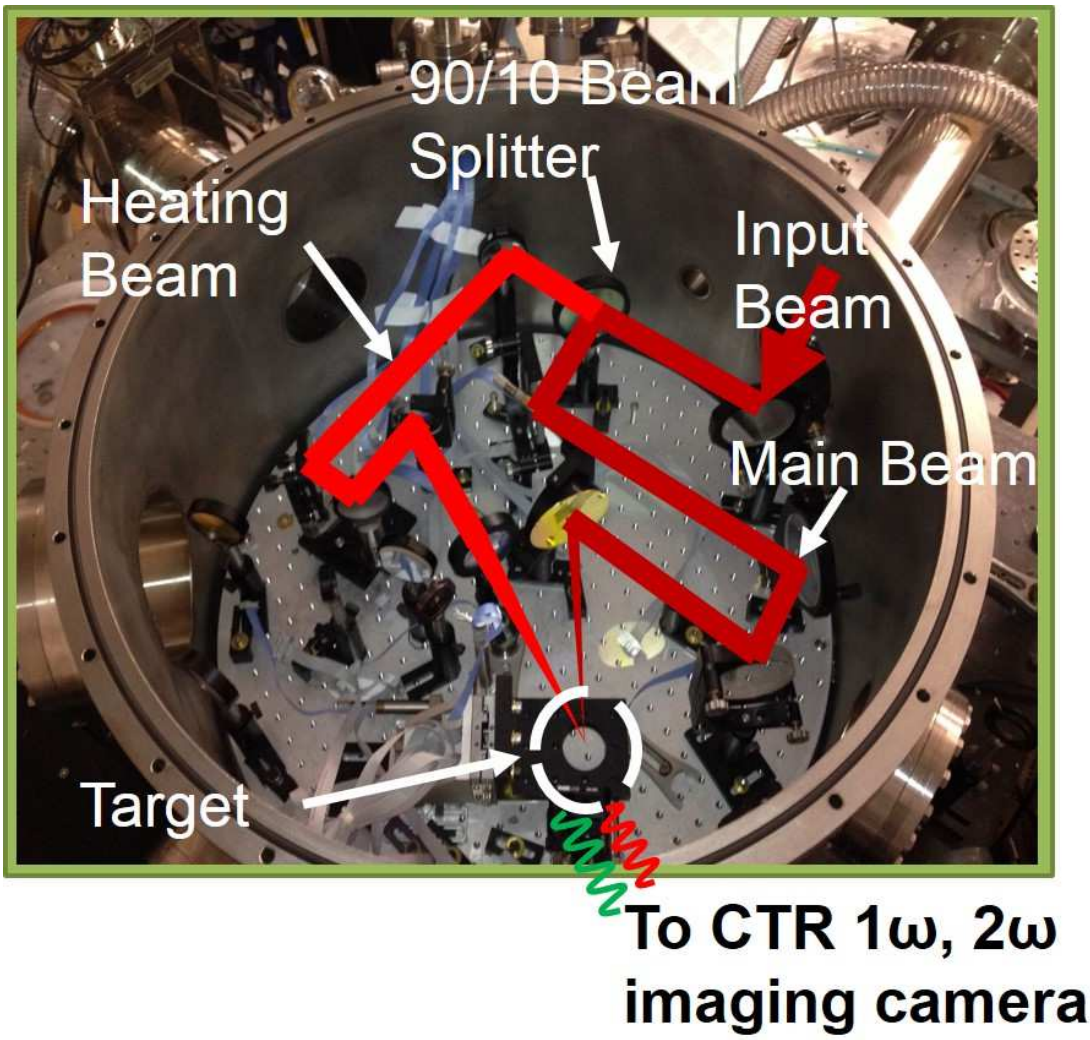

Figure 42: Experimental chamber layout for 200nm Al targets.

7.2.1 200nm Al foil

The experimental methods described in chapter 6 for shooting solid targets were followed. Typical results for both 1ω and 2ω CTR are shown in figure 43. The images on the left are 1ω with ND 7.1 and the images on the right are 2ω with ND 5.2. The viewing window for each image is 40 x 40 microns. The shots were taken from the same

foil. The poor surface quality of the foils made the reflective z-scatter technique very difficult to implement. The assumed best focus was located at the oscillator focus.

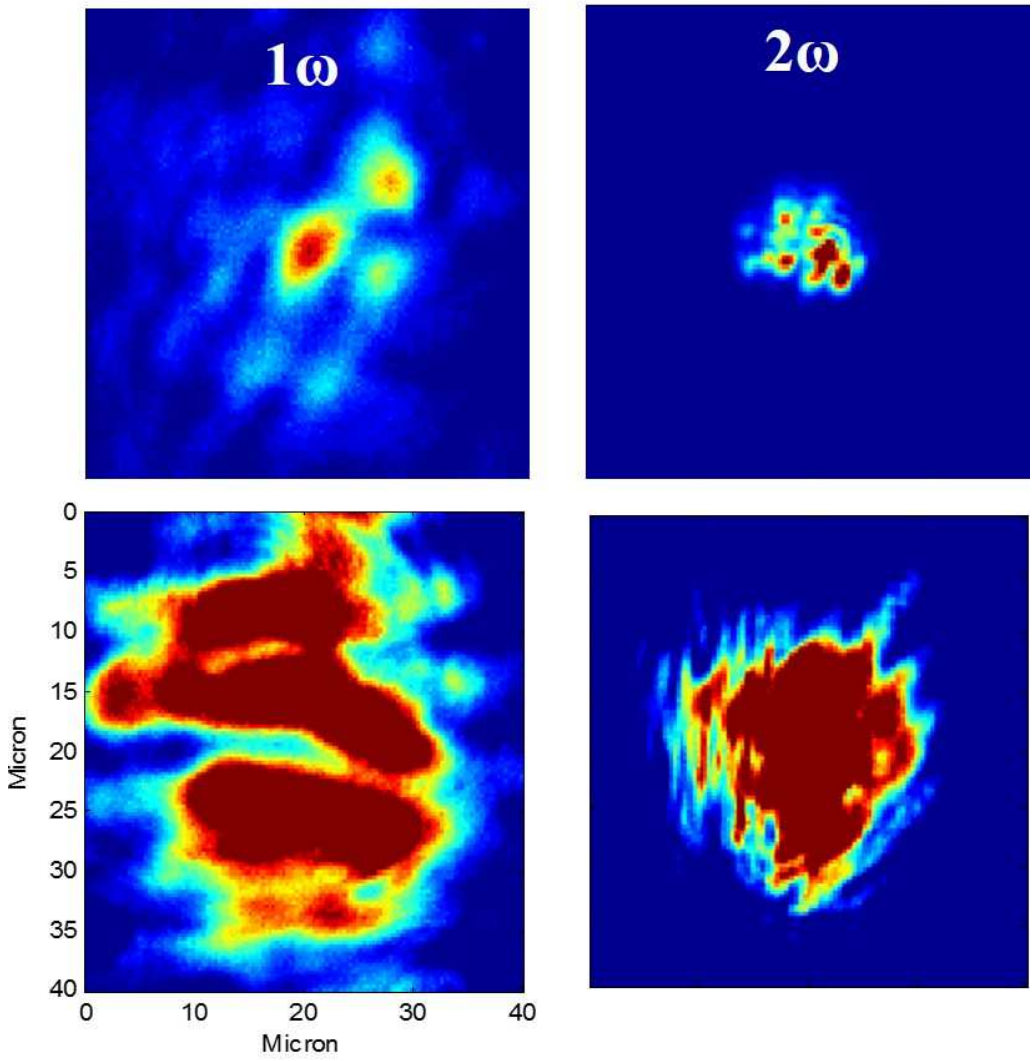

Figure 43: Typical CTR images for 200nm Al foil. The difference in images are typical of the large shot to shot variation.

The difference in the images above were typical of the shot to shot variation for a 200 nm Al foil. The CTR images were not repeatable within the same foil nor comparable to different foils. The images do not look like any existing published CTR data nor was

there any discernable pattern to analyze. Different target imaging techniques were attempted with no obvious differences. The ultrathin targets did not allow many shots ~4-5, per vacuum cycle. Also, several optics in the laser chain exhibited damage signs after a week of shooting. It was thought that the wrinkled targets reflected light back at near normal incidence. The reflected light was then collected by the OAP and sent back through the laser chain causing damage.

7.2.2 – 1.5µm Al Foil

The root cause of the unpredictable CTR images was not clear. A thicker target, 1.5µm Al, with a flatter front surface was selected. The improved front surface allowed the reflective z-scatter to be used and twice as many shots to be taken on target per vacuum cycle. A larger, more consistent set of data would hopefully allow more insight into the best target focal plane. To accommodate the thicker target, the beam splitter was replaced with a 65/35 ratio.

Typical CTR images from the 1.5µm Al foil are shown in figure 44. All the images are from the same foil. The viewing window is 40 x 40µm. The images at left are 1ω CTR with an ND 3.3 and 2ω CTR on right with ND 2.4. The intensity of the radiation is several orders of magnitude less than the 200nm foil, but without any repeatability or pattern. The images do not resemble anything found in the literature or in previous experiments within our group. The difference in the images is representative of the large shot-to-shot variation observed.

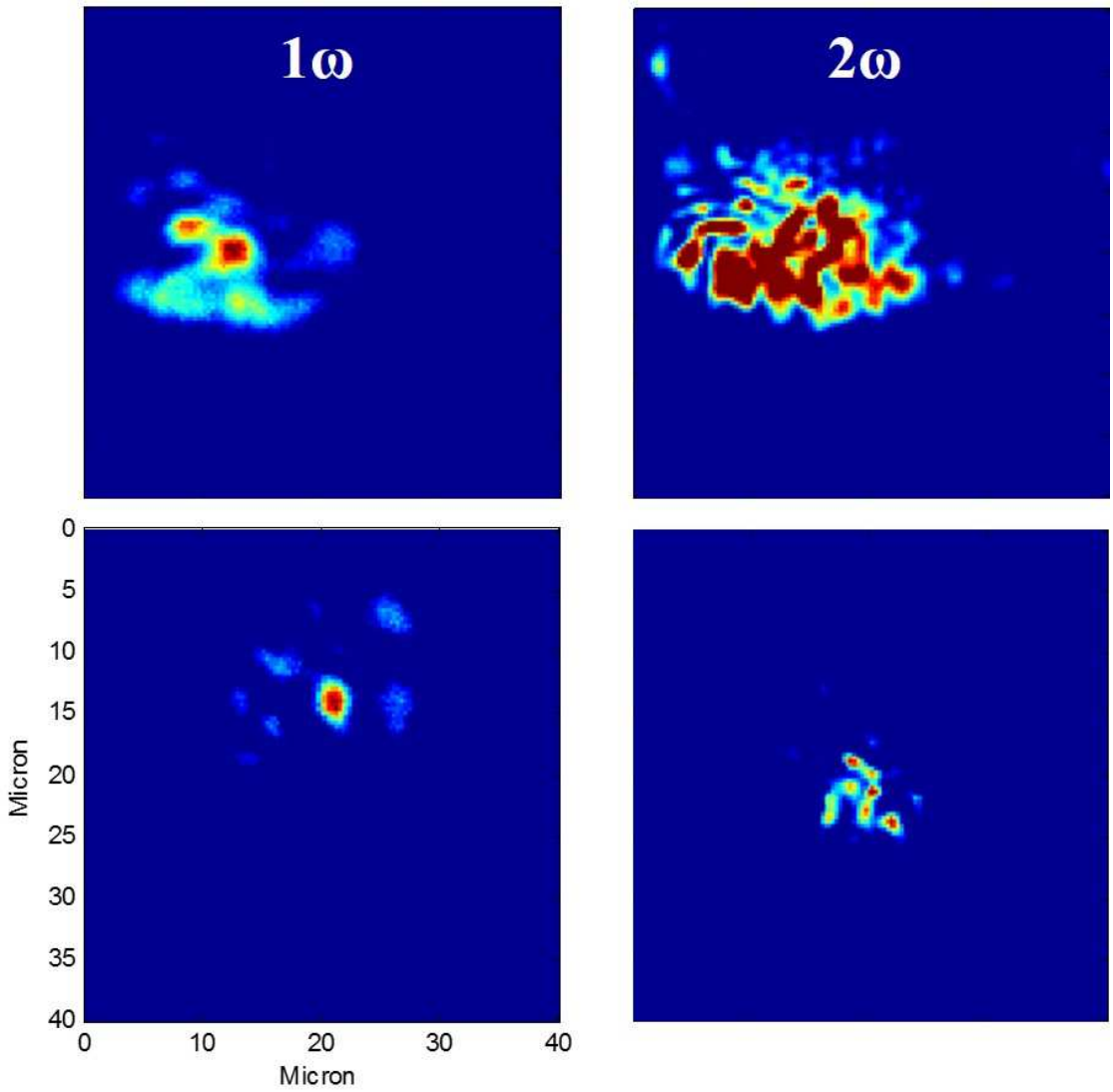

Figure 44: Typical CTR images for 1.5µm Al foil.

7.2.3 Far Field Diagnostic

The CTR images obtained up until now contained no obvious correlation with one another. The presumed root cause is the inability to align the target in the correct focal plane. A far field diagnostic was installed to assist in determining the location of the focal plane. The laser focus, or far field, would be measured simultaneously while

collecting CTR data. Any differences observed in the laser focus could be used to improve the focus in the experimental chamber. The emitted radiation from the acceleration processes are directed along two distinct directions: the laser k vector or normal to the target as shown in figure 45. The data collected up until now has consisted of filaments in irregular patterns. The location of the far field when compared to the CTR position could give insight into which acceleration mechanism is present or if CTR is observed at all.

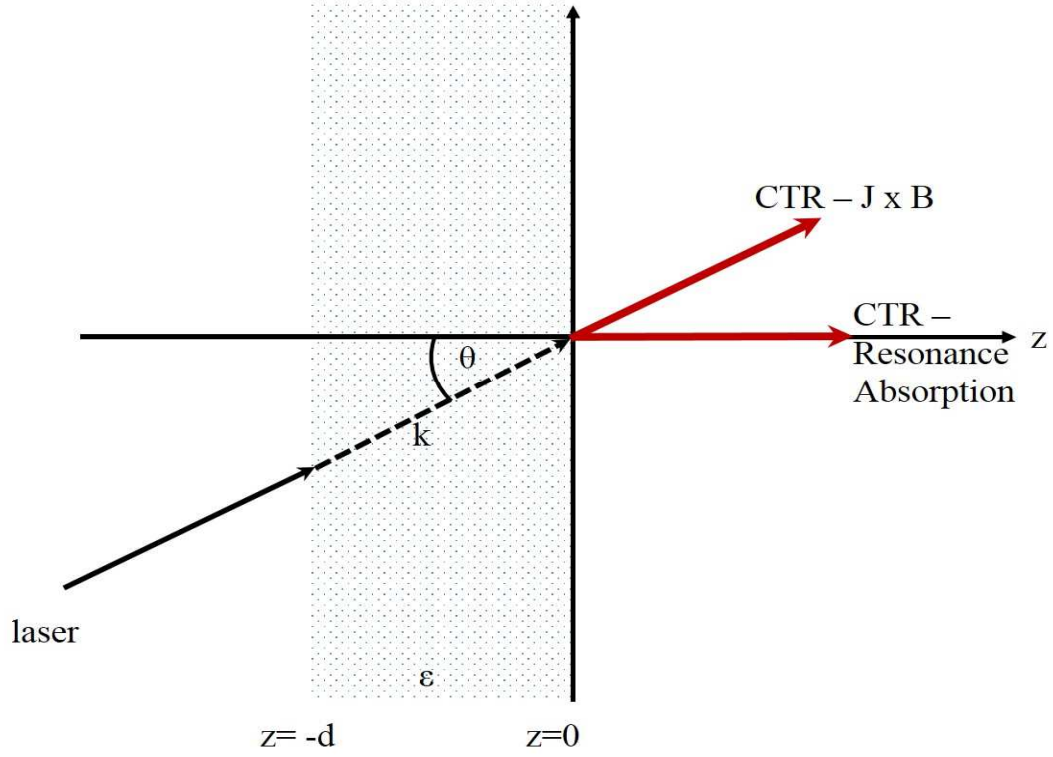

Figure 45: 2D schematic of CTR emission. One acceleration process is located along the laser k vector typically J x B heating. Another acceleration process is normal to the target, Resonance Absorption or Vacuum Heating.

A far field diagnostic was installed using leakage through a mirror in the compressor. The leakage can be observed using the oscillator at 76 MHz. The diagnostic was

installed to see how the laser focal spot corresponds to the centroid of the observed radiation. A 3 inch 1.5 meter focal length lens was placed in the compressor and a camera placed at the lens focal plane. The focus was approximately 1 meter outside the chamber in order to avoid optical damage or nonlinear effects. The oscillator light at focus is shown on the left in figure 46. A full system shot is shown at right in the figure. The difference in the two images is immediately noticed. The full system shot has a high degree of astigmatism acquired from a large polarizer located at the end of the laser chain.

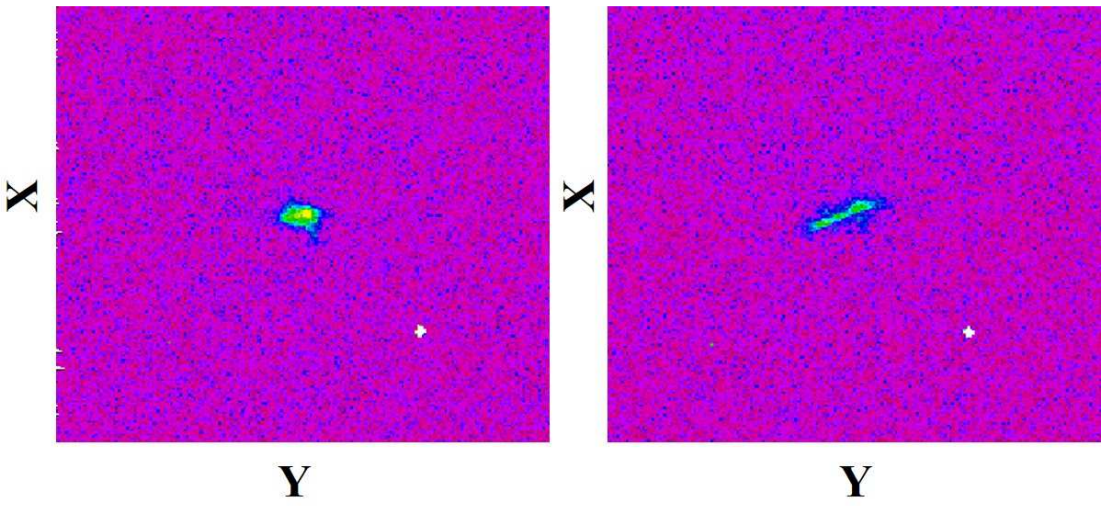

Figure 46: Images of the far field diagnostic shown for the oscillator only at left and a full system shot at right.

A well described feature of an astigmatic beam is perpendicular focal planes located on either side of a circular image, called the circle of least confusion. The oscillator focus is positioned in the circle of least confusion resembling a typical circular focal spot. When the full system shot takes place, the image is now outside the circle and is representative

of an astigmatic image plane located before the circular image. A simple schematic is shown in figure 47.

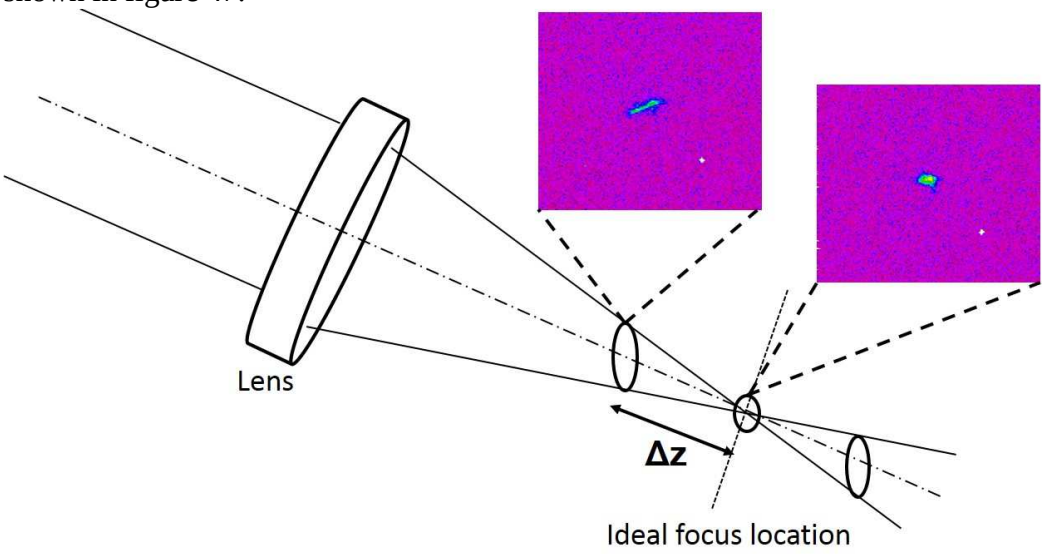

Figure 47: Simplified ray trace of an astigmatic beam brought to focus. Experimental images are shown in their corresponding locations in the ray trace.

However, the important point obtained here is the position of best focus *shifts* in z when taking a full system shot. The shift is attributed to the 300mm long glass rods. The rods are excited by flashlamps discharged at 15kV each which induce a thermal gradient along the radial axis. The thermal gradient acts as a lens shifting the plane of best focus away from the best focus observed with the oscillator or OPA at room temperature. In the target chamber, the beam astigmatism is corrected during the initial alignment of the OAP.

The amount of shift depends on the square of the f/# ratio of the optical system. This is basically the ratio of the OAP focal length and the 1.5 meter far field lens. The ratio for the target chamber and far field focal lengths was approximately 17. To move

the far field image into the circle of least confusion required a translation of almost 2mm for a system shot. Dividing 2mm by 17 yields a distance a little larger than 100 microns.

7.2.4 Initial Z-scan

A scan of best z position was then initiated starting at 60µm behind best oscillator focus (away from the focusing optic). The microscope objective images the CTR emission which is located on the back surface of the target. Thus, any z-scan requires movement of both target and objective. The technique implemented is to define an image plane with the microscope objective using the light from the oscillator. The microscope objective can then translated a known distance via a motor with an encoder. A diagram of the procedure is shown in figure 48. The target is then brought into the focal plane defined by the objective. In this way, the imaged plane could be controlled very precisely and moved only when the motorized stage is moved. This is a more accurate method than using the target to determine the z translation amount. Although the target can be precisely controlled, it would require reestablishing the desired focal plane each time after target replacement. The target is connected to a magnetic base, but still moves at least 20-30µm with respect to the previous target.

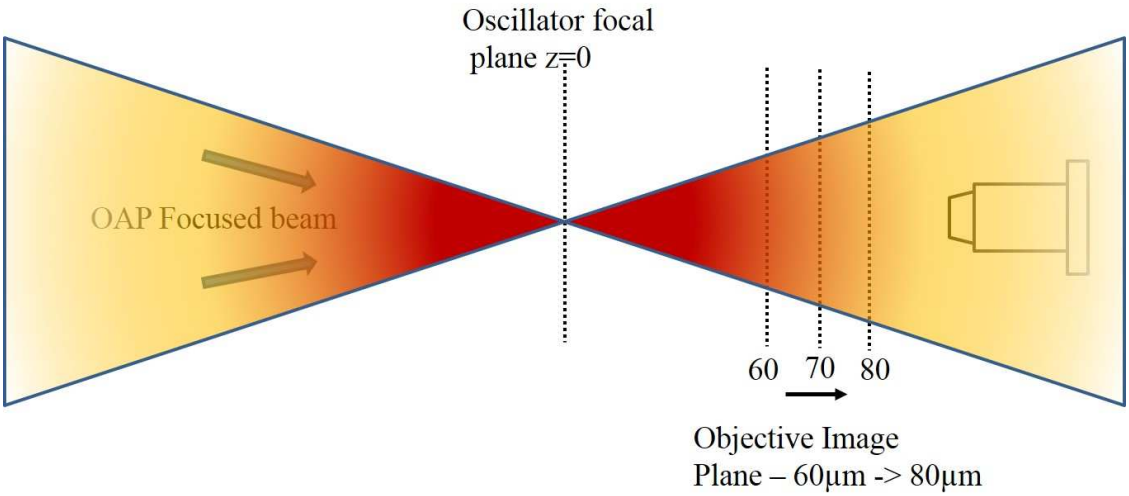

Figure 48: Diagram of the scanning technique. The microscope objective defines the image plane. A z-scan was performed by moving the objective away from the oscillator focus.

The result of the z-scan is shown in the figure below. The image plane was moved from 60 to 80 micron in 10 micron steps. The images are slightly saturated due to an increase in the radiation intensity as a result of moving closer to best focus. The radiation images coalesce into a single filament and emission intensity increases over an order of magnitude. The ND level for the 1ω CTR at 60µm was 2.9 and at 80µm the level was 4.1. This is attributed to the target being imaged at the correct location of the full energy focus.

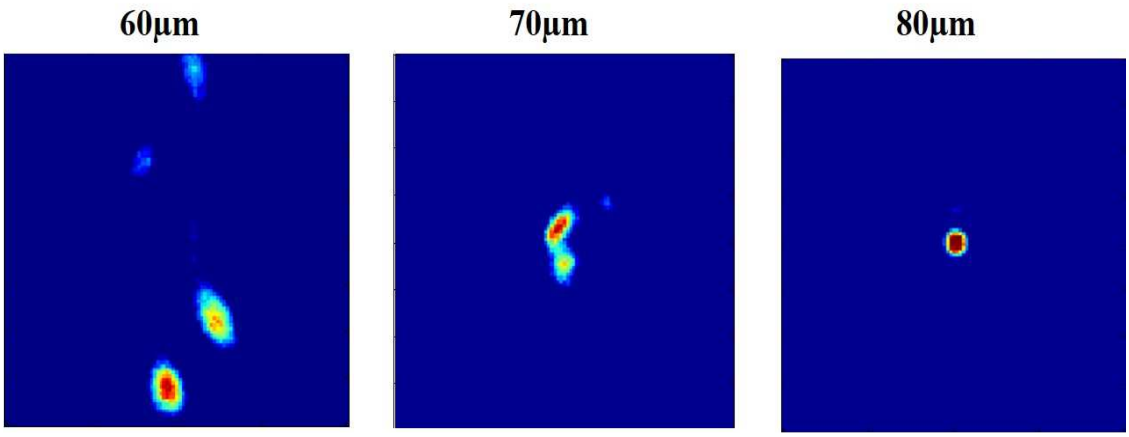

Figure 49: Z-scan images of 1ω CTR. Target locations from 60 to 80µm shown from left to right with 0µm defined as the oscillator focal plane. Viewing window is 40 x 40 micron.

7.3 PREPULSE IN GHOST LASER

Several experimental campaigns were interrupted by a sudden reduction in CTR intensity and a significant increase in area thought to be caused by a laser prepulse. The large area of CTR displayed multiple filaments with an irregular intensity distribution. A comparison with and without prepulse is shown below in figure 50.

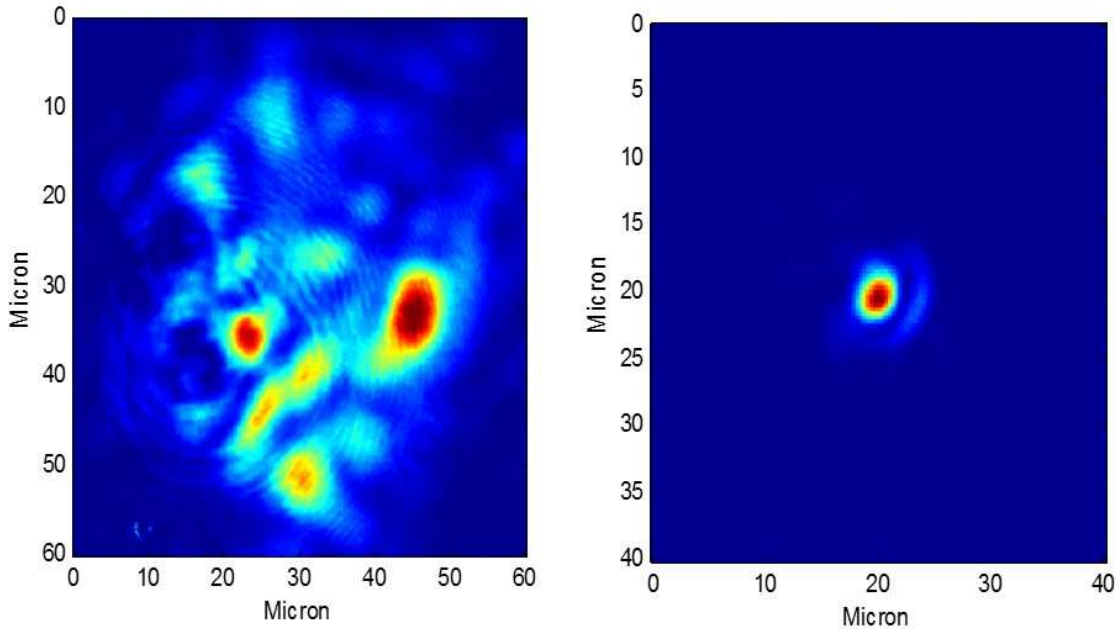

Figure 50: 1ω CTR beam affected by a laser prepulse (left). At the same conditions, a comparison 1ω CTR with no prepulse. The ND for the image on left is 2.2 and ND 4 on right. Note the viewing windows are different sizes.

The CTR divergence was attributed to laser interaction with a large amount of preplasma on the front surface from the laser prepulse. The emission intensity was constant over a large z scan - +/- 100μm from oscillator best focus.

The existence of a prepulse was investigated. The laser beam was focused on an EOT-3500 photodiode placed in the target chamber. The photodiode with a Tektronix 5104 oscilloscope allows a temporal resolution of 500ps. No distinct prepulses were observed on that timescale. A pedestal of amplified spontaneous emission 1000 times less than the main pulse was observed approximately 4ns before arrival of the main laser pulse. This was reduced to 10000 by inserting tighter pinhole spatial filters. The pulse contrast was examined on a shorter time scale, <100ps, with a 3rd order autocorrelator detailed in section 6.1.4. The autocorrelation revealed several pre-pulses. Two prepulses

corresponding to two postpulses were observed. These were assumed to originate from the autocorrelator measurement itself. One prepulse at approximately 40ps at an intensity of 10^{-5} of the peak intensity was unable to be accounted for. This was ultimately attributed to a pair of damaged dichroics in the 2nd stage OPA laser section. Replacing the dichroics caused the prepulse to go away. Data taking was resumed and the previous baseline CTR images were recovered. A plot of the 3rd order autocorrelation is shown in figure 51. In this image, the prepulse assumed to be the root cause has been removed.

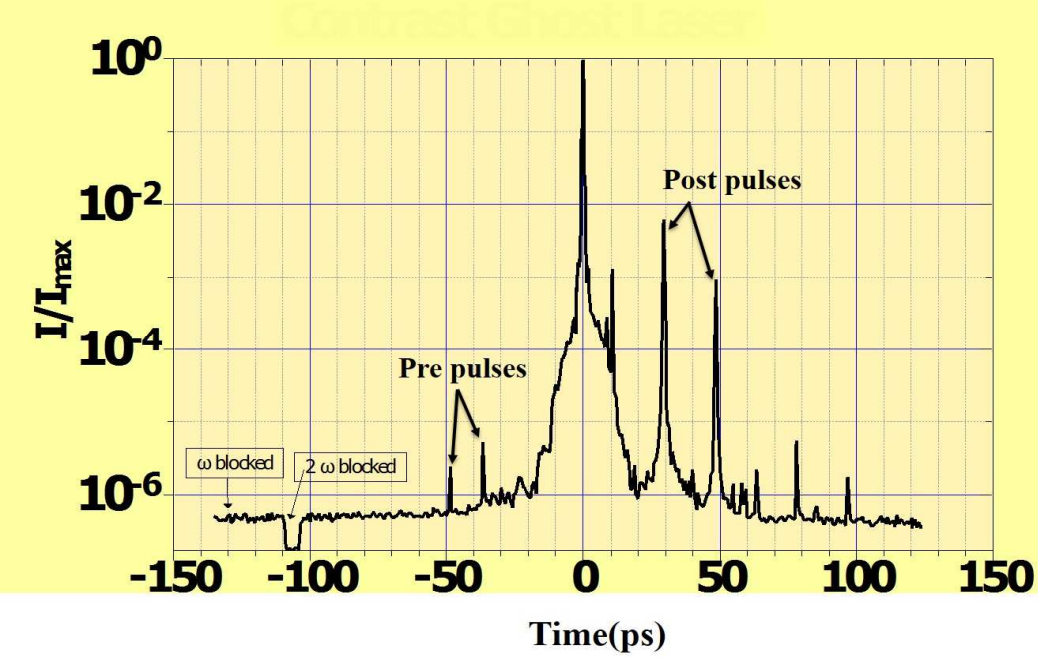

Figure 51: 3rd order autocorrelation of the GHOST laser. Pre and Post pulses shown are artifacts of the device. The prepulse affecting the CTR emission has been removed and is not shown in this scan.

7.4 BASELINE CTR MEASUREMENT

Once the optimal target image plane was determined, shots were taken to determine the general characteristics of the CTR radiation. The data were taken on the

1.5µm Al foil exclusively with the heating beam blocked. Unblocking and introducing the heating beam simultaneous with the main beam had no discernible impact on the CTR image.

Typical CTR images for 1ω, 2ω are shown in figure 52. The images provide information regarding the electron beam characteristics. The intensity of the CTR emission is dependent on the electron temperature distribution and the number of electrons. The CTR area gives a measurement of how collimated the electrons are transported through a target. The CTR emission appears as a single filament almost 2.5x smaller than the laser focal spot. It is not immediately known if only a central filament escapes the target or if the beam is pinched via an external source like the magnetic field.

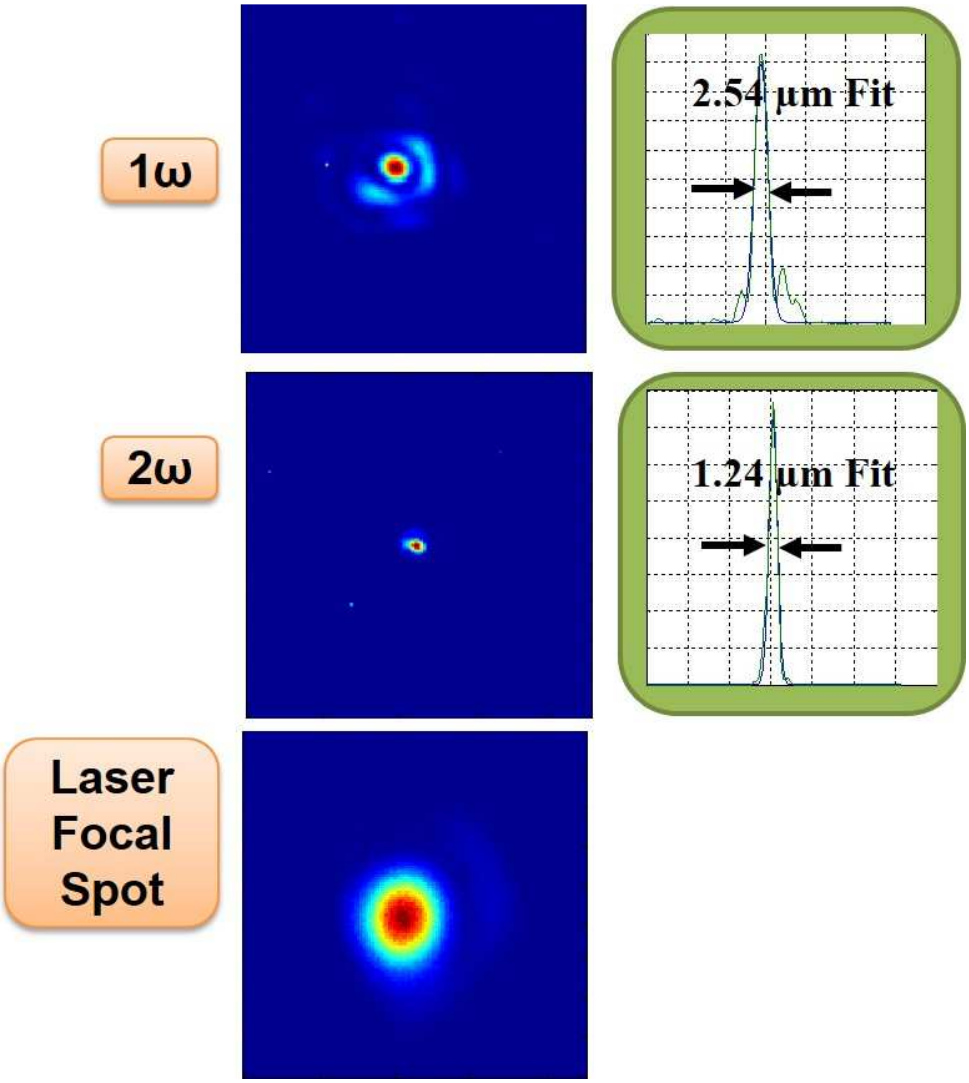

Figure 52: Images of 1ω CTR (top) and 2ω CTR (middle) alongside a Gaussian fit for each. The laser focal spot with FWHM 6.75µm is shown at bottom for comparison.

7.5 Analysis of CTR Data with 1-D Ballistic Model

A 1-D ballistic model of electron propagation [89] was used in conjunction with an absolute CTR energy measurement to determine the parameters of the electron beam.

The experimental CTR data was first calibrated and then the experimental data was fit using the 1-D model.

7.5.1 Calibration of CCD and ND filters

The ND filters used in the experiment were calibrated with a Cary 5000 UV-VIS NIR spectrometer. The spectrometer gives a precise transmission of the ND filter as a function of wavelength. The filter transmission is shown in figure 53 below.

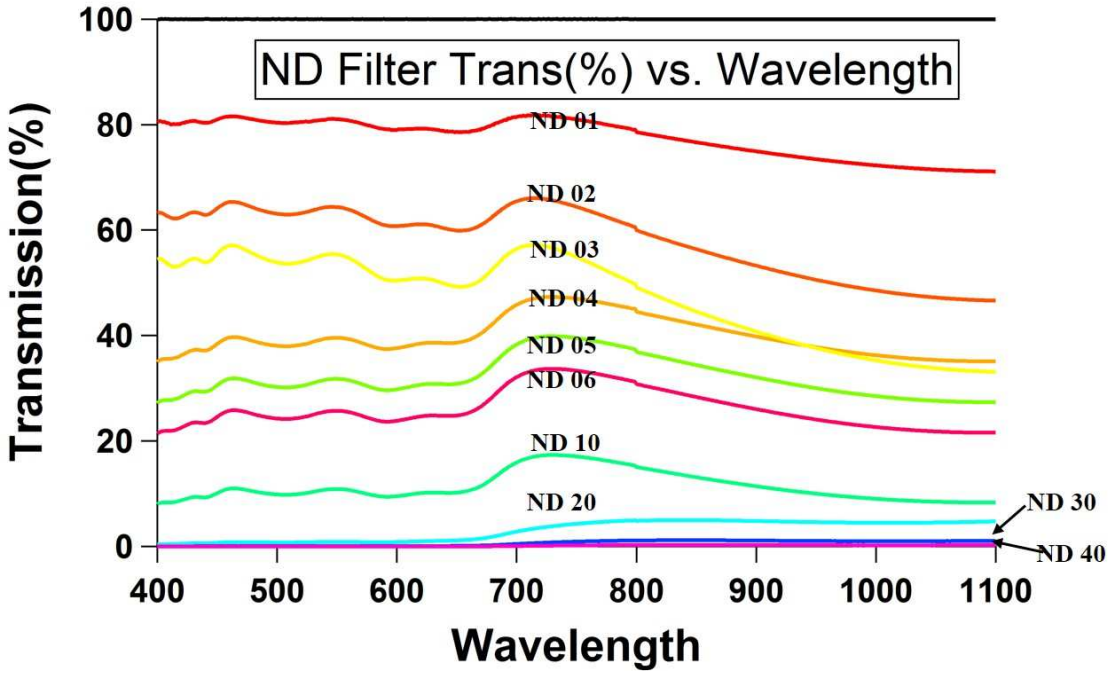

Figure 53: ND filter transmission measured with the Cary 5000 spectrometer. The black line is the reference measurement. The filter used are ThorLabs 2" square filter kit.

Using the known transmission of the ND filters, the response of the camera CCD sensor could be obtained. The two cameras used were IMI Tech IMC-11FT firewire with 1/3" CCD sensor. The modelocked oscillator was used as the incident light source. An oscillator frequency of 75.37MHz was recorded by an oscilloscope. The oscillator output

power was measured with an Ophir power meter yielding 18mW. From these two measured quantities, an energy per pulse was determined, .24nJ. Since the period of the oscillator is known, the number of pulses in a specific time window can be calculated. From the camera manual, the shutter open time was confirmed to be 16.67ms. Opening the camera shutter with a single trigger and using the calculated energy per pulse, the total energy in a time window can be calculated. An energy of 299μJ was estimated to be incident on the CCD sensor during the opening of the camera shutter. The CCD sensor response can be determined from the known values of the ND filter transmission and the energy incident on the camera from the oscillator. The CCD sensor maximum response was determined to be 23nJ. This is an average value that represents the energy of the entire area of the beam. On each shot, the nominal ND filter values for 1ω, 2ω CTR images are 4 and 5.1 respectively. Using the calibrated ND filter transmission values in conjunction with the CCD energy response, yields average CTR energies of 400 nJ for 1ω and 20μJ for 2ω. This corresponds to a CTR to laser conversion of $2.5*10^{-5}$.

7.5.2 1-D Ballistic Code Comparison

The ballistic code is developed from the theory described in section 5.2.2. The CTR spectrum is given by

$$\frac{d^2E_{CTR}}{d\omega} \sim N_b^2 \left| \begin{array}{c} \int d\tau dv \exp[i(\omega - q\cdot w)\tau \sum_{\alpha=1}^{\Lambda} \delta(\tau - \tau_\alpha - d/u) f_v(v) \exp[iq\cdot w\tau_\alpha] \\ \times \frac{\beta[\sin\theta - \beta\sin\Theta]}{\left[(1-\beta\sin\theta\sin\Theta)^2 - \beta^2\cos^2\theta\cos^2\Theta\right]} \end{array} \right|^2 \quad (73)$$

Here β is the electron velocity scaled with c, θ is the angle of observation, Θ is the electron emission angle, d is the target thickness, τ_o is the laser pulse duration, τ_n is the time when the nth bunch is created, $\Lambda = \frac{\tau_o}{\tau_n - \tau_{n-1}}$ is the total number of micropulses,

$N_b = N/\Lambda$ is the electron number in a micropulse, and $f_v(v)$ is the velocity distribution function. The distribution function is a relativistic Boltzmann given by

$$f_v(\beta) = \frac{\beta}{T(1-\beta^2)^{3/2}} \exp\left[-\frac{1}{T}\left(\frac{1}{\sqrt{1-\beta^2}} - 1\right)\right] \tag{74}$$

where T is the electron temperature normalized with mc^2 . The experimental parameters are well known. The target thickness is 1.5μm, laser pulse duration is 120fs, and the angle of observation is 15˚. The time interval between adjacent electron pulses is determined by the heating process. For processes occurring once a laser cycle, $\lambda_o / c = 3.5\, fs$ which yields $\Lambda = 30$ electron micropulses. For twice a cycle, $\Lambda = \frac{\lambda_o}{2c}$ yielding 60 micropulses. The electron distribution is not known, but can be inferred by working backwards from our experimental estimate of CTR emission and making several assumptions.

The first assumption is that 25% of the laser energy is transferred to electrons that contribute to the CTR signal. This conversion value was based on prior experimental evidence[99, 19]. The next assumption is the 2ω electron temperature scales as the ponderomotive force given by $9.33*10^{-14} \times I\left[W/cm^2\right] \times \lambda[\mu m]$ [25]. For a laser intensity of $1.25*10^{19} W/cm^2$ and wavelength 1055nm, this corresponds to an electron temperature distribution of 1.25MeV. This temperature value is plugged into the ballistic code. An appropriate electron bunch number is selected that yields a CTR value comparable to the experimentally measure value. At 2ω, 60 bunches with an electron bunch number of $8.8*10^9$ results in 19μJ of CTR emitted. This is very close to the experimental estimate of 20μJ. The electron number and CTR spectrum for 2ω are plotted in figures 54 and 55.

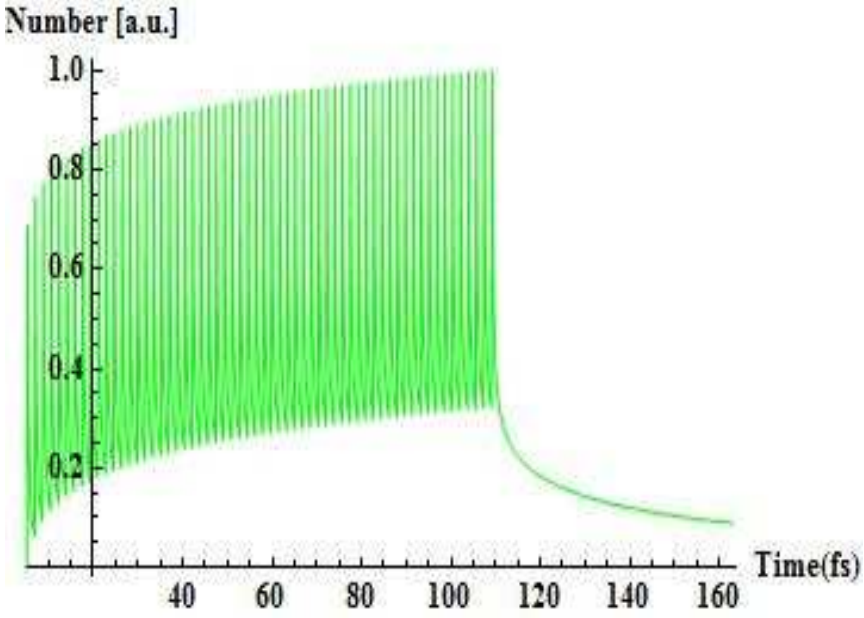

Figure 54: Normalized electron number at rear surface for 2ω CTR. The electron temperature is 1.25MeV.

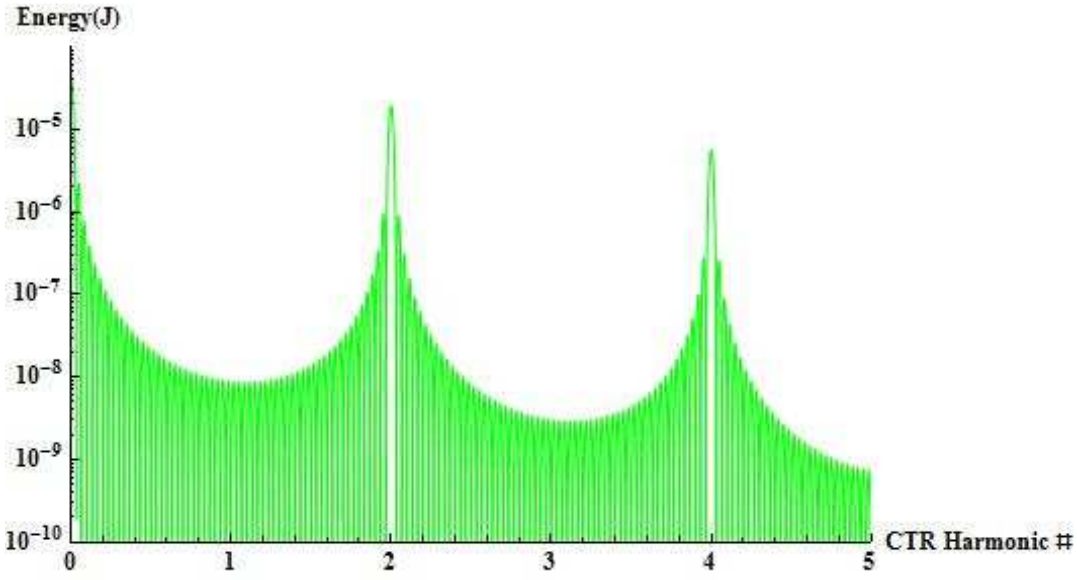

Figure 55: Harmonic energy spectrum for 2ω CTR. For 60 electron bunches with 8.8 $*10^9$ electrons per bunch, the CTR emitted is 19μJ.

Since 30 electron bunches are generated for 1ω, the electron temperature is fitted to satisfy both 25% laser energy conversion and the experimentally measured CTR value, ~400 nJ. The best fit was found using an electron temperature of 2.5MeV and $6.6*10^9$ electrons per bunch. For these parameters, the electron number and CTR spectrum are plotted in figures 56 and 57. In comparison, if Beg's scaling law $T \approx 100keV\left(I\lambda^2\right)^{1/3}$ was assumed, the result would be an electron temperature of 500keV. $1*10^{11}$ electrons per bunch would be required to obtain the experimental value. This would require virtually 100% conversion from laser to hot electrons which is unrealistic. The high electron temperature suggests the CTR emission is due primarily to the electrons in the high energy tail of the distribution.

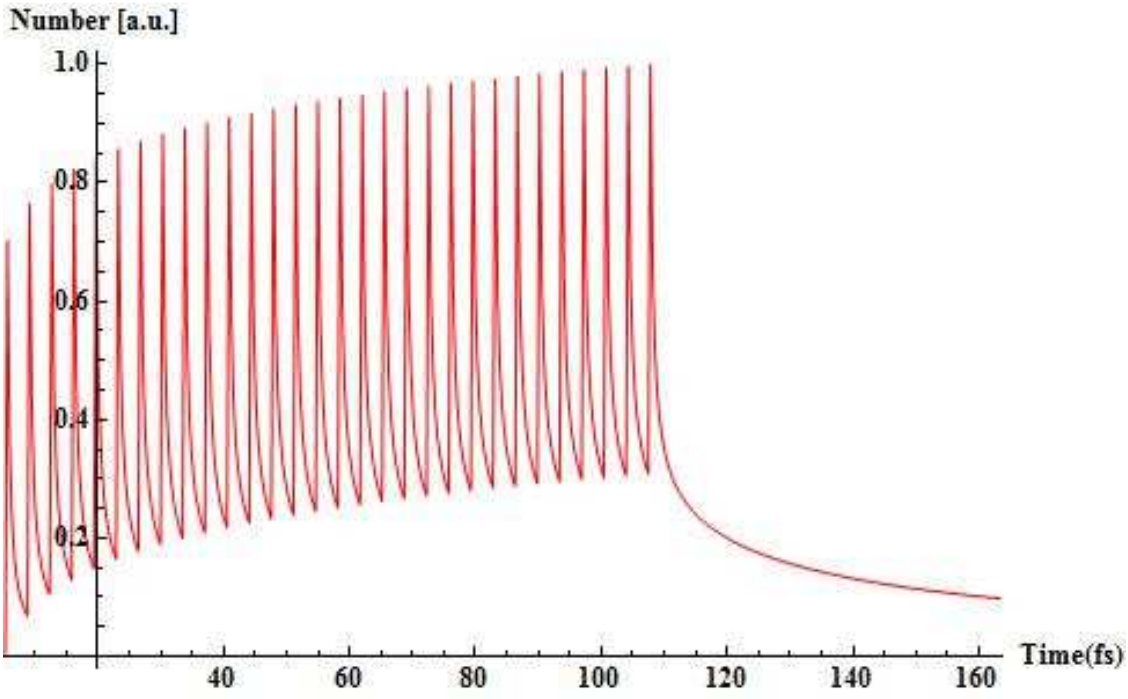

Figure 56: Normalized electron number at rear surface for 1ω CTR. The electron temperature is 2.5MeV.

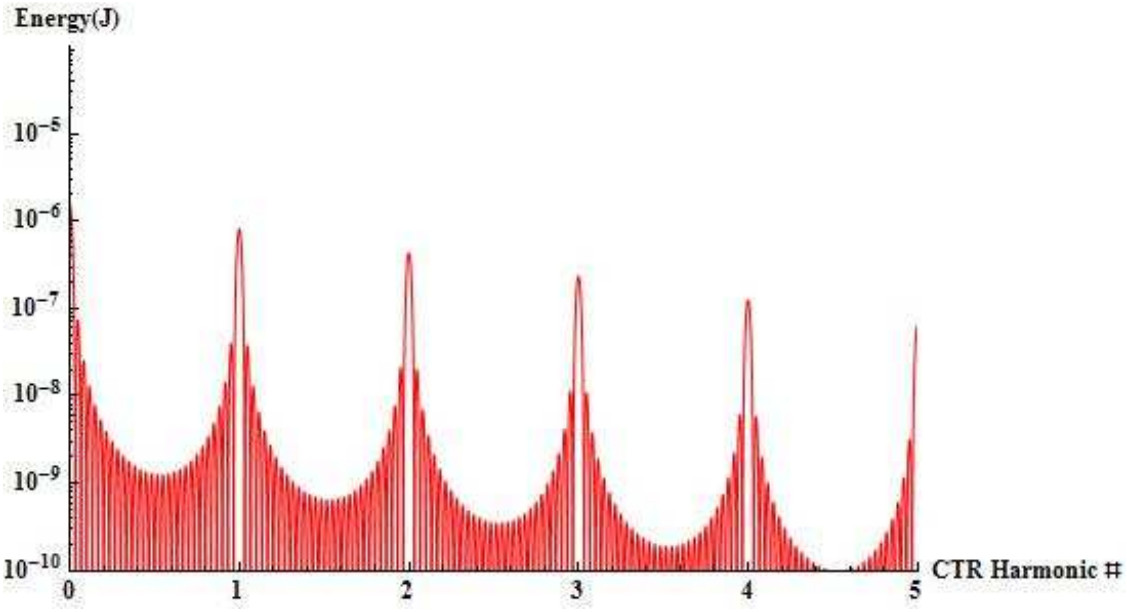

Figure 57: Harmonic energy spectrum for 1ω CTR. The electron temperature is 2.5MeV.

The experimental parameters, laser-CTR conversion, electron temperatures and number of electron, calculated by the ballistic code compares well to similar published experiments [49, 50, 79, 96, 102, 103]. The assumption of 2ω energy scaling with the ponderomotive force has been experimentally verified [96, 102]. The 1ω CTR energy of 2.5 MeV is plotted against several other results [49, 50, 79] with the first name author listed as the experiment name in figure 58. Here, UTexas is the experiment described in this thesis. It should be noted that the laser intensities are all comparable with the exception of Batani that is 3 – 4 times higher.

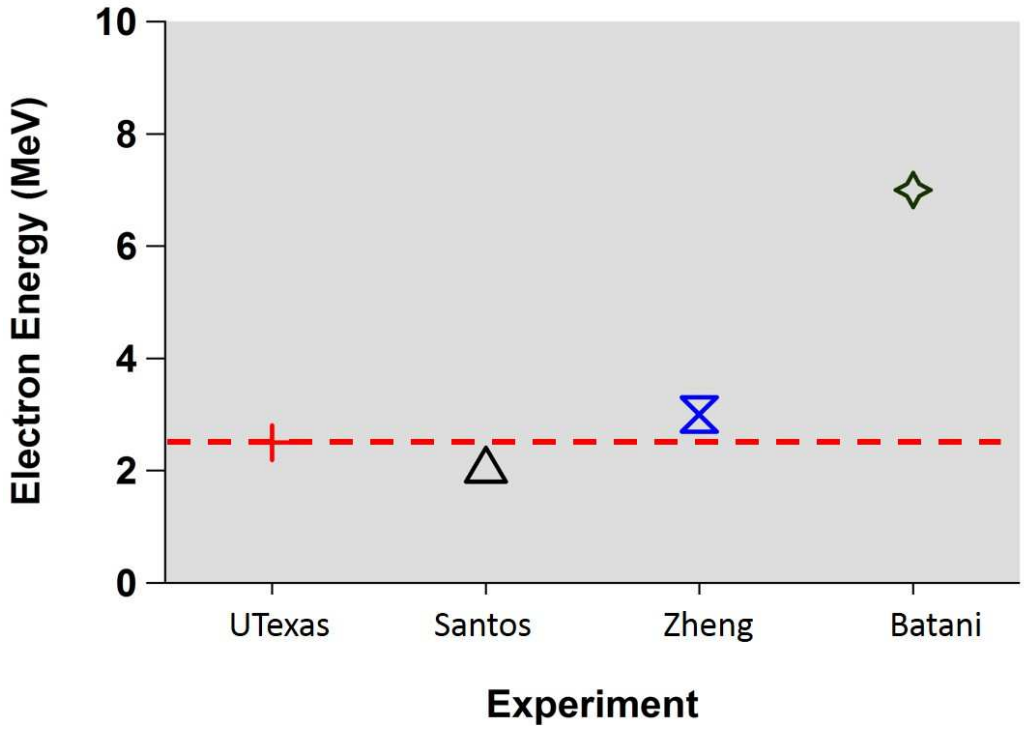

Figure 58: Comparison plot of published1ω CTR energy values. Dotted red line shows location of University of Texas energy estimate.

The laser to CTR conversion is plotted in figure 59. The first author is listed as the name of the experiment.

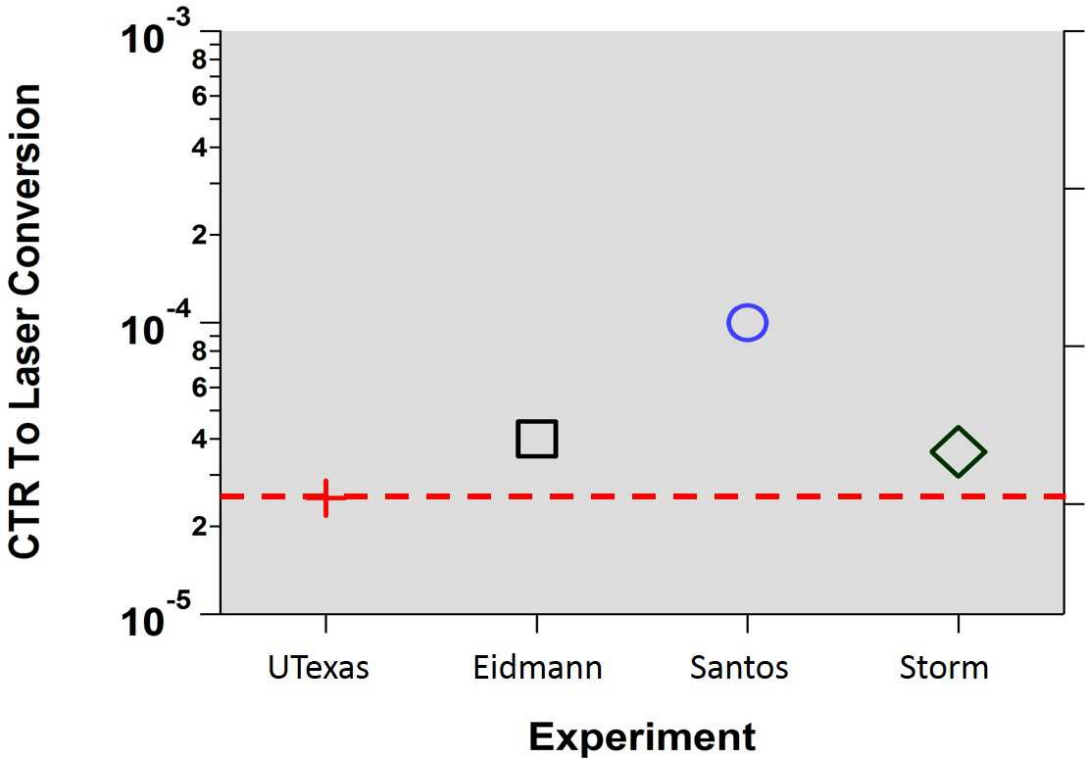

Figure 59: Comparison plot of published laser/CTR conversion values. Dotted red line shows location of University of Texas energy estimate.

7.6 OPTICAL PROBING OF TARGET SURFACE

In order to determine the impact of the heating beam on the target, surface reflectivity as a function of heating beam delay was measured. The reflectivity was measured using an optical probe on both the front and rear target surface. In this case, the main beam was attenuated and frequency doubled for use as an optical probe. Since the heating beam is rather large 250-300µm, the main beam was expanded to ~2mm at the target surface using an f=-400mm plano-concave lens. A schematic of the beam overlap is shown in figure 60. The surface of the target was imaged with a 10x infinity corrected microscope objective. From the objective, the beam is directed out of the chamber to a lens doublet forming a telescope with a magnification ~2-3. The beam is

then viewed on a camera with a cut off filter allowing only the 2ω frequency doubled light. The beams are overlapped temporally by the method described in section 6.2. The main beam experiences a delay due to the additional optics required for the frequency doubling, etc. This should be no more than 2-3ps. The beams were spatially overlapped using an IR card. This was much harder to do in practice than it appeared – two beams hitting a point in space from two different angles. So, a single pulse from the heating beam was fired on target creating a hole in the target. The heating beam is then blocked and the hole in the target centered on the probe beam

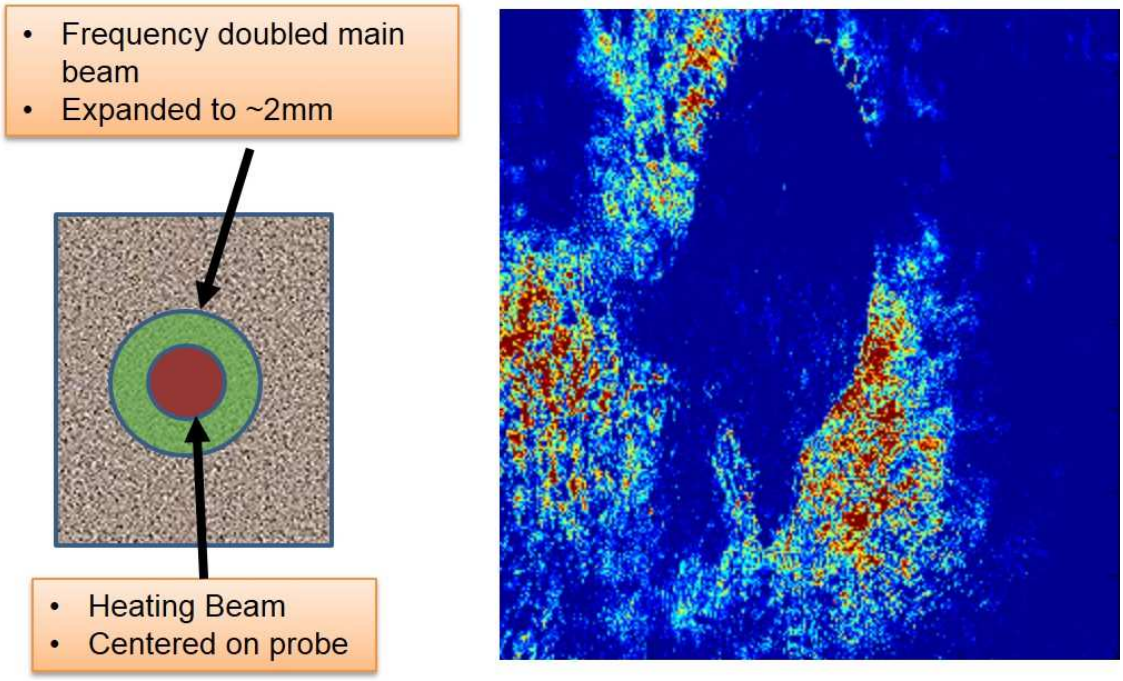

Figure 60: At left, Diagram of the heating and probe beam at the target surface. On right, heating beam imprint used for probe beam alignment.

Three shots were taken at each heating beam delay starting at t=0ps. The three shots at each time step were averaged. The heating beam was delayed in 10ps increments from 0 to -100ps. A given region of interest was selected according to the alignment of the heating beam and the energy contained in the region was integrated. At 0ps, the integrated energy in the region was assumed to correspond to a reflectivity of 100%. For comparison, the heating beam was delayed to come after the main beam, t=+10ps. Additional shots at t=+10ps which yielded similar results to the energy measurement at 0ps. Therefore, we can conclude that 100% reflectivity at 0ps is a reasonable assumption. The plot of reflectivity for the front and rear surface is shown in figure 61. Values larger than 1 on the graph are attributed to frequency conversion of the probe beam away from an image plane. The reflectivity on the front surface shows a sharp drop after 40ps. This indicates that either the front surface temperature is increasing or the preplasma from the target blow off is a factor. According to the HYADES model, the temperature should not be increasing so it's probable the reflectivity drop is due to the plasma on the front surface. The rear surface maintains a 100% reflectivity for greater than 100ps. This verifies the thermal wave does not generate a shock or discontinuity that influences the rear surface. A sharp interface is maintained throughout the experiment which is verified by the observation of CTR.

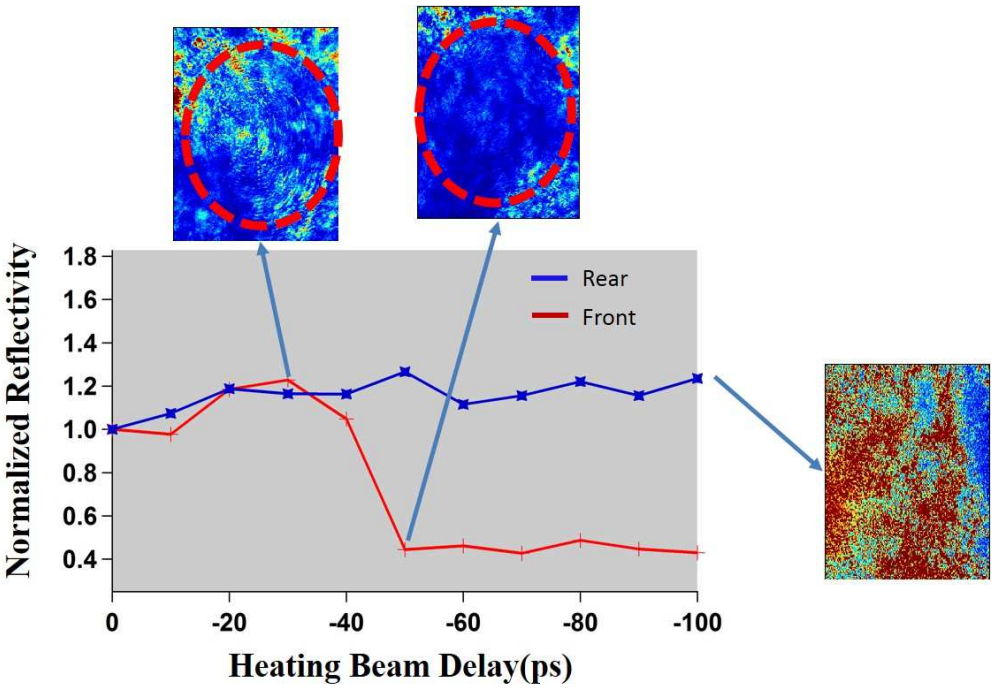

Figure 61: Plot of the front and rear surface reflectivity of 1.5µm Al foil as a function of heating beam delay.

7.7 CTR COMPARISON OF AL VERSUS AL/PLASTIC

7.7.1 1ω CTR Energy

The 1ω CTR energy was recorded for two different targets: a conductor, Al, and a dielectric, Al/plastic. The energy was determined from the signal recorded on the CCD by integrating over a specific area. The selected area is equivalent in size to the laser focal spot, 7.5µm by 7.5µm, and the image was centered in the region as shown in figure 62.

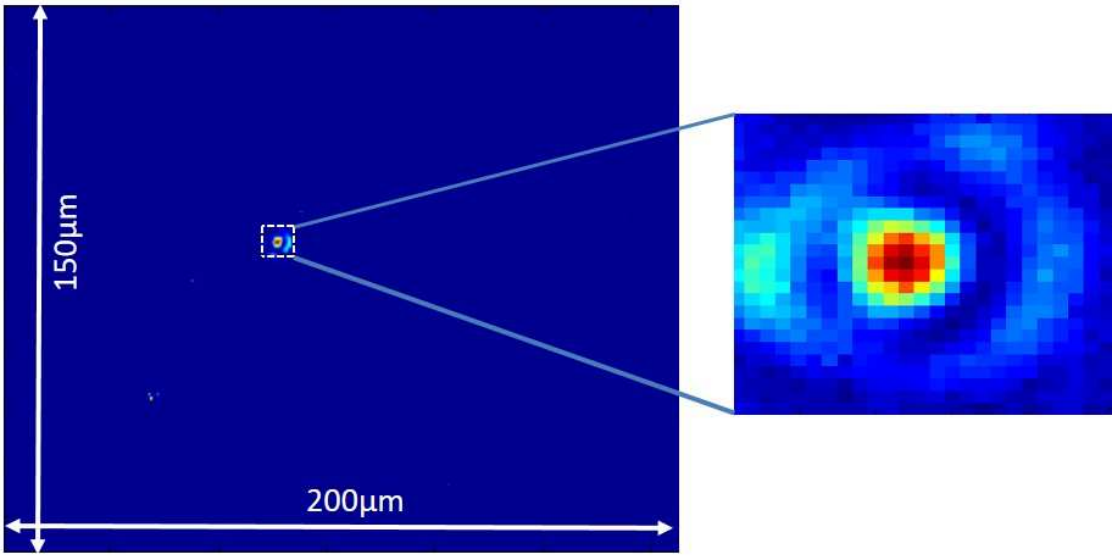

Figure 62: Full camera viewing window of 1ω CTR. The 7.5µm x 7.5µm window used to integrate the CTR energy is shown with the respective image.

Approximately 20 shots were recorded on each target with the average shown in figure 63. The energy values for both materials are approximately equal and within the standard deviation.

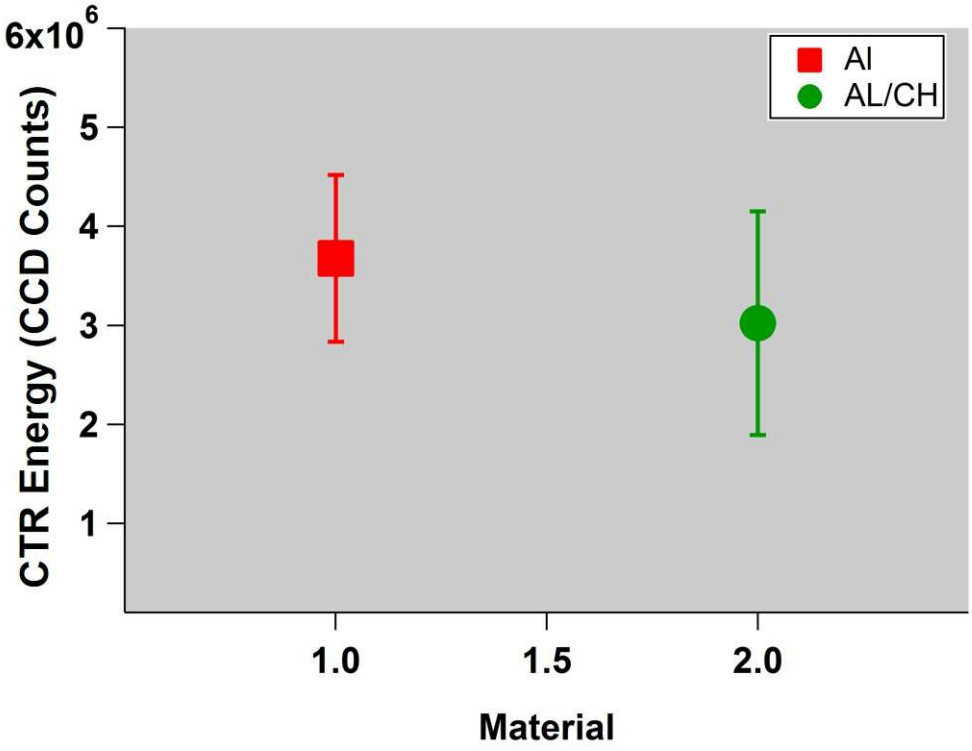

Figure 63: Comparison of 1ω CTR energy in two different target materials – Al & an Al/plastic sandwich target.

7.7.2 1ω CTR Area

For the same shots, the area of the radiation was analyzed. A larger window, 40 x 40µm, was used. This was due to some of the images contained multiple filaments and were irregularly shaped making a Gaussian fit difficult. Some examples are shown in figure 64. The Al/Plastic targets clearly show greater radiation spreading and filamentation.

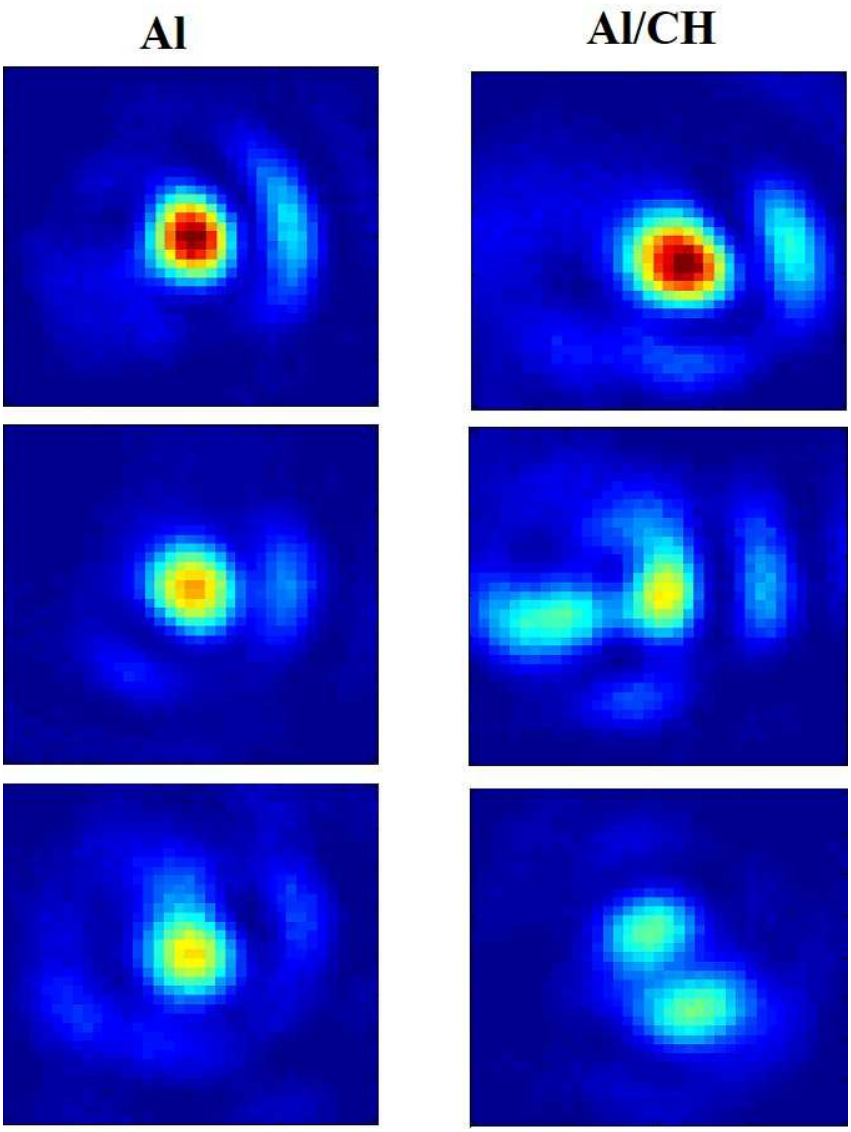

Figure 64: 1ω images for Al target (left) and Al/Plastic (right). Viewing window is 20 x 20μm.

The averages of the 1ω CTR area are plotted in figure 65. The Al/Plastic targets show a 2x greater area than the Al targets. The increased electron divergence is suggestive of return current inhibition in a dielectric material.

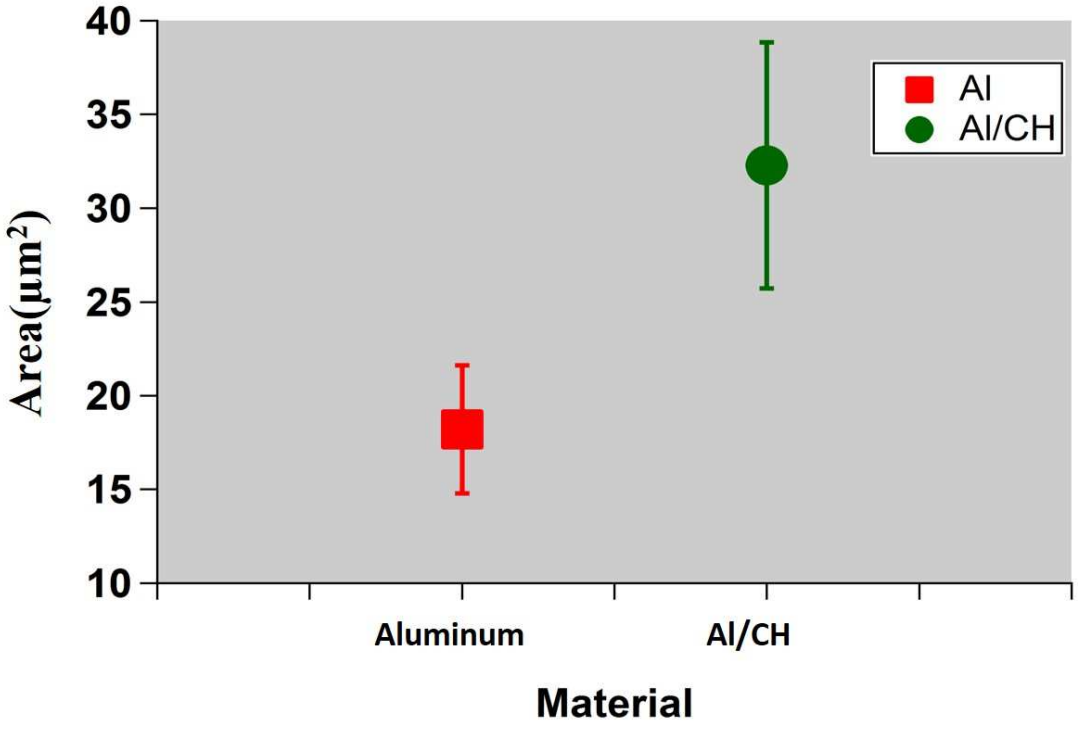

Figure 65: Comparison of 1ω CTR area in two different target materials – Al & Al/plastic sandwich target.

7.7.3 2ω CTR Comparison of Al versus Al/Plastic

The energy and area of 2ω CTR data was taken in a similar manner. Plotted in figure 66 and 67 are the average of 20 shots. The 2ω CTR energy is 30 percent greater for the Al foil compared to the Al/plastic sandwich target. However, the 2ω CTR area was similar for both target types. The laser target interaction should be similar due to the Aluminum front surface, the results of the 2ω area suggest electron collimation in the two different acceleration mechanisms are effected differently.

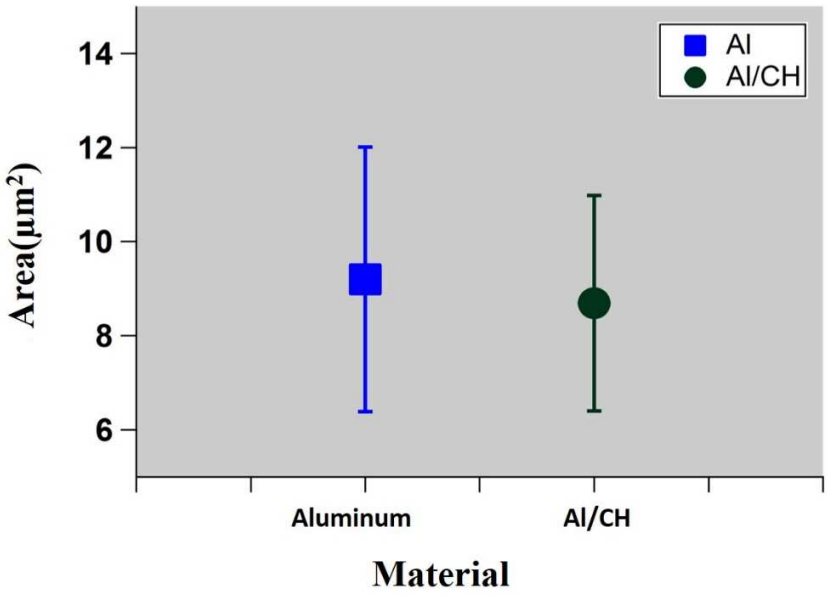

Figure 66: Comparison of 2ω CTR area in two different target materials – Al & Al/plastic sandwich target.

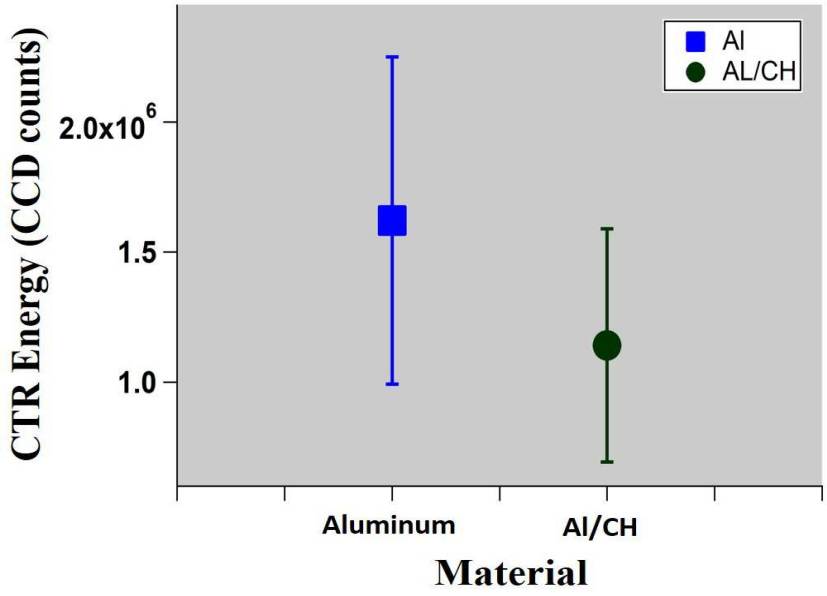

Figure 67: Comparison of 2ω CTR energy in two different target materials – Al & Al/plastic sandwich target.

7.8 CTR Comparison of Al – Heated/Unheated

7.8.1 1ω and 2ω CTR Energy

The heating beam was now introduced prior to the arrival of the main beam and electron propagation through heated material was measured. On each foil, the first shots were taken with the main and heating beam simultaneously hitting the target at t=0ps. This was done until the baseline CTR shown in section 7.4 was observed. After repeated observation of the baseline CTR signal, the heating beam was advanced in time 20, 40, or 60ps with respect to the main beam. For the last 2-3 shots left on the foil, the heating beam delay is moved back to t=0ps. In this scenario, data were taken at two time steps for each foil. This also verified the laser quality over the course of the foil.

Since two delay times were measured on each foil, a ratio of two delay times were obtained for both CTR energy and area. Unheated Al, t=0ps, was then compared separately against the three heating beam delays, -20, -40, and -60ps. Approximately 15 shots for each time delay were taken and the average CTR energy calculated. The energy was calculated over an area the size of the laser focus similar to the method described in section 7.7.1. Figure 68 shows the 1ω and 2ω CTR heated/unheated energy ratios for each time delay. Energy ratios ranged from 0.5 to 0.8 for 1ω and from 0.3 to 0.7 for 2ω. For each the heating beam delays, a ratio <1 means the heated material emits less radiation than the unheated material. The reduced CTR emission corresponds to a reduction in the number of electrons escaping the target.

7.8.2 1ω and 2ω CTR Area

The CTR area is calculated in the same manner as described in section 7.7.2 and a ratio of heated/unheated is plotted in figure 69. The CTR area for the heated targets is larger than the unheated (t=0ps) targets. This results in a ratio >1 for each case. Ratios

ranging from 1.1 to 1.3 were observed for both 1ω and 2ω. For all time delays, heated Al emits less CTR radiation over a greater area when compared to unheated Al. Typical CTR images are shown in figure 70.

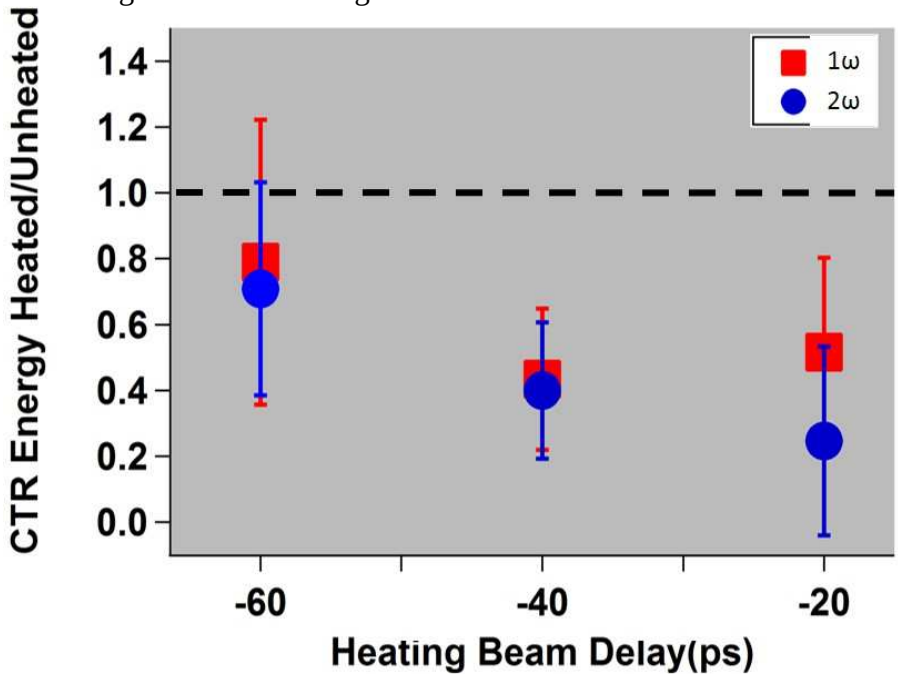

Figure 68: Ratio of CTR energy for unheated vs heated Al targets is plotted. The ratio is the average of 15 shots.

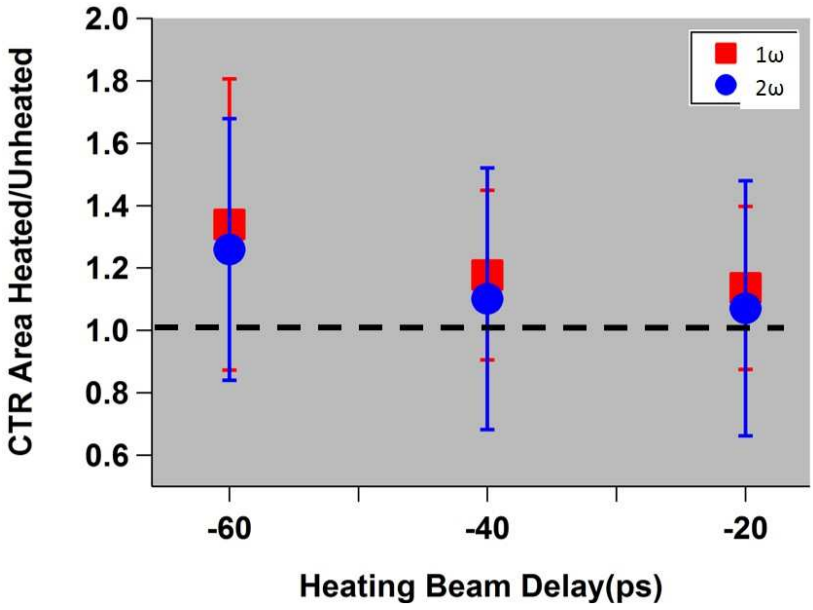

Figure 69: Ratio of CTR area for unheated and heated Al targets is plotted. The ratio is the average of 15 shots.

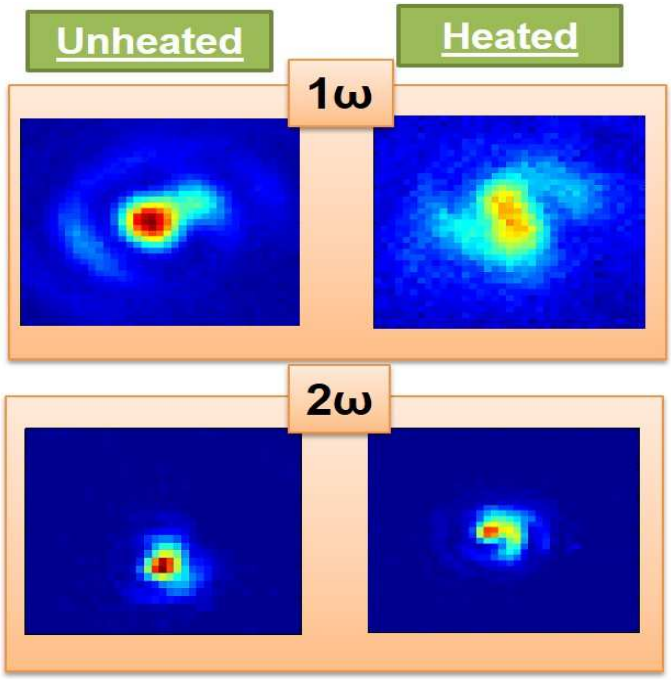

Figure 70: Typical CTR images of heated and unheated Al. 1ω CTR are in the top row with 2ω in the bottom. Unheated images are on the left.

7.8.3 RC Circuit Model of CTR

The hot electron and return currents can be approximated through an analogy to an RC circuit. Here, the laser provides an alternating voltage source, the bulk material is the resistor and the accelerated electrons are analogous to charging a capacitor as shown in figure 71.

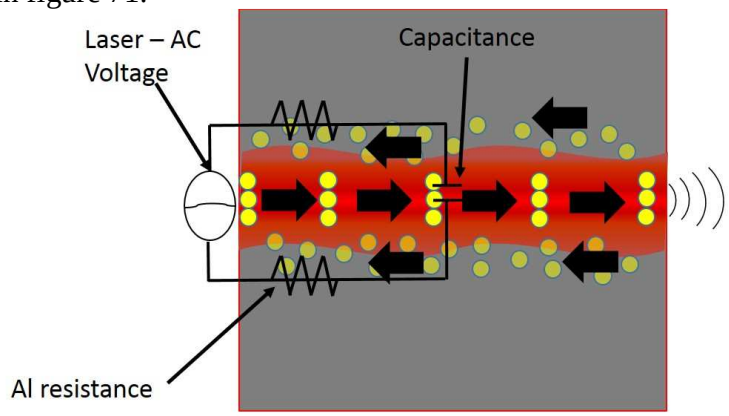

Figure 71: RC Circuit analogy of electron current transport in aluminum.

The impedance of the circuit can be calculated by

$$Z = \sqrt{R^2 + \left(\frac{1}{\omega_L C}\right)^2} \tag{75}$$

where R is the value of the material resistance and $1/\omega_L C$ is the capacitive reactance. The capacitance is approximated as a hemisphere with radius equal to the 1ω CTR radius ~1.3 μm and ω_L is the laser frequency. The unheated resistivity values are well known and obtained from any solid state physics textbook. Here, we use Ashcroft & Mermin [62] which gives $2.45*10^{-8}\Omega\cdot m$. The heated values are slightly more difficult to interpret due to the lack of extensive experimental data in this regime. Here, we select a value that agrees with both theory and experiment for temperatures ~10eV. The experimental results of Freeman and Milchberg [34] have been fit analytically [73]. The analytical fit gives a value of $\approx 2.0*10^{-6}\Omega\cdot m$. This value is compared to the

conductivity of Lee & More [63] which gives a value of $1.5*10^{-6}\Omega\cdot m$. The value we use is the mean value of the experiment and theory $1.75*10^{-6}$. The resistance is obtained from the resistivity by using the hemispherical geometry with radius of 1.5 μm. This value is slightly larger than the CTR radius and equivalent to the target thickness of 1.5 μm.

The impedance is related to the current via $I_{\max} = \frac{V_{\max}}{Z}$. The main laser pulse for both heated and unheated scenarios are the same so $V_{\max}$ is a constant. Plugging in the different impedance values for heated and unheated, a ratio of the heated versus unheated current is obtained $\frac{I_{unheat}}{I_{heat}} = \frac{Z_{heat}}{Z_{unheat}} \approx 1.05$. This result confirms the experimental results of the previous section in that more current flows when the material is less resistive. In the 1-D ballistic CTR model [89], a reduction in current corresponds to less electrons accelerated per cycle. Plugging in the reduction in current yields a CTR ratio of 0.90 shown in figure 72 as the yellow line. This simple model expresses the correct physics and gives a reasonable result suggesting that our measured parameters are valid.

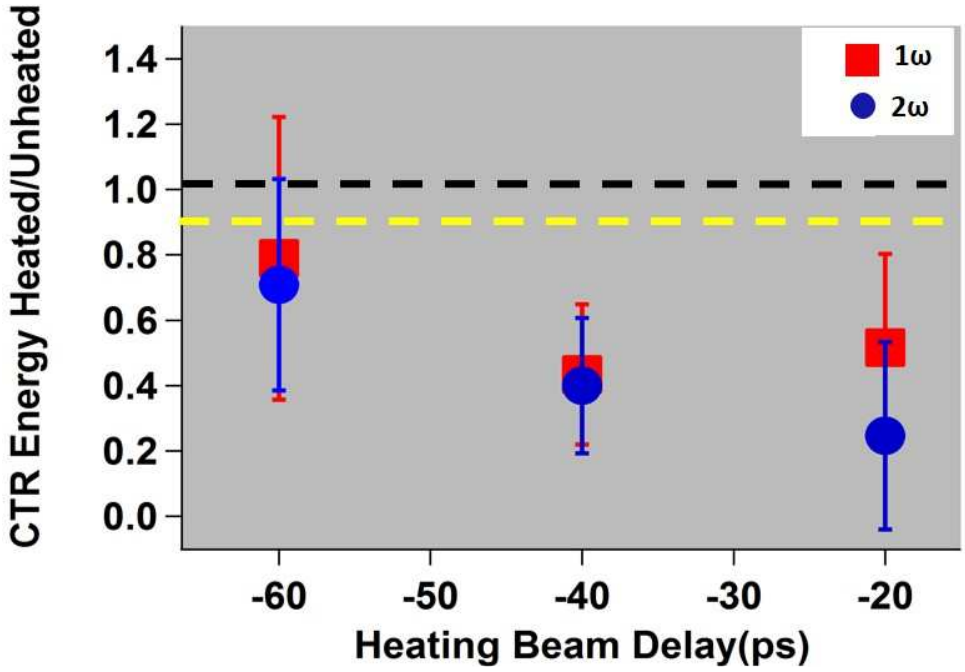

Figure 72: Comparison of CTR energy in heated and unheated Al. The yellow dotted line indicates the CTR estimate from the RC circuit analogy.

7.9 CTR Comparison of Al/Plastic – Heated/Unheated

In a dielectric, an intense laser pulse will ionize the medium providing electrons available to generate a return current. The conductivity will increase from zero in a perfect insulator and transition to a value comparable to a metallic conductor. Thus, the expectation is a heated dielectric medium will be more receptive to electron transport. 1ω CTR area and energy were recorded for heated and unheated Al/plastic sandwich targets in a procedure similar to Al targets. The heating beam propagates through the plastic faster due to the reduction in density. Therefore, the time steps selected are -42ps, -28ps, and -14ps.

7.9.1 1ω CTR Energy Comparison

The 1ω CTR energy ratio for heated/unheated Al/plastics is plotted in figure 73. The energy ratio for each heating beam delay was averaged over 15 shots.

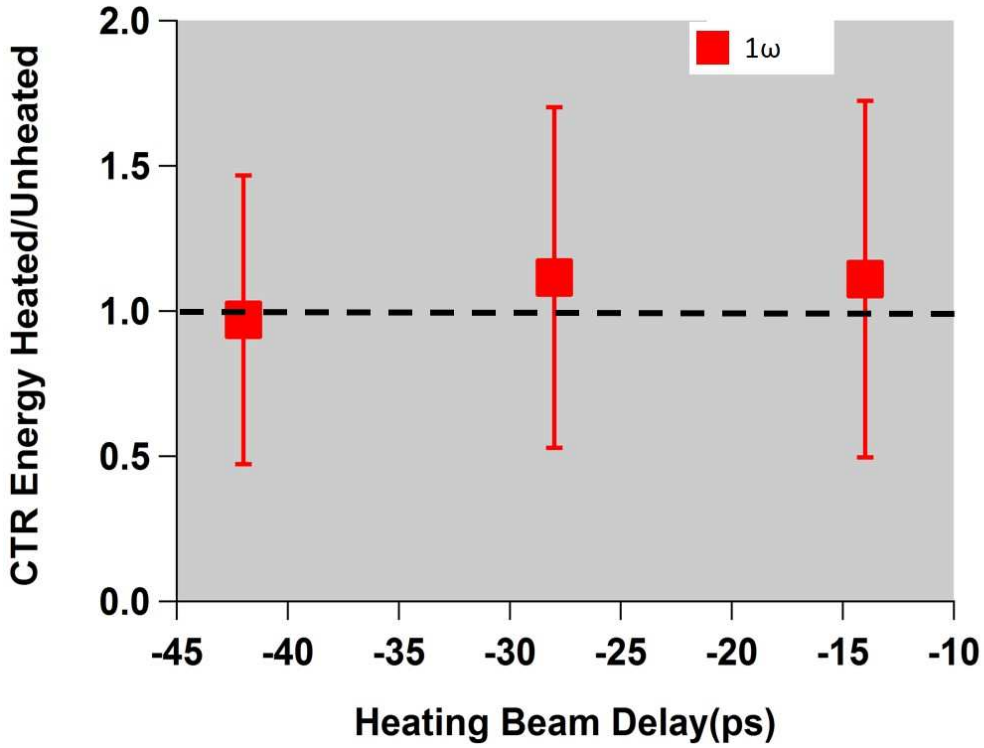

Figure 73: Comparison of 1ω CTR energy in heated and unheated Al/Plastic. Ratio of CTR energy for unheated and heated Al/CH targets is plotted. The ratio is the average of 15 shots.

The ratio for each time delay ~1. The result is not completely surprising for a couple of reasons. The heating beam only weakly ionizes polyethylene resulting a material conductivity not precisely known. The first 100nm of the target is Aluminum which has been heated and thus experiences a reduction in conductivity as a result. This result also serves as a contrast to the aluminum foil which saw a reduction in CTR when heated.

That the heated Al/plastic targets experienced no reduction in CTR energy indicates the influence of the heating beam plays a secondary role.

7.9.2 1ω CTR Area Comparison

The 1ω CTR area ratio for heated/unheated Al/plastic is plotted in figure 74. The ratio in each time step is very close to 1. The results reinforce the assumptions provided by the energy.

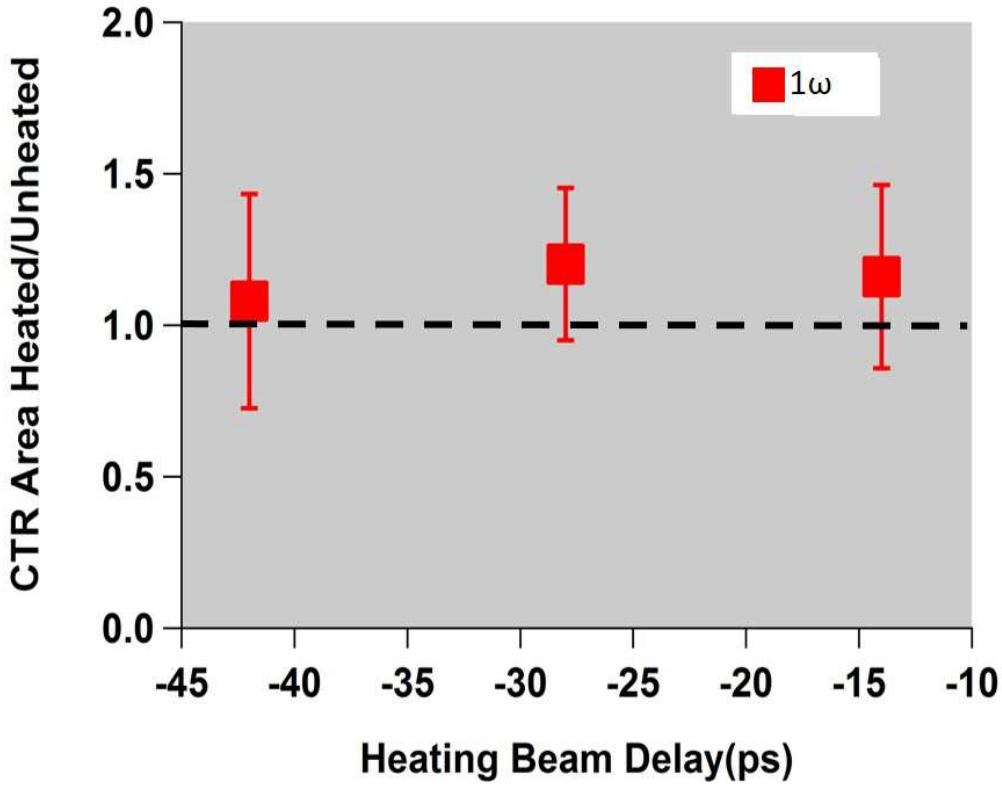

Figure 74: Comparison of 1ω CTR area in heated and unheated Al/Plastic. Ratio of CTR area for unheated and heated Al/CH targets is plotted. The ratio is the average of 15 shots.

7.10 INITIAL PIC CODE SIMULATIONS

For further investigation of the effects leading to the CTR spectral structure, we have conducted initial 2D PIC numerical simulations with similar conditions as used in the experiment employing the EPOCH [104] 2D PIC code.

A simulation box of 11x14 µm was used with a resolution of 100 cells and 40 particles per cell and species. The target consisted of a neutral slab of Al with 1.5µm thickness that has an exponentially decaying pre plasma density at the front surface. Higher ionization stages were computed using the Ammosov-Delone-Krainov rates. The electron density and magnetic field perpendicular to the simulation plane at the rear side of the target where sampled at times steps corresponding to c/4.5µm. The electron density and magnetic field are shown in figures 75 and 76. Both show clear harmonics emitted at two different emission angles.

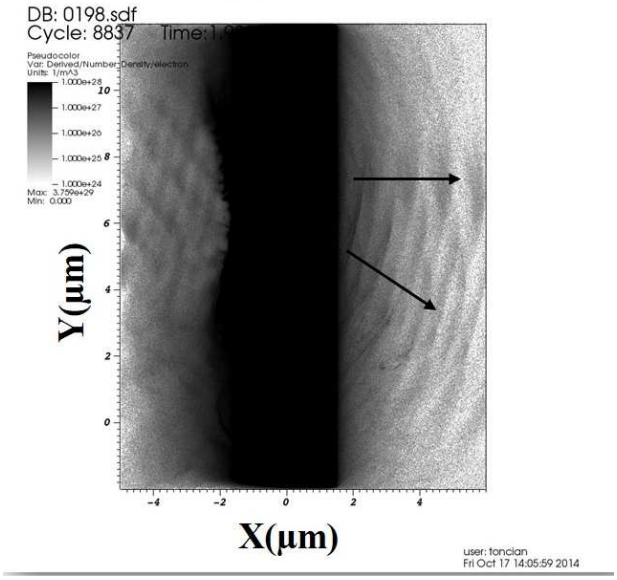

Figure 75: EPOCH simulation of electron density for 1.5µm Al foil. The arrows indicate two distinct directions of electron densities corresponding to CTR emission.

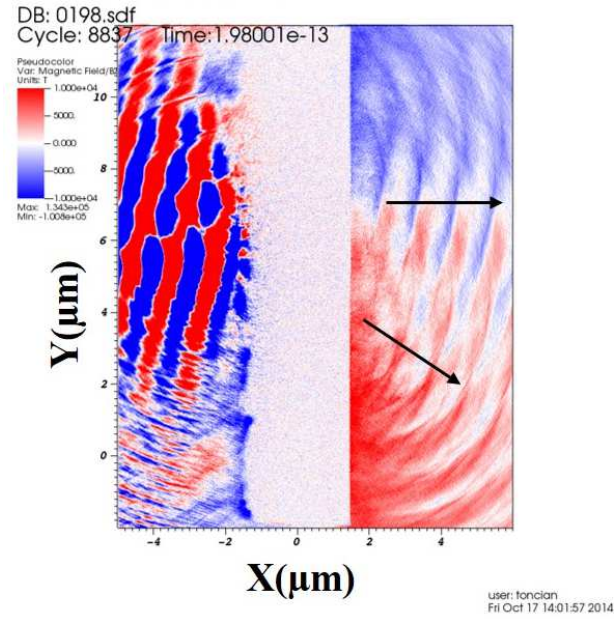

Figure 76: EPOCH simulation of B field for 1.5µm Al foil. The arrows indicate two distinct directions of electron densities corresponding to CTR emission.

The CTR consists of discrete harmonics which are angularly separated in space. The future direction is to take a Fourier Transform of the fields at the back surface of the target. This must be done such that the angular distribution of electrons can be resolved and filtered for only the desired harmonic. The value at each time step will then have to be integrated to represent the signal observed in the experiment.

Chapter 8: Conclusion

8.1 SUMMARY

The goal of this thesis was to obtain insight into the role return currents play in hot electron transport. Return currents are governed by the bulk material conductivity through $j_{return} = \sigma E$. It has been observed [100,101] that the return current density is the primary source for target heating and serves as the dominant stopping mechanism for hot electrons. Quantifying the response of return currents to changes in material conductivity will aid in the understanding of hot electron propagation.

The material conductivity was influenced in two ways – changing the temperature and selecting different materials. A conducting material, Al, was compared to an insulator, polyethylene. A 2nd laser beam, the heating beam, at low intensity heated the target to a temperature 1-10eV. In aluminum, this resulted in a reduction in conductivity. The insulator will experience an initial increase in conductivity due to an increase in available electrons via laser ionization.

Coherent transition radiation was the diagnostic used to evaluate the electron transport. CTR exhibits clear peaks at the first and second harmonics of the laser frequency. This indicates there are two acceleration mechanisms present. The baseline CTR measurement made on Aluminum indicates a single, highly collimated filament for 1ω, and 2ω approximately 2.5 times smaller than the laser focus. Comparing the Aluminum CTR emission with the Al/plastic target, a clear difference in the electron divergence of the low conductive material emerges. The 1ω CTR area was 2x larger for the Al/plastic target while the integrated energy was similar. The 2ω CTR was relatively consistent for both target materials indicating that the different electron generation mechanism might be affected unequally. The aluminum targets were preheated at different delays with respect to the main beam and compared to the baseline CTR. The

heated Al targets exhibited a reduction in emitted energy and a greater divergence. This was observed for both 1 and 2ω CTR and suggests the difference is due to the difference in conductivity.

Since the target heating is performed with a laser pulse, the front and back surface reflectivity of an Al foil were measured. The main beam was frequency doubled to 2ω and increased to ~2mm at the target plane for use as an optical probe. The heating beam was centered with respect to the optical probe and the reflectivity of the probe measured in the location of the heating beam. At the front surface, the reflectivity dropped to 50% at 50ps and the back surface showed no change in reflectivity out to 100ps. This supports the results of the hydrodynamic model with the assumption we are generating a thermal heating wave that decays with material interaction.

The CTR emission from heated and unheated Al/plastic targets were evaluated and found to be similar for each heating delay time. As a result, no unambiguous conclusion about the Al/plastic targets could be obtained. However, the fact that the heated Al/plastic data is different than the heated Al data suggests that the heating beam influence on the observed CTR is minimal.

The experimental evidence collected during this thesis work shows a clear difference in CTR emission in high versus low conductive media. The emitted radiation directly reflects the electron beam characteristics at the target back surface. Increased divergence and reduced radiation intensity were observed for low conductive media. This was true whether the conductivity was reduced by heating the target or the material was inherently low conductive. This indicates that the material conductivity significantly influences electron propagation through the inhibition of return currents on micron scale distances.

8.2 FUTURE WORK

The concept of propagating high currents of electrons through dense plasmas continues to be of great interest to the high energy density community. The work presented here is an effort to better understand electron transport. The laser parameters available limited the target foil thickness to several microns. In the current experimental geometry, different materials, specifically high Z metals, could be shot and compared. The high Z metal is more collisional and would provide insight as to how much influence collisions exert in a micron length foil. Additionally, the return current would heat the target more rapidly through the increased collisions. A larger laser with a dedicated probe line could enable heating of thicker targets on the order of 10-20 microns. This would enable greater interaction time between the hot electrons and the return currents in the bulk medium.

However, using a laser driven thermal wave to heat target thicknesses greater than several microns comes with the drawback of a large preplasma on the front surface. Another alternative heating mechanism would be to use protons to heat the target. The protons generation would originate from a secondary foil. This increases the requirements on the laser system. With the continued operation of the Texas Petawatt and similar laser systems increasing, accessibility for the necessary laser architecture is not an experimental roadblock. The benefit of the protons is the local deposition of energy. An appropriate laser pulse with an appropriate filter could preferentially select protons that exclusively heat the target interior leaving the front surface of the target minimally affected. Heating could also be accomplished with x-rays, one example being the coherent light source, LCLS, at SLAC.

Additional diagnostics could be fielded that would give more insight into the relevant physics. The preplasma scale length could be more precisely determined

through a probe beam and interferometer. The temporal evolution of the target temperature could be measured via streaked optical pyrometry. Electron transport in overdense targets is a very rich and complex physical problem with many questions still to be resolved.

Appendix A Hyades Input File for Heating Beam on Al Foil

This is the input file for HYADES hydrodynamic simulation. The library and EOS are included in HYADES. Gilliss Dyer ran the additional EOS file on line 16.

```
c
mesh   1 41 0.0e-6 10e-7 1.03
mesh 41 89 10e-7 100e-7 1.01
mesh 89 189 100e-7 1500e-7
region 1 188 1 2.7 2.6e-5 2.6e-5
material 1 13. 27. 1.
eos 44 1
c
c EOS XEOSElec2130.dat 1
c EOS XEOSIonD3130.dat 1
c an attempt to use hyadlib:
c eos 2130 1
c eos 3130 1
c
ioniz 1 3 .0001  $ Thomas-Fermi model
DATA ioniz 1 XEOSZeff4130.dat
data thrmcond 1 1.5e-3 2.33e+14
c
c Laser: 1.06 micron, P-pol, 0 deg. incidence
c
source wave 1.06 +1 1 0
```

```
gauss .6e-13 5e+22 1.3e-13
c
c  Room temperature dielectric constant
c
data refindx 1 .00015 0.49
data absindx 1 .00015 4.86
c
c Melting data

data tmelt 1 1.05e-4 1.5 1.97
data metal 1 1 9.1e+13 0.65 1 1 3.48e+25 1 2.67e+14

c Post Processor Arrays
c
pparray r rcm te ti rho dene deni taue tauei zbar elecon0 pres deplas conde condi
c
parm alvism .3
parm qstimx 5.e-5
parm flxlem .05
parm xlwabth 1.e+10
parm temin 26.e-6
parm timin 26.e-6
parm trmin 26.e-6
c
parm dtmax 10.e-15
```

```
parm editdt 5.e-13
parm postdt 5.e-13
parm tstop 150.e-12
parm itmcyc 50
parm nstop 1000000
```

Appendix B CTR 1-D Model

CTR ballistic model adapter from J. Zheng, et al., Physics of Plasmas, **10**, 2994 (2003).

```
c = 3 * 10 ^ 8; (*speed of light m/s*)

kT = 1000; (*electron temp in keV*)

d = 1.5; (*Target thickness in microns*)

index = 1; (*micro bunching cycle, RA→1, jXB→2*)

θ = 15 * 2 Pi / 360; (*incidence angle, degree*)

Θ = 0 * 2 Pi / 360; (*electron observation angle, degree*)

Nt = 100 000; (*Total number of steps*)

Nb = 10; (*number of steps per cycle*)

M = 30 * index; (*# of micro pulses generated during laser pulse*)


lambda = 1057; (*laser wavelength in nm*)

dt = lambda * 10 ^ -9 / c / index; (*electron bunching cycle - sec*)


w0 = 2 Pi * c / (lambda * 10 ^ -9); (*laser frequency*)

deltat = dt / Nb; (*Time step sec*)

deltaf = 1 / (Nt * deltat); (*Frequency step size*)

TimeTable = Table[deltat * i, {i, 0, Nt - 1}]; (*timesteps of program*)
```

```
fsTimeTable = TimeTable * 10^15;(*time steps in sec?*)

FreqTable = Table[2 Pi * deltaf * i, {i, 0, Nt - 1}];(*freq steps of program*)

NFreqTable = FreqTable / w0;(*frequencies normalized to laser frequency*)

t0 = (d * 10^-6) / Cos[θ] / c;(*time required for electron to reach rear of target*)

step = Round[t0 / deltat] + 1;(*Number of time steps before t0*)

β[t_] := t0 / t;(*electron speed*)

g[t_] := (β[t]^4 Cos[θ] (Sin[θ] - β[t] Sin[θ]) Exp[(-511 / kT) ((1 - β[t]^2)^(-1/2) - 1)])
 / (((1 - β[t] Sin[θ] Sin[θ])^2 - β[t]^2 Cos[θ]^2 Cos[θ]^2) (1 - β[t]^2)^1.5)

SinglegTable = Join[Table[0, {step}], g[Take[TimeTable + 10^-24, -Nt + step]]];

gTable = Table[0, {Nt}];

For[i = 1, i ≤ M, i++, gTable += Join[Table[0, {Nb * (i - 1)}],
      Take[SinglegTable, Nt - Nb * (i - 1)]];];

ListPlot[Transpose[{TimeTable, gTable}], P
   lotRange → {{t0, (t0 + 2 M * dt)}, All}, Joined → True]

qatable = Exp[-NFreqTable^2 * Sin[θ]^2];

CTR = Abs[Fourier[gTable]]^2;

ListLogPlot[Transpose[{NFreqTable, CTR}],
 PlotRange → {{0, 10}, {0, 10^8}}, Joined → True]

CTR[[30001]]

0.265992

Num[t_] := 1/kT * β[t] Exp[(-511/kT) ((1 - β[t]^2)^(-.5) - 1)] / (t0 (1 - β[t]^2)^(1.5))
```

```
SingleNumTable = Join[Table[0, {step}],
    Num[Take[TimeTable + 10^-24, -Nt + step]]];


NumTable = Table[0, {Nt}];

For[i = 1, i ≤ M, i++, NumTable += Join[Table[0, {Nb * (i - 1)}],
      Take[SingleNumTable, Nt - Nb * (i - 1)]];];


ListPlot[Transpose[{fsTimeTable, NumTable / Max[NumTable]}],
 PlotRange → {{t0 * 10^15, (t0 + 1.5 M * dt) * 10^15}, All},
 Joined → True, AxesLabel → {"Time(fs)", "Number [a.u.]"},
 LabelStyle → Directive[Bold, Medium], PlotStyle → {Blue, Thick}]

ListPlot[Transpose[{NFreqTable, qatable}],
 PlotRange -> All, Joined → True]

Plot[Exp[-{z / (3 * 10^8) * Sin[θ]}^2 * (2 * 10^-6)^2],
 {z, 1.8 * 10^14, 1.8 * 10^15}, PlotRange → All]

elec = 1.6 * 10^-19;(*elec charge*)

ϵ0 = 8.85 * 10^-12;(*vacuum permittivity*)

Elecbunch = 1.18 * 10^10;(*electron bunch number*)

coherent = elec^2 * Elecbunch^2 / (8 * Pi^3 * c * ϵ0 * (511 / kT)^2 * t0^2) * Sin[θ]^2 * qatable * CTR;

ListLogPlot[Transpose[{NFreqTable, coherent / (3 * 10^17)}],
 PlotRange → {{0, 4}, {10^-12, 10^-6}}, Joined → True,
 AxesLabel → {"CTR Harmonic", "Energy(J)"}, LabelStyle → Directive[Bold, Medium]]
```

Appendix C Design of a Ti:Sapphire Power Amplifier

The Ti:Sapphire (Ti:Sa) power amplifier is the main addition to the THOR laser that will boost the output power from 20 TW to 1 PW. The desired goal is to extract greater than 45 J of energy while maintaining adequate beam quality to compress the beam to 30 fs on the target. The system components consist of the amplified medium, a 100 mm diameter Ti:Sa crystal, imaging telescopes for each beam pass, and an imaging telescope for transport to the compressor. The Ti:Sa crystal is 100mm diameter by 25 mm thick, an absorbance α of 1.21 cm^{-1}, and damage threshold of 14.6 J/cm^2 . The crystal is pumped by the custom glass pump amplifiers (described in a different section). The power amplifier consists of four (4) passes through the crystal. Each pass is relay imaged by off-axis parabolas(OAPs) resulting in a compact design housing the entire section in a 13 feet by 20 inch diameter(ISO 500) vacuum chamber. By using OAPs, the system is composed of all-reflective elements which reduce the system B-integral, wavefront distortions, ghost foci, while eliminating the need for radial group velocity and chromatic corrections. The position of the power amplifier in the laser chain is shown in figure 77 and a detail drawing of the power amplifier is shown in figure 78.

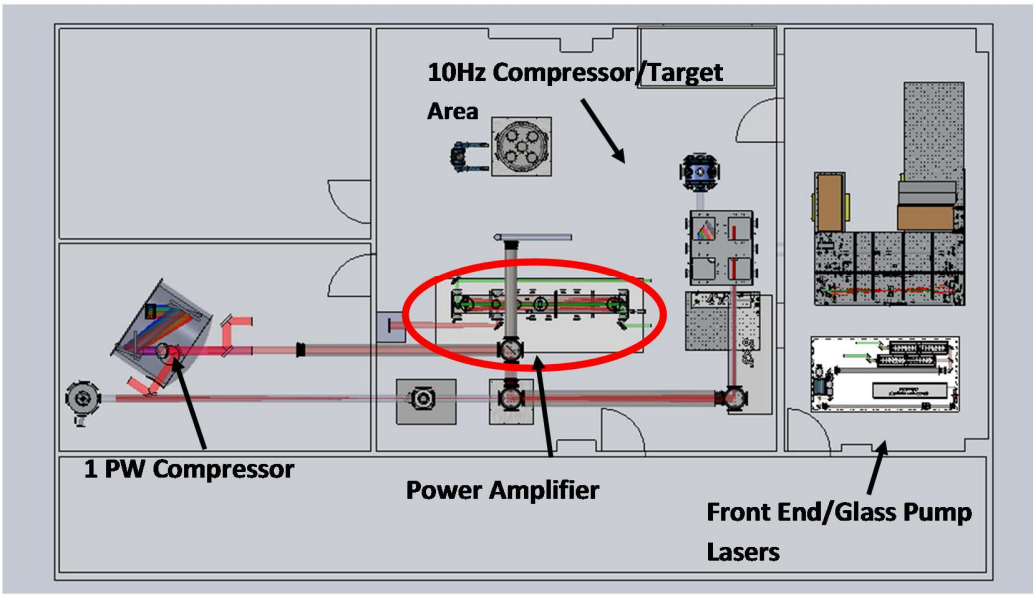

Figure 77: THOR PW upgrade layout showing the location of the power amplifier.

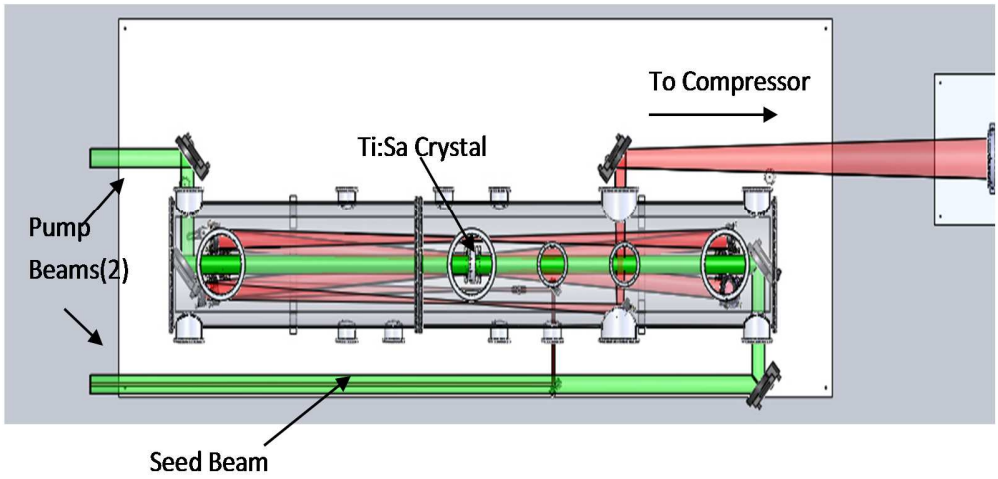

Figure 78: TOP view of the entire power amplifier assembly. The pump beams are shown in green. The seed beam is injected from the left side corresponding to the location of the existing 5-pass Ti:Sa laser amplifier.

The input beam to the power amplifier is the output beam from the 5-pass Ti:Sa amplifier described previously. The output from the 5-pass creates an image plane approximately two feet from the center of the crystal. From there, the beam enters the vacuum chamber and encounters a lens/OAP telescope combination which expands the beam from 13mm to 70mm and relays the image to the center of the Ti:Sa crystal. The pass by pass beam layout is documented at the end of the appendix. The OAP off-axis angle is 4.7° and focal length is 1524mm. This corresponds to translations of 101mm in x and 65mm in y with the crystal being at the center of the coordinate system. The beam then propagates collimated through the Ti:Sa crystal to the other side of the vacuum chamber. A 1-1 OAP telescope relay images the beam back to the center of the Ti:Sa crystal for the second pass. After the second pass, the beam is translated vertically by a rooftop mirror and passed back through the crystal for the third pass. Another pair of OAPs relay image the beam from the center of the crystal back on the crystal for the fourth pass through the crystal. After the fourth and final pass through the crystal, the beam is then upcollimated from 70mm to 170mm for delivery to the compressor. This is accomplished by a telescope combination of an OAP located in the vacuum chamber and an achromat lens outside the chamber. The OAP in the chamber has a larger off-axis angle of 6.3° to allow the beam to be picked off by a mirror and delivered out of the chamber. The achromat lens is on a separate table in the adjacent room where the compressor is located.

Based on energies derived from previous large aperture Ti:Sa based laser systems and preliminary calculations, it was determined that four passes would be sufficient to extract the necessary energy to achieve 1 PW. Four passes allows for reduced footprint design, reduced number of optical components and system optical aberrations. Since the goal is 1 PW on target, a 30 fs pulse on target and compressor throughput of ~60% is assumed. This means that we must extract >45 J of energy to ensure our on-target energy

goal is met. The energetics per pass is shown in figure 79. This was a result of 110J pump energy, 1 J input energy, 7 cm input beam, and 7.5 cm pump beam.

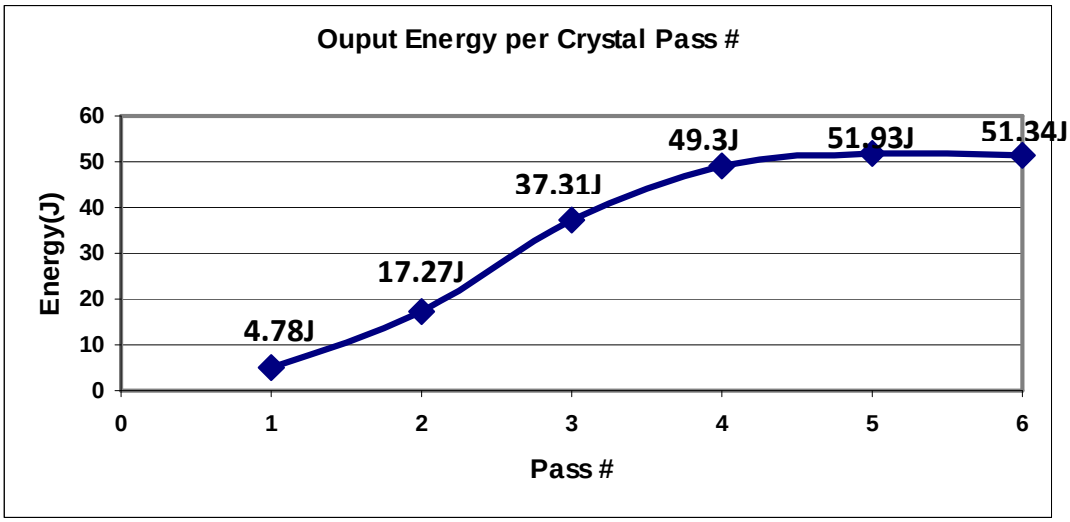

Figure 79: Output Energy per Ti:Sa crystal pass plotted as a function of pass #.

As can be seen from the graph, the beam saturates by the end of the 4th pass (Six passes are shown here to determine on which pass saturation begins). The beam saturation reduces the impact of input energy variation on the output energy. The pump energy is directly related to the output energy. The pump energy is also the source for Transverse gain which is very problematic in large aperture Ti:Sa laser systems. This must be accounted for and will be described in a later section. The beam size affects the amount of energy extraction as well. The same pump energy deposited in a small volume will excite more ions making them available for energy extraction by the seed pulse.

To verify these effects we analyzed their influence with two different codes. The given parameters were noted: percent of pump laser absorption, saturation fluence of medium, absorbance per length (α), and losses per pass. The remaining calculated parameters are

beam size, pump energy and input energy. These three parameters were varied and compared with two different codes. We used a 1-D user generated code, THOR PW Power Amp Laser Energetics, based on the Frantz-Nodvik laser rate equations. For comparison, we ran the same parameters in a 3-D laser design code, Miro, THOR PW Power Amp 3D Energetics Layout. The results are shown in the figure below. When not varied, a beam diameter of 7cm, with a pump beam of 7.5cm, pump energy of 110J and an input energy of 1J is assumed.

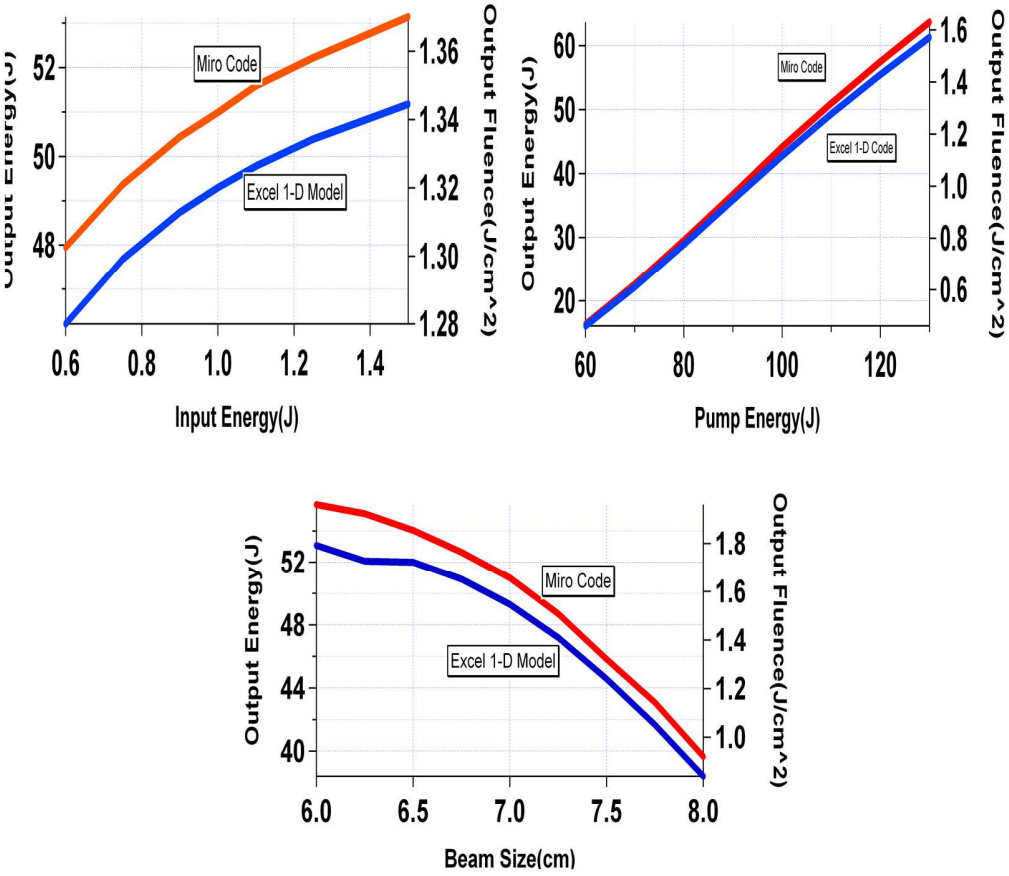

Figure 80: Plots showing output energy as a function of Input Energy, Pump Energy, and Beam Size. Miro code is shown in red with the Excel code shown in blue. The output fluence is shown on the right axis. The input beam is 7cm, pump beam is 7.5cm, input energy is 1J, and the pump energy is 110J.

THOR PW Power Amp Laser Energetics and Miro give consistent results. The differences can be attributed to the different manner of evaluating the pump beam interaction with the crystal. Additionally, the codes give slightly different results at the extremes of the parameter space. The magnitude of the difference is only about 1% of pump energy absorbance. The conclusion is that our 1-D model is approximate to Miro and can be used in calculations to produce an accurate result. When convenient, the 1-D model will be used to simulate the energetics due to ease of computation.

At smaller beam diameters, the 800nm beam fluence at the crystal face was a consideration. The coating damage quoted by Crystal Systems, Inc. was 14.6 J/cm2 for a 10ns pulse. This system's pulse duration of .6 ns corresponds to a damage fluence of 3.6 J/cm2. A safety factor of 2 was incorporated with respect to this damage threshold for the baseline design of the operating fluence. These considerations supported a beam diameter of 7 cm that will tolerate the maximum theoretical output of pump amplifiers and still enable attainment of the energy goal.

A large amount of energy will be extracted from the power amplifier section with the leading edge of the seed pulse experiencing a larger gain than the trailing edge. Since our pulse is dispersed in time (chirped), the leading edge (frequency) of the pulse encounters a greater population of ions in an excited state than the trailing edge (frequency). This can also be seen by the leading wavelengths (red ones) experiencing a larger gain that the trailing ones (blue). Some of these "dynamic" laser processes will be addressed in this section. From the code simulations, the input pulse profile from the existing THOR laser is identified as a 4th order spatially Gaussian pulse. Additionally, the pump laser profile can be modeled as a super-Gaussian pulse which has been assumed to be 5th order. Shown in figure 81 below are input and output fluences with line outs at the center of the beam

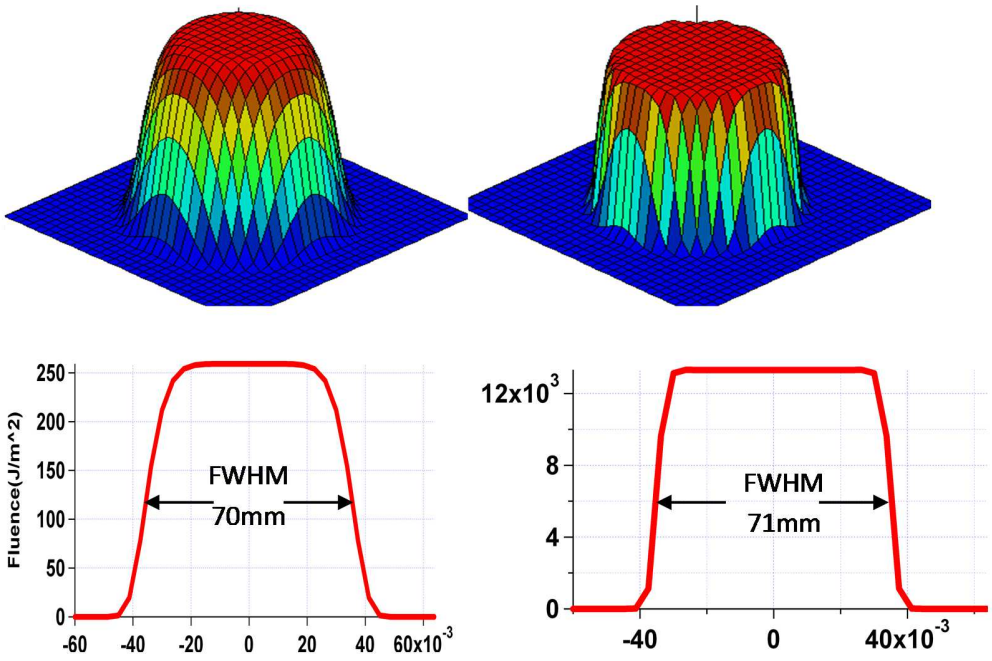

Figure 81: Input and output fluences with center line outs are shown left and right respectively. Parameters are 100 J pump energy, 1 J input energy, 7 cm seed beam, and 7.5 cm pump beam.

As shown above, the seed pulse profile experiences minor changes during the 4 passes through the power amplifier. The most visible effect is the slight increase in beam size. The main factors in the pulse shape as it progresses through the amplifier are the shape of the pump pulse and the saturation of the beam.

Another feature that changes during amplification is the beam spectrum. The beam spectrum is equivalent to a pulse stretched from 25fs to 600ps centered at 800nm. The input and output spectrums are shown in the figure below.

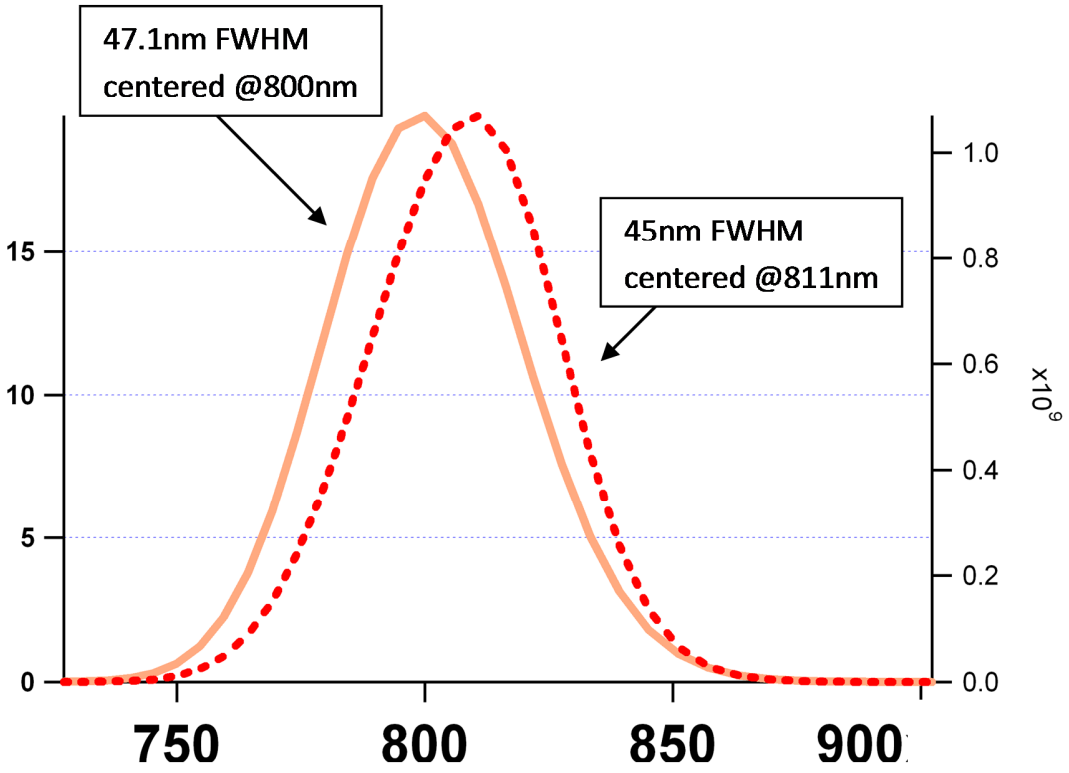

Figure 82: The input and output spectrum of a 20fs input pulse to the power amplifier is shown above. The input beam is centered at 800nm with a 47.1nm bandwidth. Output beam shows the center wavelength shift to 811nm with a narrower bandwidth of 45nm. The vertical axis units are of power – different scales for input and output.

The center wavelength experiences a shift to red wavelengths – 800 to 811- due to increased gain on the front part of the pulse. The pulse also experiences a small decrease in the FWHM of the spectrum. This is typical of multiple passes through a single amplifying medium and the decrease in spectrum will not affect the 30 fs pulse duration on target.

Another important "dynamic" process that occurs during the propagation of a laser pulse through an amplifying medium is the B-integral. The B-integral is defined as the peak non-linear phase shift of a pulse passing through a medium. Due to the all-reflective

imaging, the beam only passes through the input & output lenses and the Ti:Sa crystal. This keeps the cumulative B-integral low as shown in figure 83. The whole system B-integral is evaluated to yield a maximum value of .46 which is well below the maximum rule of thumb value of 1.

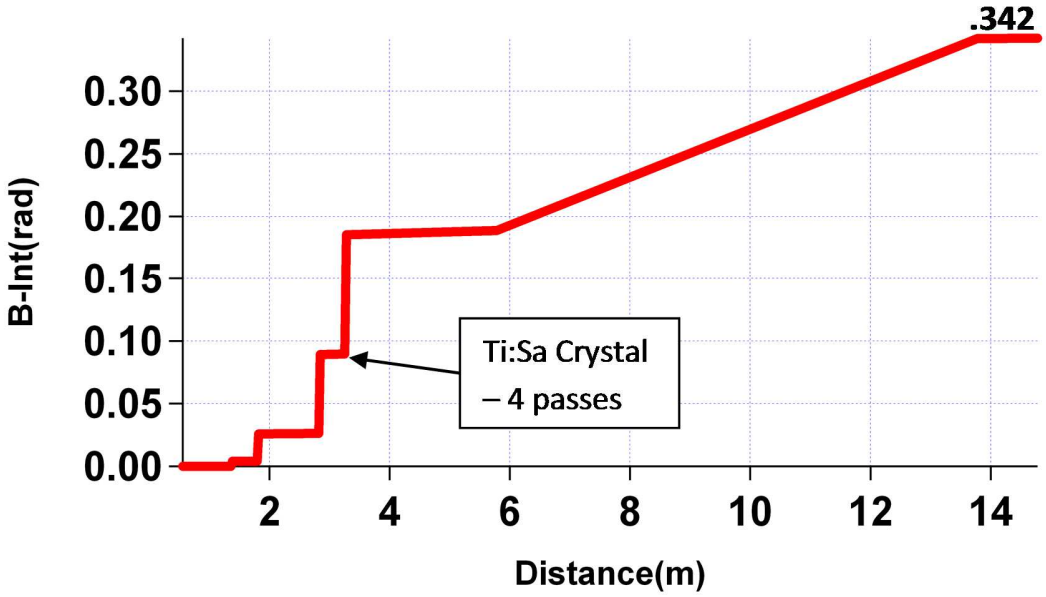

Figure 83: The B-integral of the power amplifier shown as a function of propagation distance through the system. The four passes through the crystal are shown on the left.

The system optical layout was modeled with Zemax© optical design software. The model, THOR PW Power Amp OAPs with achromat, consists of the input plano-convex lens, six (6) off-axis parabolic mirrors, a rooftop mirror and output lens to the compressor. The input beam is 13mm in diameter, no beam appodization, and a bandwidth of 70nm centered at 800nm. The only drawback to the model is the lack of Zemax© to prescribe any wavefront error to a reflecting surface. This will give a lower

than laboratory measured value for the wavefront distortion. The ray tracing of the system is shown in figure 84 below.

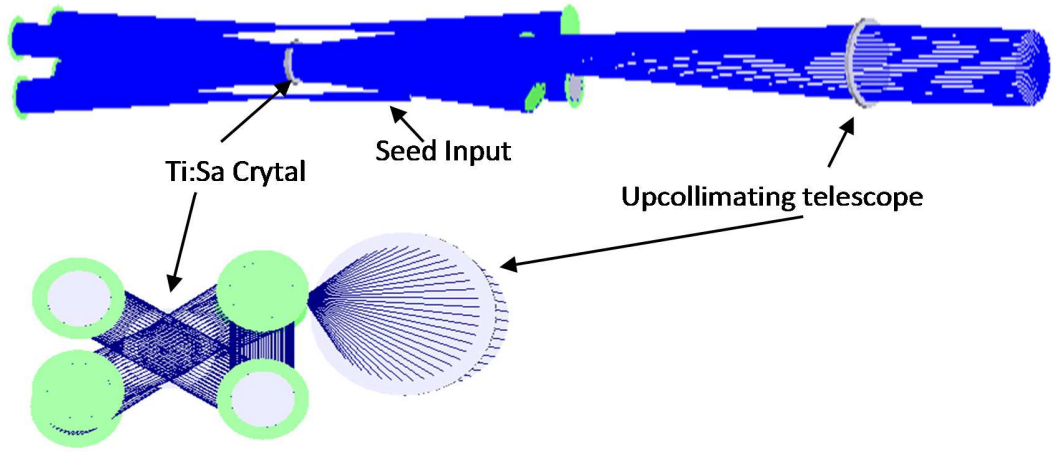

Figure 84: The system ray tracing is shown above. At top, is an ISO view of the system. Above is an end view with the expanding beam to the compressor on the right.

The input beam is up-collimated from 13mm to 70mm and relay imaged to the crystal by a plano-convex lens and an off-axis parabola pair depicted in the end of this section. The beam is relay-imaged by off-axis parabola pairs on passes 2 and 4. On Pass 3, the beam is displaced vertically by a rooftop mirror. After pass 4, the beam hits an off-axis parabola with a larger off-axis angle to enable a mirror to be inserted to send the beam out of the vacuum chamber to the compressor. The final off-axis parabola is paired with an achromat lens to up-collimate the beam to 170mm for delivery to the compressor.

The achromat lens is 8"ϕ and consists of BK7 and SF2 mixed glasses for chromatic dispersion. The main issue with the achromat lens was the location of the ghost foci. Specifically, a 2nd order forward propagating ghost focus due to the reflection of the interior surfaces (2nd & 3rd). The first surface of the achromat was assumed to be flat

which allowed Zemax© to optimize the radii of curvature of the other three surfaces for the needed focal length. However, this design yielded the 2nd order ghost focus propagating 20m in the forward direction. Depending on the exact location of the target chamber, the ghost focus would result in a relatively high intensity post pulse ~ 35ps after the main pulse and possibly create damage on the final focusing optic. By adjusting curvatures of the two interior surfaces, the location of this ghost focus could be adjusted from a few meters away up to 130m away. The final design was settled on a ghost focus 2.5m away which is placed in the center between two compressor mirrors. The optical characteristics for the complete system are shown in figure 85. The parabola and achromat lens telescope specifications are shown below in figure 86.

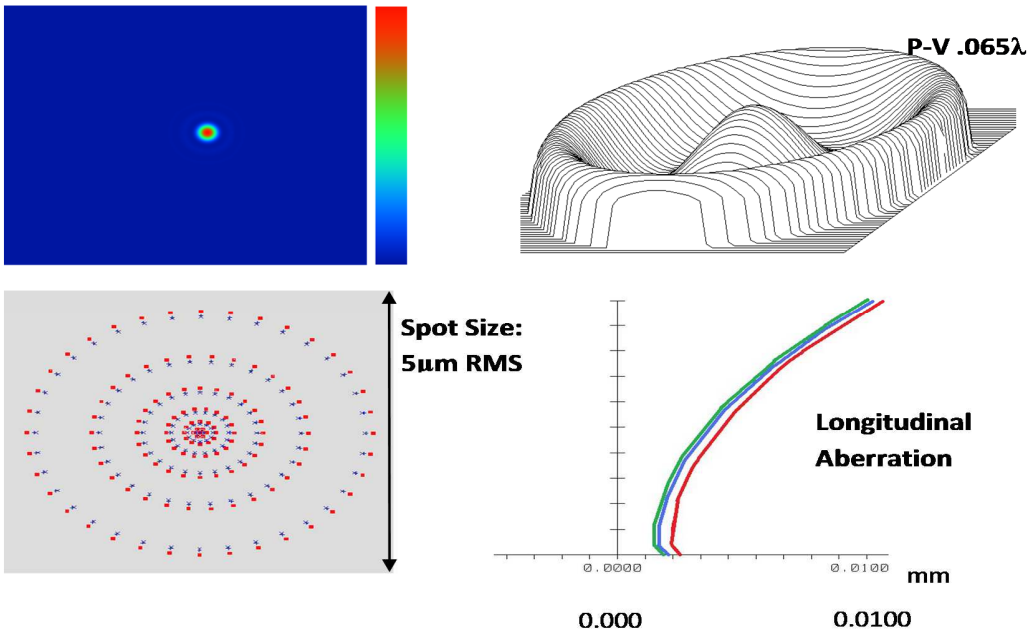

Figure 85: Optical characteristics of the power amplifier layout. Clockwise from the upper left is the far field of the beam. Top right is the wavefront distortion peak to valley. Bottom right is the longitudinal aberration and bottom left is the geometric ray tracing (neglecting diffraction) showing the spot size at focus.

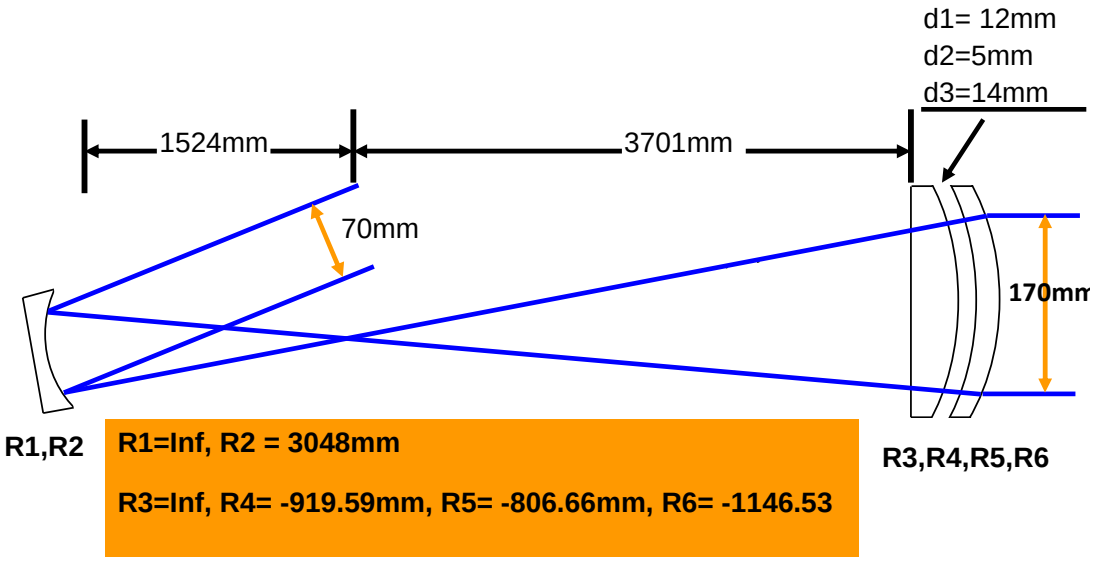

Figure 86: Layout of the upcollimating telescope before the compressor. Telescope consists of an off-axis parabola and an achromat lens.

A major issue in large aperture Ti:Sapphire laser systems is amplified spontaneous emission. Ti:Sa crystals are available in diameters of up to 10cm with thicknesses of 2-3cm so as to minimize the variation of ion dopant along the crystal axis. The crystals are typically pumped by green (~530nm) pump lasers due to the short fluorescence lifetime. In the typical arrangement, each crystal face is pumped by one or more pump beams. This allows a more uniform deposition of pump energy in the crystal and allows more pump energy input on the crystal due to reduced fluence as opposed to pumping on side of the crystal only. Typically, both seed and pump beam are vertically polarized aligning the pump energy with the largest crystal absorption cross section to achieve maximum energy extraction. The ASE and transverse gain is primarily affected by the pump beam and the crystal ion concentration along its crystal axis, α. This can be seen by the governing equation for the transverse gain: $G_T = \exp(\frac{F_o}{F_{Sat}} \frac{\nu_{las}}{\nu_p} \alpha D)$ where

F_o is the pump fluence on the face of the crystal, F_{sat} is the saturation fluence, α is the crystal absorbance, D is the pump beam diameter, ν_{las} & ν_P are the frequency of the seed and pump beam respectively.

The main problem is scattered photons that can reflect at the surface of the Ti:Sa crystal and then traverse the transverse length already excited by the pump beam diameter. If the gain along these transverse paths is high enough, amplification of these photons will actually deplete the remaining energy available for photons propagating in the longitudinal direction, reducing the energy output of the laser. The percentage of photons reflected is dictated by the large index mismatch between Ti:Sa (n=1.76) and air (n=1). To calculate the round-trip photon gain, the gain (transverse gain) and loss (Fresnel reflection of Ti:Sa/air) were multiplied and any value >1 was considered equivalent to lasing in the transverse direction. Only combinations of pump energy and beam size where the round trip gain was less than 0.5 were considered.

To reduce the index mismatch at the Ti:Sa/air interface, an index matching absorber is applied around the edge of the crystal. Several types are described in the literature and have been demonstrated in large aperture Ti:Sa systems. Since the crystal in this system is in vacuum, an index matching solution is used that is already in use on the Lawrence Livermore National Lab Titan Laser. The index matching solution consists of a thermoplastic polymer (Cargille Laboratories – MeltMount 5870 Cat #24170) mixed with an absorbing agent. At 800 nm, the index of refraction of the polymer is 1.69. This reduces the Fresnel reflection coefficient by a factor of ~200. The polymer is quite viscous at room temperature. However, the viscosity is inversely dependent to temperature. Heating the sample to around 60 -70°C allows the polymer to reach a "workable" state. This means the polymer is essentially a liquid. However, the polymer does not have a sharp melting point and will have to be visually inspected to determine

what state it presently is in. At this point, the polymer is poured into a mold around the crystal. The heat is then removed allowing the polymer to harden and stick to the edge of the crystal.

In order to prevent the scattered light from returning to the Ti:Sa crystal, the polymer is doped with an absorbing agent, in this case black ink toner. The toner is added when the polymer is heated and in a liquid state. In order to determine the amount of absorption from the ink toner, a typical ND filter was considered for comparison. A ThorLabs ND 2 filter (2" x 2" square) has a thickness of 0.06in and when considering the optical transmission using the Lambert-Beer Law, $T = \frac{I}{I_o} = 10^{-\alpha l}$, the ND filter has an absorption coefficient of 14.3 cm-1. Studies in the literature regarding the absorption coefficient of black ink have been published. A 10% aqueous solution of black ink corresponds to an absorption coefficient of ~15 cm-1. Since the path length of the light passing through the edge of the crystal and reflecting back is approximately .5 cm, this would corresponds to an absorbance equivalent to an ND 4 filter.

A crystal test fixture has been designed to create the mold housing the index matching solution. The text fixture, with the crystal inside, will be heated so as to eliminate any thermal discontinuities when applying the heated index matching absorber in liquid form. The index matching absorber can then be poured into the mold around the edge of the crystal. The fixture with crystal and index matching solution will be set aside and left to cool. Once the fixture cools, the crystal can be removed along with the polymer that has bonded to a Teflon ring separating the polymer from the test fixture. The crystal will then be transferred to a crystal holder that will house the crystal in the vacuum chamber. The test fixture and crystal housing are shown in figure 87.

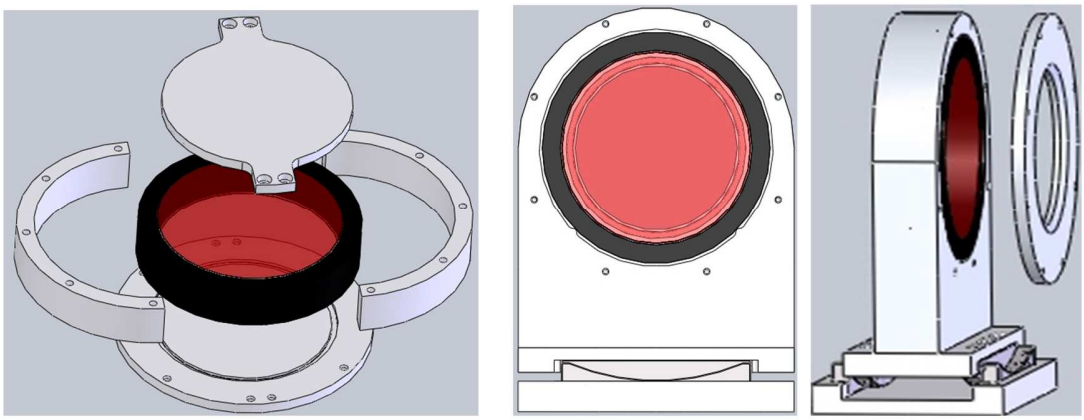

Figure 87: On left, expanded view of the test fixture to install the polymer on to the crystal. At right, a picture of the crystal holder with an exploded view of the mounting plate. The crystal holder has a manual goniometer at the base for minor adjustment of the crystal axis.

To achieve 1 PW on target, we have shown above that we need at least 110J of pump energy. At that energy, the transverse gain is ~28000 and the gain * Fresnel reflection is 11. This is a not acceptable operating condition primarily due to the high α of the crystal. To reduce the transverse gain while still allowing large pump energy, the polarization of pump beam is rotated 90° away from the crystal axis. This corresponds physically to a reduction of the absorption cross section in the crystal. In the transverse gain equation, this is represented by a change in α (=.5168) lowered in value comparable to the reduced absorption coefficient. This is in slight contrast to the traditional method of using a lower doped crystal with maximum absorption. In order to compensate for the reduced pump energy absorption, the pump beams are double passed through the compressor. The pump beam will pass through the crystal and be reflected by a 0° mirror tilted slightly to prevent the beam from propagating back upstream to the glass pump lasers. An additional benefit of the lowered absorption, α, is more uniform pump energy absorption

through the length of the crystal. The transverse gain using the double pass pump beam arrangement is shown for both α=1.21 and α=.5168 in figure 88.

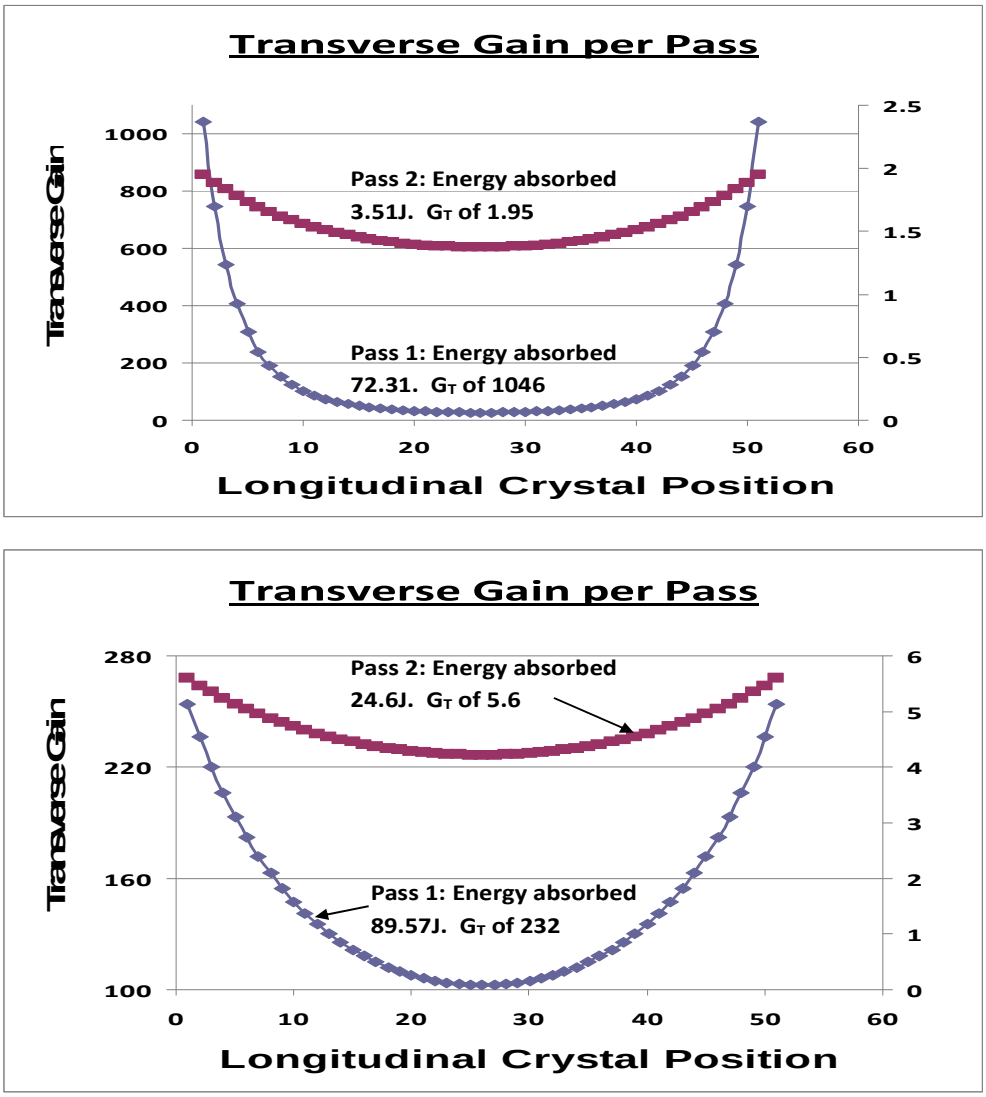

Figure 88: Plot of transverse gain versus longitudinal crystal position for two different crystal configurations. The blue curve is the first pass through the crystal and the blue is the second pass. The top configuration is a Ti:Sa crystal with an α of 1.21 and a pump energy of 80J. This results in a Transverse gain of ~2100 which is right at the lasing threshold. The bottom has an α of .5168, pump energy of 130J and a transverse gain of 1100.

Additional images showing the optical layout of the Ti:Sa power amplifier are provided.

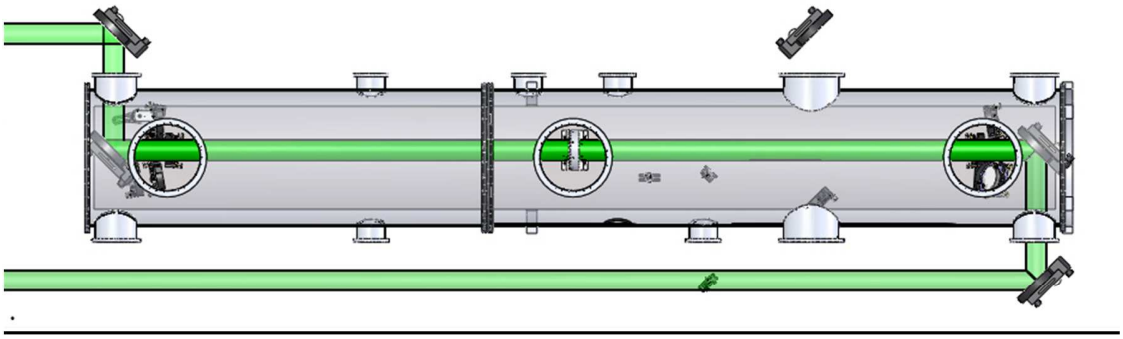

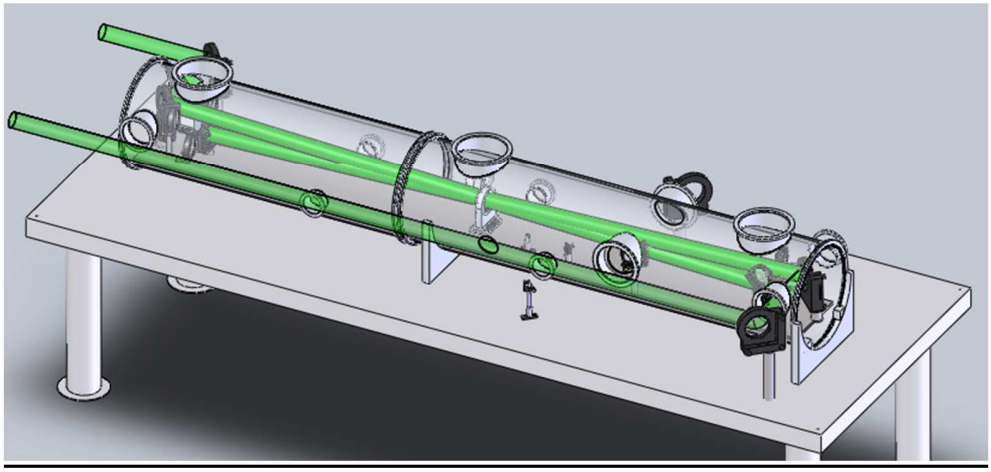

Figure 89: TOP and ISO view of pump beams entering the vacuum chamber. Pump beams excite the crystal 15-30ns before the seed beam arrives.

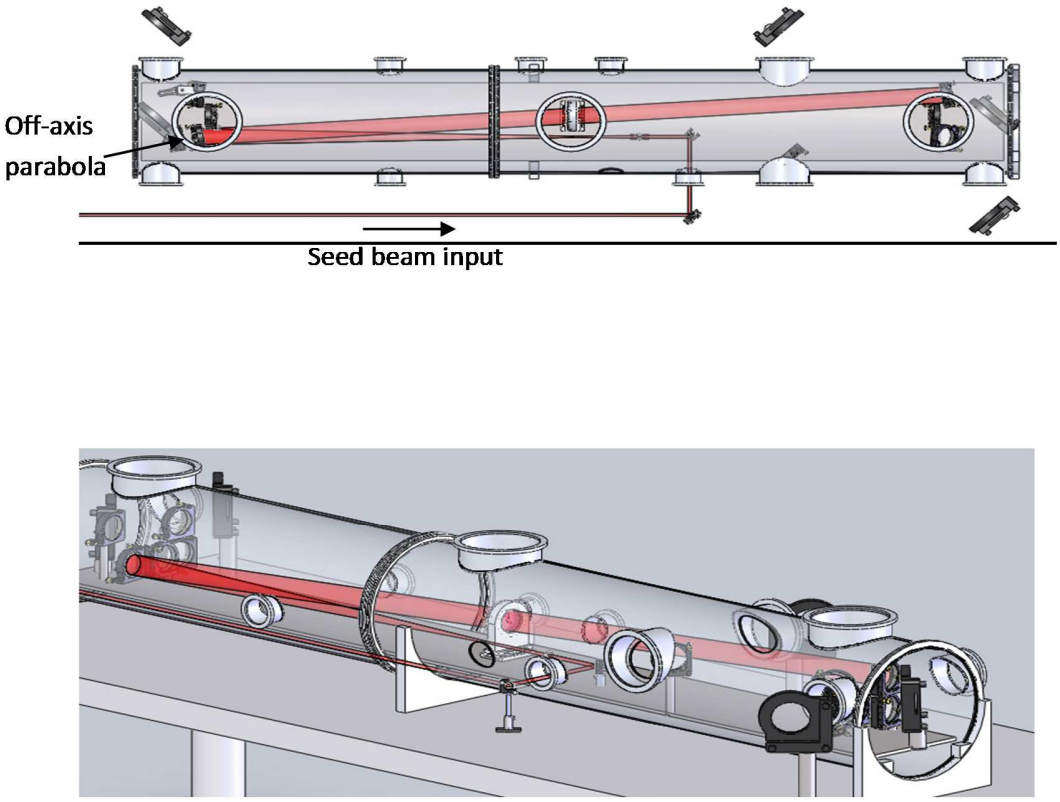

Figure 90: Entry seed beam shown in TOP and ISO views. Seed beam enter from the left which is the output of the existing 5-pass section. The beam is then up-collimated with a lens and achromat and the image is relayed to the center of the crystal. The collimated beam passes through the crystal to the opposite side of the chamber.

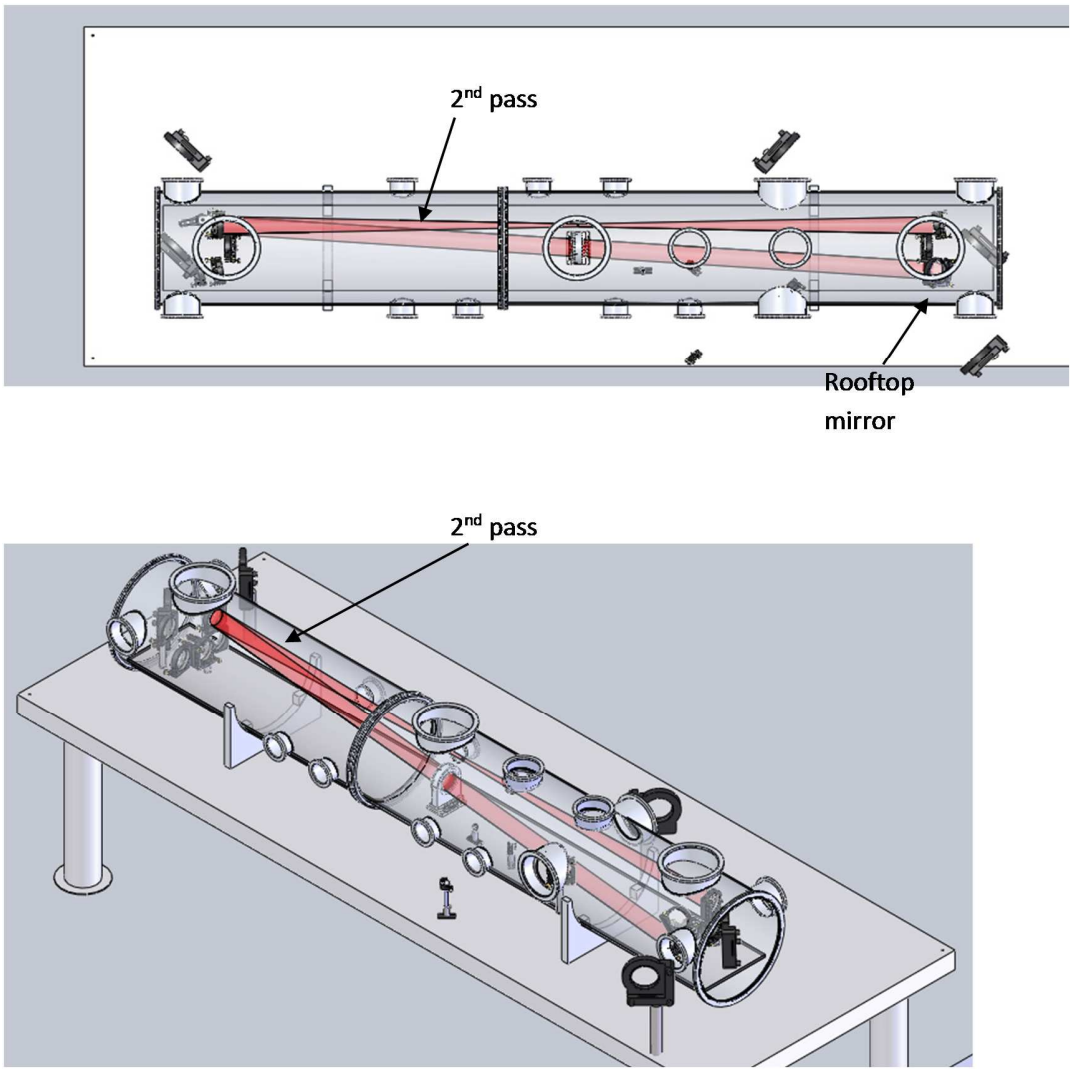

Figure 91: TOP and ISO layout of the 2nd beam pass through the crystal. The collimated beam from the first pass hits an achromat lens which forms a telescope with another achromat lens to relay image the beam from center crystal plan to crystal plane.

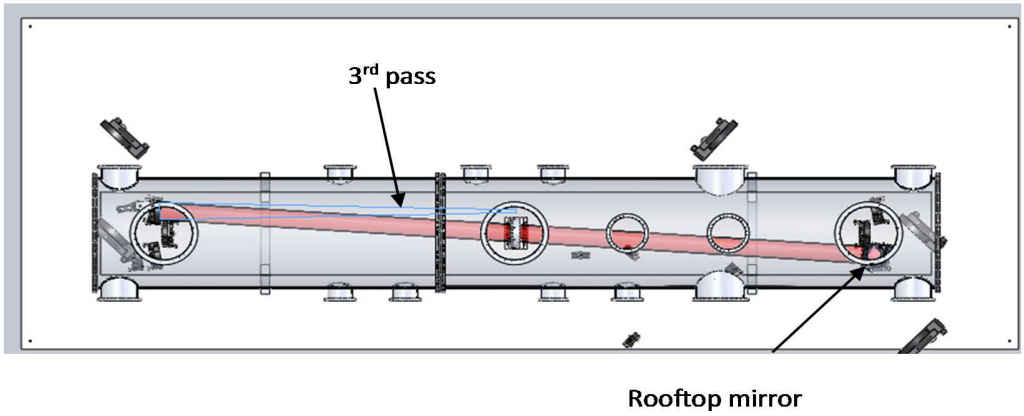

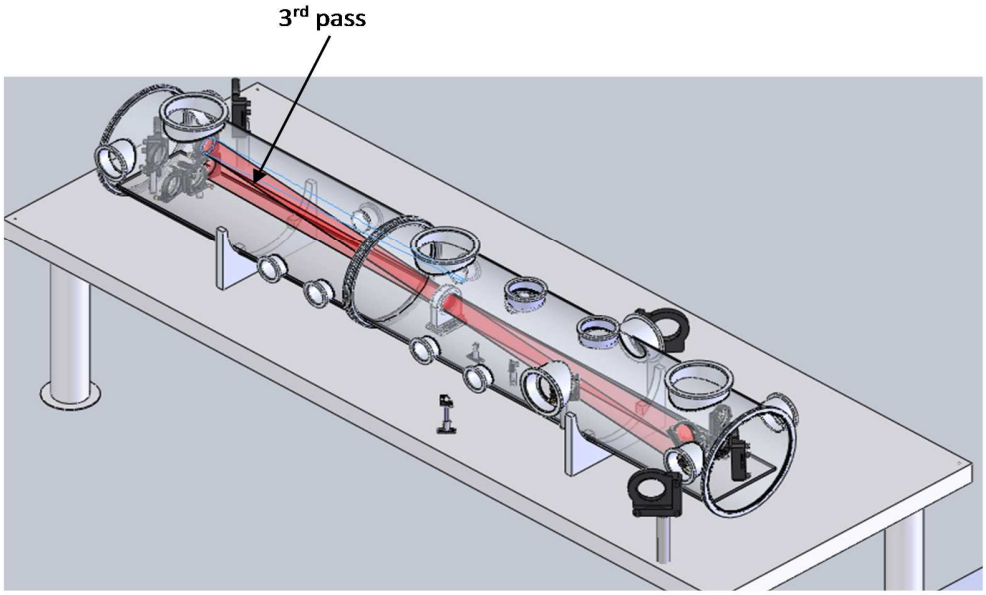

Figure 92: Shows the TOP and ISO views of the 3rd beam pass through the crystal. The beam after the 2nd pass through the crystal hits a rooftop mirror and is translated vertically back through the crystal. The entry and first beam pass is not shown for clarity.

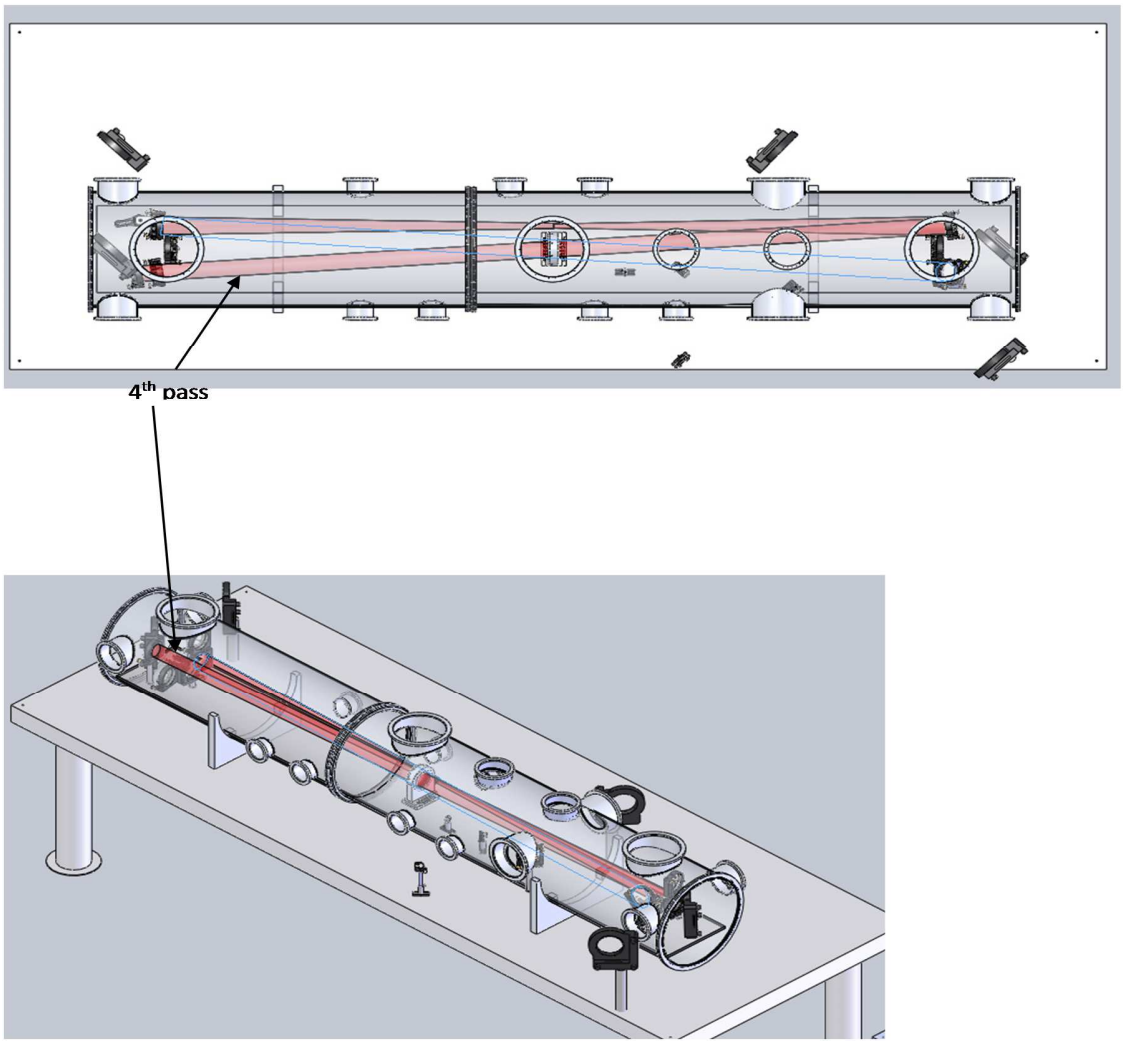

Figure 93: TOP and ISO view of 4th pass through the crystal. After the 3rd pass, another achromat telescope relay images the beam from crystal plane to crystal plane. The beam then exits vertically above the entry beam.

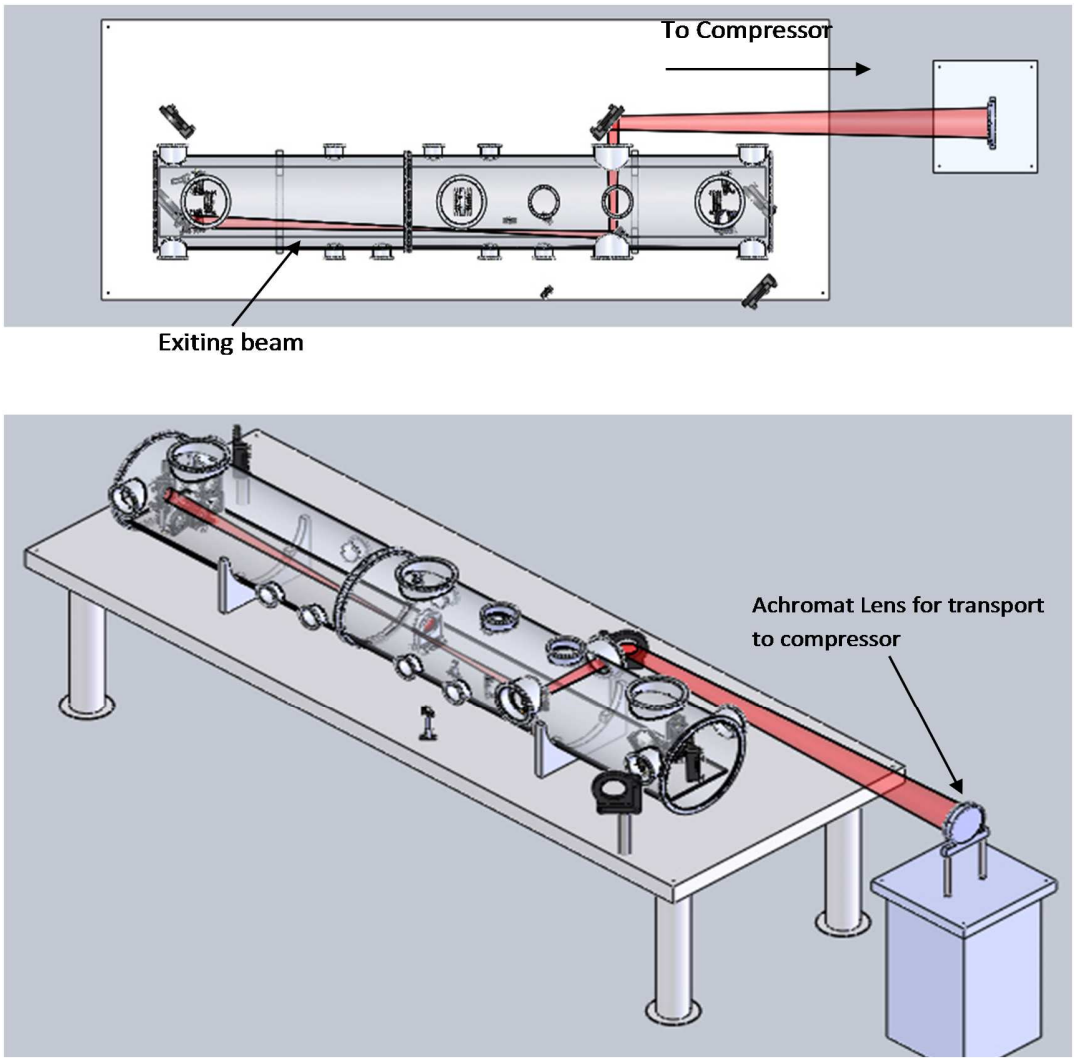

Figure 94: TOP and ISO images of the beam exiting the vacuum chamber. The last off-axis parabola has a larger off-axis distance to allow inserting a mirror to pick the beam off and send it to the compressor.

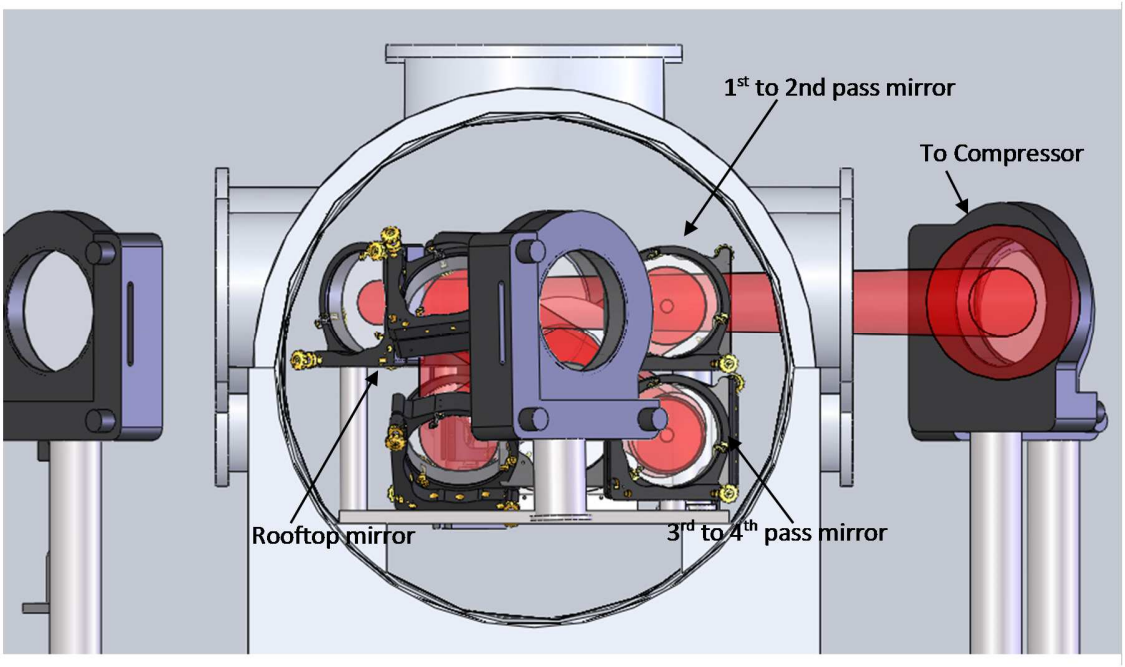

Figure 95: Image of vacuum chamber from end of chamber (right side end in all of the figures above).

Bibliography

1. D. Strickland and G. Mourou, *Compression of Amplified Chirped Pulses*, Optics Comm. **56**, 219(1985).
2. T. Tajima and G. Mourou, *Zetawatt-Exawatt Lasers and their applications in ultrastrong-field physics*, Physical Review Special Topics – Accelerators and Beams, **5**, 031031 (2002).
3. M. Krishnamurthy, S. Mondal, A. D. Lad, K. Bane, S. Ahmed, V. Narayanan, R. Rajeev, G. Chatterjee, P. K. Singh, G. R. Kumar, M. Kundu, and K. Ray, *A Bright Point Source of ultrashort hard x-ray pulses using biological cells*, Optics Express, Vol. 20. No. 5, 5754-5761.
4. A Ravasio et al., *Hard x-ray radiography for density measurement in shock compressed matter*, Physics of Plasmas **15**, 060701 (2008).
5. D. J. Hoarty, et al., *Equation of state studies of warm dense matter samples heated by laser produced proton beams*, High Energy Density Physics, Vol. 8, (2012), 50-54.
6. G. Dyer, R. Sheppard, J. Kuba, E. Fill. A. Wootton, P. Patel, D. Price, and T. Ditmire, *Isochoric heating of solid aluminum with picosecond x-ray pulses*, Journal of Modern Optics **50**, 2495-2505, (2003).
7. M. Roth et al., *Fast Ignition by Intense Laser-Accelerated Proton Beams*, Physical Review Letters **86**, 436 (2001).
8. M. Tabak, J. Hammer, M. E. Glinsky, W. L. Kruer, S. C. Wilks, J. Woodworth, E. M. Campbell, and M. D. Perry, *Ignition and high gain with ultrapowerful lasers*, Physics of Plasmas **1**, 1626 (1994).
9. M. H. Key, *Status and prospects for the fast ignition inertial fusion concept*, Physics Of Plasmas **14**, 055502(2007).
10. S. Atzeni and J. Meyer-ter-Vehn, *The Physics of Inertial Fusion*, Oxford University Press, 2004.
11. B. Vauzour et al., *Relativistic High-Current Electron-Beam Stopping-Power Characterization in Solids and Plasmas: Collisional versus Resistive Effects*, Phys. Rev. Lett. **109**, 255002 (2012).
12. L. Willingale et al., *Investigation of relativistic intensity laser generated hot electron dynamics via copper K_α imaging and proton acceleration*, Physics of Plasmas 20, 123112(2013).
13. R. B. Stephens et al., *K_α fluorescence measurement of relativistic electron transport in the context of fast ignition*, Phys. Rev. E **69**, 066414 (2004).

14. T. Johzaki et al., *Pre-plasma effects on core heating and enhancing heating efficiency by extended double cone for FIREX*, Nucl. Fusion, **51**, 073022 (2011).

15. J. J. Santos et al., *Fast Electron Transport in Ultraintense Laser Pulse Interaction with Solid Targets by Rear-Side Self-Radiation Diagnostics*, Phys. Rev. Lett. **89**, 025001 (2002)

16. A. Debayle, J. J. Honrubia, E. d'Humieres, and V.T. Tikhonchuk, *Divergence of laser-driven relativistic electron beams*, Phys. Rev. E **82**, 036405 (2010).

17. N. J. Sircombe, R. Bingham, M. Sherlock, T. Mendonca, and P. Norreys, *Plasma heating by intense electron beams in fast ignition*, Plasma Phys. Control. Fusion **50**, 065005.

18. A. Bret, and C. Deutsch, *Hierarchy of beam plasma instabilities up to high beam densities for fast ignition scenario*, Phys. Plasmas 12, 082704 (2005).

19. F. Pisani et al., *Experimental evidence of electric inhibition in fast electron penetration and of electric-field-limited fast electron transport in dense matter*, Phys. Rev. E **62**, R5927 (2000).

20. T. A. Hall et al., *Fast Electron Deposition in Laser Shock Compressed Plastic Targets*, Phys. Rev. Lett. **81**, 1003 (1998).

21. A. P. L. Robinson and M. Sherlock, *Magnetic collimation of fast electrons produced by ultraintense laser irradiation by structuring the target composition*, Phys. Plasmas **14**, 083105 (2007).

22. P. Drake, *High-Energy-Density Physics*, Springer Series: Shock Waves and High Pressure Phenomena (2010).

23. F. Chen, *Introduction to Plasma Physics*, Plenum (1974).

24. W. L. Kruer, *The Physics of Laser Plasma Interaction*, Addison-Wesley Publishing Company, 1988.

25. S. C. Wilks and W. L. Kruer, *Absorption of Ultrashort, Ultra-Intense Laser Light by Solids and Overdense Plasmas*, IEEE Journal of Quant. Elec., Vol. 33, 11, 1997.

26. S. Palaniyappan et al., *Dynamics of Relativistic Transparency and optical shuttering in expanding overdense plasmas*, Nat. Phys. **8**, 763 (2012).

27. B. J. Albright, L. Yin, K. J. Bowers. B. M. Hegelich, K. A. Flippo, T. J. T. Kwan, and J. C. Fernandez, *Relativistic Buneman instability in the laser breakout afterburner*, Phys. Plasmas **14**, 094502 (2007).

28. L. D. Landau and E. M. Lifshitz, *The Classical Theory of Fields*, Butterworth-Heinemann (1975).

29. E. Esarey, P. Sprangle, and J. Krall, *Laser acceleration of electrons in a vacuum*, Phys. Rev. E **52**, 5443 (1995).

30. P. Gibbon, *Short Pulse Laser Interactions with Matter: An Introduction*, Imperial College Press (2005).

31. D. Bauer, P. Mulser and W. Steeb, *Relativistic Ponderomotive force, Uphill acceleration, and Transition to chaos*, Phys. Rev. Lett. **75**, 4622 (1995).

32. D. D. Meyerhofer et al., *Resonance Absorption in high-intensity contrast, picosecond laser-plasma interactions*, Phys. Fluids B 5, 2584 (1993).

33. P. Gibbon and E. Forster, *Short-Pulse Laser-Plasma Interactions*, Plasma Phys. Control. Fusion **38**, 769 (1996).

34. H. M. Milchberg, R. R. Freeman, and S. C. Davey, *Resistivity of a Simple Metal from Room Temperature to 10^6 K*, Phys. Rev. Lett. **61**, 2364 (1988)

35. R. Fedosejevs et al., *Absorption of Femtosecond Laser Pulses in High-Density Plasma*, Phys. Rev. Lett. **64**, 1250 (1990).

36. Y. B. Zeldovich and Y. P. Raizer, *Physics of Shock Waves and High-Temperature Hydrodynamic Phenomena*, Dover Publication Inc. (2002).

37. M. D. Rosen, *Scaling Law for femtosecond laser plasma interactions*, Femtosecond to Nanosecond High-Intensity Lasers and Applications 1229, 160 (1990).

38. W. Rozmus and V. T. Tikhonchuk, *Skin effect and interaction of short laser pulses with dense plasmas*, Phys. Rev. A **42**, 7401 (1990).

39. F. Brunel, *Not-So-Resonant, Resonant Absorption*, Phys. Rev. Lett. **59**, 52 (1987).

40. M. K. Grimes, Y. S. Lee, A. R. Rundquist, and M. C. Downer, *Experimental identification of 'vacuum heating' at femtosecond-laser-irradiated metal surfaces*, Phys. Rev. Lett. **82**, 4010 (1999).

41. P. Gibbon and A. R. Bell, *Collisionless absorption in sharp-edge plasmas*, Phys. Rev. Lett. **68**, 1535 (1992).

42. P. McKenna et al., *Laser Plasma Interactions and Applications*, Springer International Publishing (2013).

43. W. L. Kruer and K. Estabrook, *J x B heating by very intense light*, Phys. Fluids, **28**, 430 (1985).

44. S. Wilks and W. L. Kruer, *Advances in Plasma Physics*, Woodbury, NY AIP (1994).

45. G. Malka and J. L. Miquel, *Experimental Confirmation of Ponderomotive-Force Electrons Produced by Ultrarelativistic Laser Pulse on a Solid Target*, Phys. Rev. Lett. **77**, 75 (1996).

46. A. A. Andreev, *Generation and Application of Ultra-High Laser Fields*, NOVA Science Publishers, Inc. (2001).

47. P. J. Catto and R. M. More, *Sheath inverse bremsstrahlung in laser produced plasmas,* Phys. Fluids **20**, 704 (1977).

48. S. C. Wilks, W. L. Kruer, M. Tabak, and A. B. Langdon, *Absorption of ultra-intense pulses,* Phys. Rev. Lett. **69**, 1383 (1992).

49. J. J. Santos et al., *Fast-Electron transport and induced heating in aluminum foils,* Phys. Plasmas **14**, 103107 (2007).

50. J. Zheng et al., *Study of Hot Electrons by Measurement of Optical Emission from the Rear Surface of a Metallic Foil Irradiated with Ultraintense Laser Pulse*, Phys. Rev. Lett. **92**, 165001 (2004).

51. F. N. Beg et al., *"Study of picosecond laser-solid interactions up to 10^{19} W/cm^2*, Phys. Plasmas **4**, 447 (1997).

52. V. T. Tikhonchuk, *Interaction of a beam of fast electrons with solids*, Phys. Plasmas **9**, 1416 (2002).

53. H. Alfven, *On the Motion of Cosmic Rays in Interstellar Space*, Phys. Rev. **55**, 425 (1939).

54. S. Humphries, *Charged Particle Beams*, Wiley-Interscience (1990).

55. D. A. MacLellan et al., *Annular Fast Electron Transport in Silicon Arising from Low-Temperature Resistivity,* Phys. Rev. Lett. **111**, 095001 (2013).

56. R. R. Freeman, D. Batani, S. Baton, M. Key, and R. Stephens, *The Generation and Transport of Large Currents in Dense Materials: The Physics of Electron Transport Relative to Fast Ignition,* Fusion Sci. Technol. **49**, 297 (2006).

57. R. F. Benjamin, G. H. McCall, and A. W. Ehler, *Measurement of a Return Current in a Laser Produced Plasma,* Phys. Rev. Lett. **42**, 890 (1979).

58. A. R. Bell, J. R. Davies, S. Guerin, and H. Ruhl, *Fast-electron transport in high-intensity short-pulse laser-solid experiments*, Plasma Phys. Control. Fusion **39**, 653 (1997).

59. R. M. More, *Pressure Ionization, Resonances, and the Continuity of Bound and Free States*, Adv. At. Mol. Phys. **21**, 305 (1985).

60. D. Schroeder *An Intro to Thermal Physics*, Addison Wesley Longman (2000).

61. K. Eidmann, J. Meyer-ter-Vehn, T. Schlegel and S. Huller, *Hydrodynamic simulation of subpicosecond laser interaction with solid-density matter*, Phys. Rev. E **62**, 1202 (2000).

62. N. W. Ashcroft & N. D. Merriman, *Solid State Physics,* Harcourt Brace Publishers (1976).

63. Y. T. Lee and R. M. More, *An Electron Conductivity Model for Dense Plasmas*, Phys. Fluids **27**, 1273 (1984).

64. M. P. Desjarlais, J. D. Kress, and L. A. Collins, *Electron Conductivity for warm, dense aluminum plasmas and liquids,* Phys. Rev. E **66**, 025401 (2002).

65. T. Tanka, *Optical Absorption and Electrical Conduction in polyethylene,* J. Appl. Phys. **44**, 2430 (1973).

66. L. Spitzer Jr., *Physics of Fully Ionized Gases,* Interscience Publishers (1956).

67. H. Brysk, P. M. Campbell, and P. Hammerling, *Thermal Conduction in Laser Fusion,* Plasma Physics **17**, 473 (1974).

68. E. S. Weibel, *Spontaneously Growing Transverse Waves in a Plasma Due to an Anisotropic Velocity Distribution,* Phys. Rev. Lett. **2**, 83 (1959).

69. L. O. Silva et al., *On the role of the purely transverse Weibel instability in fast ignition scenarios,* Phys. Plasmas **9**, 2458 (2002).

70. P. A. Norreys et al., *Intense laser-plasma interactions: New Frontiers in high energy density physics,* Phys. Plasma **16**, 041002 (2009).

71. M. S. Wei et al., *Observations of the filamentation of high-intensity laser-produced electron beams,* Phys. Rev. E **70**, 056412 (2004).

72. R. Jung et al., *Study of Electron-Beam Propagation through Preionized Dense Foam Plasma,* Phys. Rev. Lett. **94**, 195001 (2005).

73. J. R. Davies, A. R. Bell, M. G. Haines, and S. M. Guerin, *Short-pulse high-intensity laser-generated fast electron transport into thick solid targets,* Phys. Rev. E **56**, 7193 (1997).

74. A. P. L, Robinson, M. H. Key, and M. Tabak, *Focusing of Relativistic Electrons in Dense Plasma Using a Resistivity-Gradient-Generated Magnetic Switchyard,* Phys. Rev. Lett. **108**, 125004 (2012).

75. B. Ramakrishna et al., *Laser-Driven Fast Electron Collimation in Targets with Resistivity Boundary,* Phys. Rev. Lett. **105**, 135001 (2010).

76. F. Perez, A. J. Kemp, L. Divol, C. D. Chen, and P. K. Patel, *Deflection of MeV Electrons by Self-Generated Magnetic Fields in Intense Laser-Solid Interactions,* Phys. Rev. Lett **111**, 245001 (2013).

77. J. R. Davies, J. S. Green, and P. A. Norreys, *Electron Beam Hollowing in laser-solid interactions,* Plasma Phys. Control. Fusion **48**, 1181 (2006).

78. L. Gremillet, G. Bonnaud, and F. Amiranoff, *Filamented transport of laser-generated relativistic electrons penetrating a solid target,* Phys. Plasmas **9**, 941 (2002).

79. D. Batani et al., *Transport of intense laser-produced electron beams in matter,* Plasma Phys. Control. Fusion **48**, B211 (2006).

80. S. I. Krasheninnikov, A. V. Kim, B. K. Frolov, and R. Stephens, *Intense electron beam propagation through insulators; Ionization front structure and stability*, Phys. Plasma **12**, 073105 (2005).

81. H. Bethe and J. Ashkin, *Experimental Nuclear Physics*, J. Wiley (1953).

82. A. R. Bell, J. R. Davies, S. Guerin and H. Ruhl, *Fast-electron transport in high intensity short-pulse laser-solid experiments*, Plasma Phys. Control. Fusion **39**, 653 (1997).

83. J. D. Jackson, *Classical Electrodynamics*, Wiley & Sons (1999).

84. V. L. Ginzburg and I. M. Frank, *Radiation of a uniformly moving electron due to its transition from one medium into another*, Zh .Eksp. Teor. Fiz **16**, 15 (1946).

85. J. Van Tilborg, C. B. Schroeder, E. Esarey, and W. P. Leemans, *Pulse shaped and spectrum of coherent diffraction-limited transition radiation from electron beams*, Lasers and Particle Beams **22**, 415 (2004).

86. E. Fermi, Z. Phys., **29**, 315 (1924).

87. M. L. Ter-Mikaelian, *High-Energy Electromagnetic Processes in Condensed Media*, Wiley & Sons, Inc. (1972).

88. J. Zheng et al., *Spectrum of transition radiation from hot electrons generated in ultra-intense laser plasma interaction*, Phys. Plasmas **9**, 3610 (2002).

89. J. Zheng, K. A. Tanaka, T. Miyakoshi, Y. Kitagawa, R. Kodama, T. Kurahashi, and T. Yamanaka, *Theoretical study of transition radiation from hot electrons generated in the laser-solid interaction*, Phys. Plasmas **10**, 2994 (2003).

90. G. Hays, *Development of Broad Spectrum Technologies for High Energy Chirped Pulse Amplification*, Ph.D. Thesis – The University of Texas at Austin (2007).

91. S. Feldman, *Isochoric heating of copper to Warm Dense Matter state using protons produced through solid-laser interactions*, Ph.D. Thesis – The University of Texas at Austin (2013).

92. R. W. Boyd, *Nonlinear Optics*, Academic Press (2008).

93. O. E. Martinez, *3000 Times Grating Compressor with Positive Group Velocity Dispersion: Application to Fiber Compensation in 1.3 to 1.6 μm Region*, IEEE J. Quantum Electron. **QE-23**, 59 (1987).

94. Siegman, *Lasers*, University Science Books (1986).

95. E. Hecht, *Optics*, Addison-Wesley Publishing Company (1990).

96. B. I. Cho, J. Osterholz, A. C. Bernstein, G. M. Dyer, A. Karmakar, A. Pukhov, and T. Ditmire, *Characterization of two distinct, simultaneous hot electron beams in intense laser-solid interactions*, Phys. Rev. E **80**, 055402(R) (2009).

97. J. J. Gilvarry, *The Lindemann and Gruneisen Laws*, Phys. Rev. **102**, 308 (1956).

98. W. Grigsby, *Experimental Studies of High Energy Density Silicon Using Ultra-fast Lasers*, Ph.D. Thesis – The University of Texas at Austin (2007).

99. J. A. Koch et al., *Experimental measurement of deep directional columnar heating by laser-generated relativistic electrons at near solid density*, Phys. Rev. E **65**, 016410 (2001).

100. M. Tatarakis et al., *Plasma Formation on the Front and Rear of Plastic Targets due to High-Intensity Laser-Generated Fast Electrons*, Phys. Rev. Lett. **81**, 999 (1998).

101. M. Borghesi et al., *Observations of Collimated Ionization Channels in Aluminum-Coated Glass Targets Irradiated by Ultraintense Laser Pulses*, Phys. Rev. Lett. **83**, 4309 (1999).

102. M. Storm et al., *High-Current, Relativistic Electron-Beam Transport in Metals and the Role of Magnetic Collimation*, Phys. Rev. Lett. **102**, 235102 (2009).

103. U. Teubner et al., *Harmonic Emission from the Rear Side of Thin Overdense Foils Irradiated with Intense Ultrashort Laser Pulses*, Phys. Rev. Lett. **92**, 185001 (2004).

104. C. S. Brady and T. D. Arber, *An ion acceleration mechanism in laser illuminated targets with internal electron density structure*, Plasma Phys. Control. Fusion **53**, 015001 (2011).

Vita

Joel Kevin Blakeney was born in Baton Rouge, La to Ernest and LaWanda Blakeney. He earned a B.S. in Physics in May 1996 from Centenary College. He earned a M.S. in Mechanical Engineering from the University of Texas at Austin in December 2000. After graduation, he worked as a mechanical engineer at Applied Materials. After Applied Materials, he became a laser engineer on the construction of the Texas Petawatt. He then entered UT in August 2008 to begin his doctoral studies in Physics.

Permanent Address: joelblakeney@yahoo.com

This dissertation was typed by Joel Blakeney.